

The Implications and Characteristics of Diffuse-like but Dynamic Aurora

Riley N Troyer¹, Casey T Deroo¹, Jasper S Halekas¹, David M Miles¹, Robert G Michell²,
and Allison N Jaynes¹

¹The University of Iowa Department of Physics and Astronomy

²NASA Goddard

May 25, 2023

THE IMPLICATIONS AND CHARACTERISTICS OF DIFFUSE-LIKE BUT DYNAMIC
AURORA

by

Riley Troyer

A thesis submitted in partial fulfillment
of the requirements for the Doctor of Philosophy
degree in Physics in the
Graduate College of
The University of Iowa

May 2023

Thesis Committee: Allison N. Jaynes, Thesis Supervisor

Casey T. DeRoo

Jasper S. Halekas

David M. Miles

Robert G. Michell

Copyright by

Riley Troyer

2023

All Rights Reserved

I dedicate this thesis to:
Samantha Pedek,
for her steadfast support and continual encouragement to pursue my interests.

ACKNOWLEDGEMENTS

My past five years at the University of Iowa have been filled with incredible highs, but also challenging lows. Throughout it I have questioned a lot and stressed about my decisions, but I never regretted my choice to pursue a PhD. I attribute much of this to the unwavering support and mentorship from my advisor, Dr. Allison Jaynes. There were certainly challenges being the first graduate student in the group, working through COVID-19, and a several year rocket launch delay, but Allison's ability to always be available to talk or answer a question is something that I will forever be inspired by. I would also like to thank the other members of my thesis committee (Dr. Casey DeRoo, Dr. Jasper Halekas, Dr. David Miles, and Dr. Robert Michell) for their insightful suggestions and advise regarding my work.

Throughout my degree there have been many others who I am indebted to. I'd specifically like to thank Dr. Steve Kaeppler, a previous Hawekeye alumni and invaluable mentor on everything from radar science to career advise. In a similar vein, I'd like to thank Roger Varney for his help with all things radar related.

Rachael Filwett was another invaluable resource and excellent office mate for my first couple years. The other members of our research group (Sanjay Chepuri, Keith Vidal, Jaya Joseph, Garry Gao, Jodie McLennan, among others) and department (Daniel Simmons and Connor Feltman, among others) were also incredible kind and supportive throughout my time at Iowa and I hope that we will continue to reconnect at the various stages of our future careers.

My path to a PhD didn't start in Iowa. I began my research journey in undergrad and thus need to thank Dr. Mark Conde, my undergraduate research mentor, for the advise and opportunities he provided, and for introducing me to space physics. Dr. David Newman, my undergraduate and SPS advisor, is another. While less influential to my research, he supported and advised me in all of my other academic related interests including science policy and SPS. These have since carried on into my graduate career. In that vein, I'd like to thank the executive committee members (Ellen Kiser, Kurayi Mahachi, Murphy Keller, Cody Poe, Emma Herbach, Qierra Brockman, and

Anya Morozov) of Connecting Science to Society, the science policy student organization we founded. One of my most influential experiences to date was the SPS summer internship during my undergrad. For that opportunity I owe a huge thanks to Dr. John Mather for his generous funding of the internship, to the SPS national team, including Dr. Brad Conrad, for managing the experience, and to my fellow 2017 interns.

I'd like to extend a thank you to the wonderful people of Venetie, Alaska who helped out during the LAMP rocket mission. In addition to the village as a whole, my thanks go to Lance Whitwell Jr. for his gracious hospitality, and to the people, whose names I do not know, that offered their plane seats to me when I had to fly back home on short notice due to a family medical emergency.

I'd also like to say thank you to my incredible parents, Corrine Leistikow and Eric Troyer. They gave me the opportunity to pursue this research with their support and encouragement. Looking back on an "autobiography" I wrote somewhere around 4th grade, it appears that they cultivated my passion for science from an early age because I wrote that I'd like to grow up to be a scientist.

Finally, I need to give the biggest thank you to my future wife, Samantha Pedek. Her support has meant the world to me. She moved across the country to live together in a 375 sq ft studio as I pursued my PhD. We have since upgraded to a larger apartment and she is graduating with a masters of science education, but her steadfast support has never changed. I honestly do not know what I would have done without her.

I could continue for many pages, but my thesis has already extended beyond the length I was expecting so I must cut these acknowledgements short. For anyone I left out, I apologize and know that your contributions did not go unnoticed. I have been incredible grateful for all of the wonderful people across the university, nation, and world that I have gotten the opportunity to work with and learn from.

ABSTRACT

The aurora (northern/southern lights) are a majestic display of light that illuminates the night sky at high latitudes in the northern and southern hemispheres. These lights come in several different varieties. Discrete and substorm aurora are the brightest and most photogenic type, but in this thesis we focus on the dimmer, but just as important, diffuse aurora. More specifically, we look at subsets of diffuse aurora that are also dynamic. A majority of this work is devoted to pulsating aurora, which appear as an uncoordinated symphony of dim auroral patches that blink on and off across wide portions of the sky. Pulsating aurora plays an important role in energy transfer between the magnetosphere and the upper atmosphere. This energy transfer can have significant impacts on the atmosphere, such as ozone depletion. Using electron density measurements from the Poker Flat Incoherent Scatter Radar, we were able to statistically quantify the energy flux of electrons responsible for pulsating aurora. We found a significant contribution from > 30 keV electrons, which increases in close temporal proximity to a substorm and for periods of high AE index. We also found that following a substorm, the energy flux from > 30 keV electrons decays with an e-folding time of 0.95 hr. Using wave measurements from the Van Allen Probes, we were able to connect this timescale to a similar e-folding time of 1.18 hr for lower-band chorus waves following a substorm. Combined, these results support the hypothesis that pulsating aurora represents a significant loss of energetic electrons from the outer radiation belt to the atmosphere. It also supports the hypothesis that pulsating aurora are the result of Doppler-shifted cyclotron resonance between energetic substorm electrons and lower-band chorus waves. However, much regarding diffuse and dynamic aurora is still unknown. This is evident in the diffuse auroral eraser, a new phenomenon that we characterize as a rapid brightening and then dimming of a diffuse arc superimposed on a background diffuse aurora. Upon dimming, the background aurora get erased and takes approximately 20 seconds to return to normal. We believe this feature may shed light on how different magnetospheric waves could influence each other. However, we need more observations to solve this puzzle and hope our results will inspire future studies into diffuse and

dynamic aurora.

PUBLIC ABSTRACT

The aurora (northern/southern lights) are a majestic display of light that illuminates the night sky at high latitudes in the northern and southern hemispheres. These lights come in several different varieties. Discrete and substorm aurora are the brightest and most photogenic type, but in this thesis we focus on the dimmer, but just as important, diffuse aurora. More specifically, we look at subsets of diffuse aurora that are also dynamic. A majority of this work is devoted to pulsating aurora, which appear as an uncoordinated symphony of dim auroral patches that blink on and off across wide portions of the sky. Pulsating aurora are caused when energetic electrons get perturbed into the atmosphere from a region of Earth's magnetic field called the Van Allen radiation belts. These aurora are important to study because they can impact a variety of processes important to society, such as destroying ozone. In this thesis, we studied the energy of pulsating aurora electrons. We quantified the most energetic events and found that they occur close in time to a shock in Earth's magnetic field, called a substorm. We also found that the total energy reduced, after a substorm, over a specific time frame. We were then able to connect that time frame to a similar one that we measured, using satellites, for electromagnetic waves in the Van Allen radiation belts. This supports the hypothesis that pulsating aurora originate in the Van Allen radiation belts and that the electrons which cause them are perturbed into the atmosphere by waves in Earth's magnetic field. However, much regarding diffuse and dynamic aurora is still unknown. This is evident in the diffuse auroral eraser, a new phenomenon that we characterize in this thesis. We believe this feature may shed light on how different types of waves in Earth's magnetic field could influence each other. However, we need more observations to solve this puzzle and hope our results will inspire future studies into diffuse and dynamic aurora.

TABLE OF CONTENTS

LIST OF TABLES	xii
LIST OF FIGURES	xiii
CHAPTER 1: BACKGROUND MATERIAL	1
Discrete Aurora	1
The Auroral Substorm	2
Pulsating Aurora	3
Imaging the Aurora	4
Auroral Interactions with the Atmosphere	5
Rocket Studies of the Aurora	7
Incoherent Scatter Radar	7
Pulsating Aurora and the Atmosphere	8
Earth's Magnetic Field	10
Magnetic Local Time	12
Ground-based Magnetometers	12
The Magnetic Field in Context and Source of Discrete Aurora	13
Atmospheric Current Systems	14
The Outer Van Allen Radiation Belt and Source of Pulsating Aurora	15
Drifts	16
Bounce Motion	19
Plasma Waves	22
Pitch Angle Scattering	26
Lower-band Chorus as a Driver of Pulsating Aurora	28
CHAPTER 2: THE ENERGY CONTENT OF PULSATING AURORA	30

Introduction	30
Data	32
Analysis	34
Magnetic Local Time	36
Substorm Onset and AE index	37
Energy Spectra from Electron Density Inversion	40
Discussion	42
Summary	45
The LAMP Rocket Mission	46
 CHAPTER 3: THE SOURCE MECHANISM OF PULSATING AURORA	 49
Background	49
Data	52
Electric and Magnetic Fields	52
Post-Substorm Identification	52
Chorus Selection	53
Analysis	54
Variations with Magnetic Local Time	54
Variations with Magnetic Latitude	56
Comparison with Meredith et al. (2000)	56
Comparison with Pulsating Aurora	58
Simulation	61
Errors	62
Discussion	63
Magnetic and Electric Field Differences	64
Summary	65
Additional Tables and Figures	65

CHAPTER 4: THE DIFFUSE AURORAL ERASER	69
Introduction	69
Data	71
Case Study	72
Analysis	73
Discussion	77
Summary	80
CHAPTER 5: ANALYSIS AND VISUALIZATION METHODS	82
Energy Inversion	82
Poker Flat Incoherent Scatter Radar Data	86
Machine Learning Identification	89
Data Processing	89
Training Data	90
Model	91
CHAPTER 6: CONCLUSIONS	94
Pulsating Aurora Energy	94
Pulsating Aurora Source Mechanism	95
Diffuse Auroral Eraser	96
REFERENCES	97
APPENDIX A: THE USE OF COLOR IN SCIENTIFIC PLOTS	116
Naturally Perceived Order	116
Artificial Boundaries and Gradients	117
Obscuring Features	117
APPENDIX B: DERIVATIONS	123

Dipole Field	123
Plasma Parameter	126
Gradient Curvature Drift	127
Bounce Motion	131
Plasma Waves	134
Pitch Angle Diffusion	140

LIST OF TABLES

Table 1. Full chorus, LBC, and UBC magnetic (B) and electric (E) SD decay timescales (τ) and peak wave magnetic field (B_w) for the midnight (21 to 3 MLT) region. We included error, R^2 values, and the number of statistics for the magnetic field measurements (N_B) to contextualize the quality of each fit.	66
Table 2. Full chorus, LBC, and UBC magnetic (B) and electric (E) SD decay timescales (τ) and peak wave magnetic field (B_w) for the predawn (3 to 6 MLT) region. We included error, R^2 values, and the number of statistics for the magnetic field measurements (N_B) to contextualize the quality of each fit.	66
Table 3. Full chorus, LBC, and UBC magnetic (B) and electric (E) SD decay timescales (τ) and peak wave magnetic field (B_w) for the dawn (6 to 9 MLT) region. We included error, R^2 values, and the number of statistics for the magnetic field measurements (N_B) to contextualize the quality of each fit.	66
Table 4. Full chorus, LBC, and UBC magnetic (B) and electric (E) SD decay timescales (τ) and peak wave magnetic field (B_w) for the morning (9 to 12 MLT) region. We included error, R^2 values, and the number of statistics for the magnetic field measurements (N_B) to contextualize the quality of each fit.	66
Table 5. Full chorus, LBC, and UBC magnetic (B) and electric (E) SD decay timescales (τ) and peak wave magnetic field (B_w) for the afternoon (12 to 15 MLT) region. We included error, R^2 values, and the number of statistics for the magnetic field measurements (N_B) to contextualize the quality of each fit.	68
Table 6. Full chorus, LBC, and UBC magnetic (B) and electric (E) SD decay timescales (τ) and peak wave magnetic field (B_w) for the evening (15 to 18 MLT) region. We included error, R^2 values, and the number of statistics for the magnetic field measurements (N_B) to contextualize the quality of each fit.	68

LIST OF FIGURES

Figure 1.	Image of discrete aurora above the LAMP rocket mission’s Venetie imager enclosure.	2
Figure 2.	A series of grayscale 428 nm images from the Poker Flat Research Range All Sky Imager with several pulsating aurora patches of differing sizes. The main patch is highlighted by the red oval. The red dot indicates the center of the field of view.	4
Figure 3.	Image from the bottom of the LAMP mission Venetie camera observatory. The skylights are dome shaped to allow the camera lenses to view the entire sky. In the image, cameras are installed in three domes, and three are empty.	6
Figure 4.	Image of the LAMP rocket mission launching into an instance of pulsating aurora. Credit: Justin Hartney	8
Figure 5.	Image of the Poker Flat Incoherent Scatter Radar (PFISR), located 30 miles north of Fairbanks, Alaska.	9
Figure 6.	An example dipole field created by a current loop.	11
Figure 7.	Artistic depiction of Earth’s magnetosphere. The red lines represent Earth’s magnetic field. The orange and yellow lines represent the incoming solar wind. The blue region is the plasma sheet. The green region represents the Van Allen radiation belts. Note, the planet is not to scale. Image credit: William Crochot, NASA.	15
Figure 8.	Altitude of the mirror point for particles with various pitch angles as measured at the magnetic equator on field line $L = 5.5$. This corresponds to a latitude of 64.8° , which is in the auroral oval.	20
Figure 9.	Gradient curvature drift and bounce periods over common pulsating aurora L-shells and energies. We’ve calculated the gradient curvature drifts for a 90° pitch angle. We’ve calculated the bounce period for a 5° pitch angle, which is close to the loss cone.	22
Figure 10.	Image from Kivelson and Russell (1995) depicting the three most important electron motions for pulsating aurora in Earth’s magnetic field. Electrons gyrate around field lines, bounce between mirror points near each pole, and drift eastward around the planet. For a 30 keV electron, located at $L = 5$, with a pitch angle $\alpha = 45^\circ$ at the equator, the respective timescales of these motions are 1.4×10^{-4} s, 1.1 s, and 1×10^4 s.	23

Figure 11. Panels A1-A3 show a series of 428 nm images from the Poker Flat Research Range All Sky Imager with several pulsating aurora patches of differing sizes. Even though the imaging cadence of 12 seconds is longer than some pulsating periods, we can still identify pulsating aurora. The red dot indicates the center of each image and thus the approximate location of the vertical PFISR beam. Panel B is the PFISR electron number density data for a pulsating aurora event on October 13, 2016. The data is plotted vs. altitude in km and universal time. The dashed red line indicates the start of pulsating aurora. The dashed and dotted blue line indicates when the images were taken. The radar stopped taking data before the pulsating aurora ended. The solid blue line indicates the lowest altitude where $N_e = 10^{10} \text{ m}^{-3}$	33
Figure 12. Lowest altitude PFISR measurements during pulsating aurora with $N_e = 10^{10} \text{ m}^{-3}$ plotted versus magnetic local time [A], time from the nearest substorm onset [B], AE index [C], and combined substorm and AE [D]. The black diamonds indicate the average altitude for the surrounding hour, 20 minutes, 200 nT of AE, and 20 minutes respectively. The red lines indicate the 25% and 75% quartiles.	36
Figure 13. Altitude of the peak electron density in PFISR measurements during pulsating aurora plotted versus magnetic local time [A], time from the nearest substorm onset [B], AE index [C], and combined substorm and AE [D]. The black diamonds indicate the average altitude for the surrounding hour, 20 minutes, 200 nT of AE, and 20 minutes respectively. The red lines indicate the 25% and 75% quartiles.	37
Figure 14. Lowest altitude PFISR measurements during pulsating aurora with $N_e = 10^{10} \text{ m}^{-3}$ plotted versus AL indices. The black diamonds indicate the average altitude for the surrounding hour, 20 minutes, 200 AE units respectively. The red lines indicate the 25% and 75% quartiles.	39
Figure 15. The high ($\geq 30 \text{ keV}$) and low ($< 30 \text{ keV}$) differential energy flux contributions to pulsating aurora events occurring in four temporal bins relative to substorm onset [A] and AE index [B].	42
Figure 16. Loss Through Auroral Microburst Pulsations (LAMP) rocket mission logo. As the logo designer, I had to shamelessly include this in my thesis. There are several hidden gems in the logo. The blue background and big dipper star constellation are the colors and constellation of the Alaska State flag. This represents the rocket launching from Alaska. The modulating light and dark auroral arcs represent pulsating aurora. The microburst wiggles that break up the inner boarder are pulled directly from the original microburst paper (Anderson & Milton, 1964). There are three of these trains to represent the 3 Hz flicker of pulsating aurora. Finally, the lamp (besides the obvious) represents the mission phrase "shinning a light on pulsating aurora".	48

- Figure 17. The inverse of magnetic field wave power decay timescales for the entire chorus range (solid), LBC (dashed), and UBC (dotted) versus MLT. For many of the points, the associated errors are smaller than the marker size. We combined the region 21 to 24 and 0 to 3 MLT and omitted 18 to 21 MLT due to statistical limitations. 55
- Figure 18. Statistical behavior, during the quiet period following substorms, of magnetic chorus wave power. The left (right) column of figures shows the behavior in the 21 to 9 MLT (9 to 18 MLT) region. The top (bottom) row of figures shows the behavior for 0° to 10° (10° to 20°) MLAT. The blue scatter points are the underlying data, the black scatter points are the geometric mean value of the proceeding 10 minutes of data. The dashed line is the best exponential decay to the first 75 minutes of data. Note that the wave power is natural log transformed. 57
- Figure 19. Figure using the data from Chapter 2 showing the decay of ≥ 30 keV pulsating aurora electrons after substorms. The blue scatter points indicate the underlying data, the black scatter points are the geometric mean values of the surrounding 20 minutes of energy flux, and the red line is the best fit exponential decay. The r^2 value is based on the fit to the black scatter points. Note that the energy flux is natural log transformed. 59
- Figure 20. Statistical behavior of magnetic wave power, during the quiet period following substorms, from the LBC [a] and UBC [b] frequency ranges. Data in the figure is from the region 21 to 5 MLT, $3 < L < 6.6$, and -20° to 20° MLAT. The blue scatter points indicate the underlying data, the black scatter points are the geometric mean value of the proceeding 10 minutes of data. The dashed black line is the best exponential decay to the first 75 minutes of data. Note that the wave power is natural log transformed. 60
- Figure 21. Results from our quasi-linear diffusion simulation of chorus waves. Panel A shows how the initial electron energy distribution decays over the simulation. The solid black lines indicate 14 keV and 125 keV and are the approximate bounds of strong diffusion. The dashed red line indicates 30 keV, which we define as the boundary between high and low energy electrons. Panel B shows the summed decay of low ($14 \text{ keV} \leq E < 30 \text{ keV}$) and high ($30 \text{ keV} \leq E \leq 125 \text{ keV}$) electrons within the region of strong diffusion. The solid lines indicate the normalized flux decays, while the dashed gray lines are the best fit exponentials for the first 30 minutes of the simulation. 62
- Figure 22. The inverse of magnetic (dashed) and electric (solid) field wave power decay rates for the entire chorus range (Panel A), LBC (Panel B), and UBC (Panel C) versus MLT. For many of the points, the associated errors are smaller than the marker size. We combined the region 21 to 24 and 0 to 3 MLT and omitted 18 to 21 MLT due to statistical limitations. 67

Figure 23. An unprocessed image from the original data. The first several seconds of the video include a UT timestamp. Ursa Major appears at the top of the image. . . .	72
Figure 24. Images across a characteristic eraser event. From left to right the images are before the event, during the event brightening, and during the event eraser. The red dots indicate the 5 pixels we used to represent the event.	73
Figure 25. The averaged intensity of a characteristic eraser event. The event is color coded by phase: initial (solid green), brightening (dotted red), eraser (solid black), recovery (dotted purple).	74
Figure 26. A keogram containing all of the auroral eraser events we identified. We increased the contrast and used the Viridis color map to see the events better.	75
Figure 27. Epoch analysis for the 22 eraser events with a full recovery. The red lines indicate the start and stop of the average recovery period, which is 20 seconds. Some of the time series show periodic behavior.	76
Figure 28. Histogram of the recovery times for the 22 eraser events with a full recovery. The recovery time is calculated as the time between the end of the eraser phase to when the brightness returns to the average of 43 seconds to 10 seconds before the brightening phase.	76
Figure 29. Five ground-based magnetometers during the night of March 15, 2002. The plots are arranged by eastward geographic longitude from bottom to top. The bottom three are located between Churchill and the west coast of Greenland. The top two are located on the east coast of Greenland and on Svalbard.	78
Figure 30. Event 6 begins as a normal eraser event, but before the diffuse background is able to fully refill, a second event (7) appears to occur. After this the background refills as normal.	81
Figure 31. The high (≥ 30 keV) and low (< 30 keV) differential energy flux contributions to pulsating aurora events occurring in four temporal bins relative to substorm onset [A] and AE index [B]. We set the bar heights to the GPI+ model. The scatter points indicate the individual values from the three other chemistry models.	85
Figure 32. An example fitted electron density using the maximum entropy method along with the GPI+ chemistry model. The plot on the left shows the PFISR measured electron density (black) along with the associated error (red). The initial guess is shown in green and the final fit is shown in orange. The plot on the right is the differential number flux over the range of energies given to the model.	86
Figure 33. Hiss noise in the vertical PFISR beam measured as a function of beam range. . .	88

Figure 34. An image from one of the test of our machine learning model. The image here was classified with a scaling technique that doesn't perform as well in poor conditions as our CLAHE technique. In this image the moon is up and the optics are damaged in some way. The combined result is a very over saturated image and the model is unable to see the aurora, thus classifying it as a bad viewing condition. The image was taken with the Gillam, MB ASI on 2015-10-02	92
Figure 35. An image from one of the test of our machine learning model. The image here was classified with our CLAHE technique. In this image the moon is up and the optics are damaged in some way. However, our processing technique is able to enhance the auroral features and allows us to see pulsating aurora. The machine learning model is also able to detect them based on the classification confidence. The image was taken with the Gillam, MB ASI on 2015-10-02	93
Figure A.1.A demonstration why the rainbow colormaps does not have a naturally perceived order. Which grayscale sequence is in order? Now which color sequence is in order?	118
Figure A.2.Four different data sets from Borland and Taylor Ii (2007) plotted with four different colormaps. Notice the artificial gradients in the first and third columns for the rainbow colormap.	119
Figure A.3.A figure from Borland and Taylor Ii (2007) demonstrating how the rainbow colormap can obscure data, particularly near the color green.	120
Figure A.4.A plot of global elevation based on sea level for both the rainbow colormap and Seismic, diverging colormap. Small variations around sea level are difficult to view in the rainbow colormap.	121

PREFACE

Live for a period in a northern culture and you'll quickly realize that the aurora are an ever present aspect of winter life. Some refer to them as the northern lights, others as the aurora borealis, but in spite of different names, most who have spent time in the north can relate to the experience of witnessing these beautiful nighttime lights. I grew up in Fairbanks, Alaska and have had many opportunities to live out this experience. In fact, as a slightly dark thought, I've often wondered how many vehicle accidents are caused by fantastic auroral displays. I remember several instances where I was driving home and the aurora came out in full force. I'd be craning my neck trying to watch the red, green and blue dance through a frosty windshield, paying less attention to the road than I should have. Despite these experiences, until my undergrad, I did not realize that the aurora could have real and measurable impacts on society, besides perhaps a car crash here or there. Nor did I realize that scientists studied the aurora. Auroral science is contained within the field of space physics, which aims to understand the region between the Sun and Earth. There are three key pillars to space physics: the Sun and solar wind, Earth's magnetic field, also called the magnetosphere, and Earth's upper atmosphere. All three of these systems are linked and couple together in complex ways. However, because the field is so large, space physicists must specialize. My specialty, a specific type of aurora, toes the line between magnetosphere and atmosphere. This special aurora is dim and diffuse, but also dynamic. It's difficult to see by eye, but incredibly influential to the system. Much of my work has been to understand how this aurora forms and what impacts it has on our atmosphere, specifically through statistical studies. This type of aurora varies significantly between different events and because of that, to make general statements, we need to go beyond case studies and look to larger statistical data sets. In Chapter 2 I study the statistical energy content of pulsating aurora, a type of diffuse-like and dynamic aurora. In Chapter 3 I uncover and investigate a timescale that can give us more statistical context to the magnetospheric source of this aurora. Finally, in Chapter 4 I look at a new auroral phenomenon that could shed light on how different types of aurora interact. Before jumping into my research,

in Chapter 1, we will cover the relevant space physics background concerning the magnetosphere, Earth's upper atmosphere, and the aurora.

CHAPTER 1: BACKGROUND MATERIAL

1.1 Discrete Aurora

When I think of the aurora, my mind jumps to bright curtains and arcs of green light, stretching from west to east, and dancing across the sky. Most photographs, artistic visions, and descriptions depict something similar. The light is bright, defined, and often dynamic. In the scientific field we call this discrete aurora and it is only one of several possible types. How we define an auroral type depends on who you talk to. Initially, it would seem that visual appearance would make for the best classifications and this is what scientists did for a long time and in some ways still do. However, the more we learn about what causes the aurora, it becomes clear that looks don't always tell the full story.

Ultimately, the lights we see are generated in one of two ways. Either an electron enters the atmosphere, collides with a molecule and produces light, or a proton enters the atmosphere and does the same thing. The protons are a separate case known as proton aurora that I will leave to other works, such as Gallardo-Lacourt, Frey, and Martinis (2021) to discuss. We will focus on aurora produced by electrons. While the atmospheric interactions that produce this light are similar, not all electrons come from the same place or were pushed into the atmosphere by the same process. To me, the most intuitive way of classifying the aurora is through the process that pushes an electron into the atmosphere, followed by where the electron came from. We will cover this in more detail later, but for now it is enough to understand that the electrons responsible for discrete aurora enter the atmosphere through a process unique to them.

Standing beneath a typical discrete aurora arc in the northern hemisphere, you will witness a band of green light that stretches across the sky in the west-east direction. The arc may be relatively static, staying in place for many minutes and varying in brightness only slightly. Or it could be dynamic, rippling along its length, splitting into multiple arcs, or forming curvy patterns similar to a bunched up curtain. All of these features can evolve and change by the second. You will see mostly green, but if you're lucky might catch a glimpse of blue or red at the bottom or top



Figure 1. Image of discrete aurora above the LAMP rocket mission's Venetie imager enclosure.

of the arc respectively (Chapman, 1962). Figure 1 is an image I took of discrete aurora that came out prior to the LAMP rocket launch, see Section 2.6.

If you were to zoom out, viewing the planet from above, and watch for many nights, you would notice that there is a region where it is common to see the aurora. This region looks like an oblong ring, centered approximately on the pole and with a width stretching from 60° to 75° latitude. Outside the ring, both to the north and south, the aurora is less common. The southern hemisphere contains a similar ring of occurrence. These two regions are called the north and south auroral ovals (Hotea & Fritz, 2017).

1.1.1 The Auroral Substorm

On certain nights it's clear that the aurora are more active. You might observe a stable discrete arc to the north of your location, which will begin to move south. Over the course of minutes, it will continue the southward motion until it suddenly brightens and expands. This new auroral display looks nothing like the original arc. It fills a large portion of the sky with bright and rapidly changing features that can last upwards of 20 minutes. Then, almost as suddenly as it arrived, the show will fade and end. Over one night, this might happen once, or several times. This

event is called an auroral substorm. Nights when there are many substorms are often the visual manifestation of something called a magnetic storm Akasofu (1964).

1.2 Pulsating Aurora

When the dramatic substorm aurora fades, it seems reasonable to head back inside, warm up, and wait for the next show. If you were to take a quick glance at the sky, this would likely seem justified. It would appear like the aurora had disappeared. However, on many nights there is an entirely different dance occurring near the visual threshold of the human eye. This display looks like blobs and patches of diffuse-like aurora that slowly turn on and then off over the course of several to tens of seconds; many with a unique frequency. These patches are different shapes and sizes, but together can span large portions of the sky (Cresswell & Davis, 1966; Johansen & Omholt, 1966; Lessard, 2013). Figure 2 shows a pulsating aurora image sequence from the Poker Flat all-sky camera, a system designed to study the aurora. The green light behind the rocket in Figure 4 is closer to what pulsating aurora would look like to the human eye, only it would be much dimmer.

Pulsating aurora, as it is referred to, often begins during a substorm, but will continue for hours afterwards, sometimes all the way into dawn (Jones, Lessard, Rychert, et al., 2013). Statistically, pulsating aurora occur in a similar, but slightly equatorward region to discrete aurora (Kvifte & Pettersen, 1969). It is also more common to see them from early morning until dawn (Grono & Donovan, 2020). There are different ways of considering pulsating aurora in context with other auroral types. To me, it makes the most sense if we consider pulsating aurora to be an important subset of diffuse-like aurora. Other important subsets of diffuse-like aurora include the faint, homogeneous glow of diffuse aurora, and diffuse auroral arcs (Lui, Perreault, Akasofu, & Anger, 1973; Sergienko, Sandahl, Gustavsson, et al., 2008). The electrons that cause diffuse-like aurora, including pulsating aurora, fall into the atmosphere from a different mechanism compared to discrete aurora. We will discuss these processes shortly.

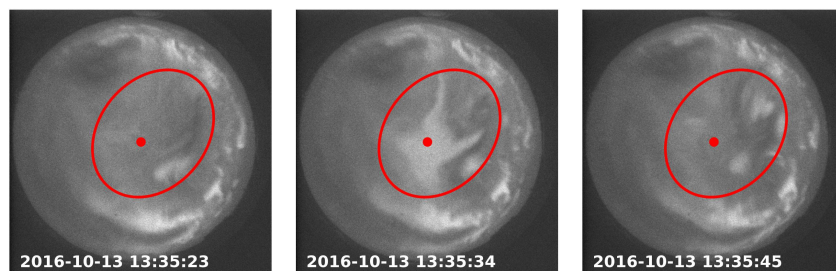


Figure 2. A series of grayscale 428 nm images from the Poker Flat Research Range All Sky Imager with several pulsating aurora patches of differing sizes. The main patch is highlighted by the red oval. The red dot indicates the center of the field of view.

1.3 Imaging The Aurora

Many of the early auroral observations were done by eye. The human eye is remarkably efficient (given its size) in low light conditions. Early cameras could image the aurora, but would require long integration times and were difficult to operate. As technology advanced, so to did our ability to study the aurora. Perhaps most significant has been improvements in imaging devices. Today, the most common instrument to measure the aurora with is an all-sky camera/imager (ASI). At the simplest, these cameras consist of an imaging sensor and lens capable of seeing the entire sky. Systems designed for viewing the aurora are optimized for low light and will sometimes take images in a variety of carefully filtered wavelengths. In addition, they are often automated to take an image every so often all night, every night. During the work on my thesis, I frequently used images taken by the Poker Flat Digital All Sky Camera (DASC) near Fairbanks Alaska and the THEMIS cameras which are scattered across Canada and Alaska. The Poker Flat ASI takes an image once every 12 seconds in three different wavelengths, while the THEMIS ASIs take a white light image once every 3 seconds. Figure 3 is a picture I took looking up at the inside of the LAMP rocket mission's Venetie observatory. The skylights are dome shaped to allow the installed cameras, of which there are three, to view the entire sky. These cameras are tuned to observe the aurora at high frame rates.

ASIs are excellent for automated, long term observations, but they aren't the only way to

image the aurora. Some systems specialize in smaller scale and more rapid auroral features and can be designed to image a small section of the sky at a very high frame rate. These are particularly interesting to study the dynamics of pulsating aurora. Data from one such camera was crucial to my work in Chapter 4.

1.4 Auroral Interactions With The Atmosphere

As we mentioned previously, the Poker Flat ASI is equipped with filters that allow it to image very specific wavelengths of light corresponding to 428 (blue), 558 (green), and 630 (red) nm. When an auroral electron enters the atmosphere it will eventually collide with a neutral molecule. This collision excites an electron in that molecule. Upon decaying to a lower energy state the molecule releases a photon. The 630 nm (red) photons come from a transition in the oxygen atom that, statistically averaged, takes around 110 seconds. For this red light to be emitted in quantity the atmosphere needs to be sparse enough that the average time between collisions is longer than 110 seconds. Thus, we most commonly see this wavelength emitted from altitudes above 150 to 200 km. The 558 nm (green) photons come from a different transition in the oxygen atom, this one takes, on average, around 0.7 seconds and thus occurs most frequently above 100 to 110 km (Whiter, Partamies, Gustavsson, & Kauristie, 2022). The 428 nm (blue) line comes from molecular nitrogen and has a much faster transition time. Because of that faster time, even though this emission peaks at a similar altitude to the 557 nm, it can occur below 95 km and so is comparatively stronger in that region. (Whiter, Partamies, Gustavsson, & Kauristie, 2022; Russell, Luhmann, & Strangeway, 2016).

The green aurora at 100 km is the most common emission. However, by looking at the individual wavelengths and the ratios between those emissions, we can gain information about the altitude of the aurora (McEwen & Bryant, 1978; Nanjo, Hozumi, Hosokawa, et al., 2021). Altitude is valuable information because of how it relates to electron energy. More energetic electrons move faster and penetrate further into the atmosphere. A lower aurora usually indicates more energetic electrons.



Figure 3. Image from the bottom of the LAMP mission Venetie camera observatory. The skylights are dome shaped to allow the camera lenses to view the entire sky. In the image, cameras are installed in three domes, and three are empty.

Another way of estimating auroral height is through triangulation. In this method, observers capture the same auroral feature from multiple different locations. They can then deduce the height of the feature through parallax with background stars (Brown, Davis, Hallinan, & Stenbaek-Nielsen, 1976). Early studies implementing these techniques such as Brown, Davis, Hallinan, and Stenbaek-Nielsen (1976) with triangulation, and (McEwen & Bryant, 1978) with wavelength ratios, found that pulsating aurora occur at a lower altitude (80 to 100 km) compared with discrete aurora (100 to 120 km). This is a strong indication that pulsating aurora contains higher energy electrons.

1.4.1 Rocket Studies of The Aurora

To truly know what is happening within pulsating aurora we need to conduct in-situ measurements. Sounding rockets are essential for this because they fly through the auroral region and can measure valuable information from within the aurora. Whalen, Miller, and McDiarmid (1971) was one of the first sounding rocket missions to investigate pulsating aurora. Using electron detectors they found that pulsating aurora energies were between 25 and 80 keV. Subsequent rockets have confirmed these results (Sandahl, Eliasson, & Lundin, 1980). The most recent mission being the LAMP rocket that launched on March 5, 2022. See Figure 4 for a photo of the LAMP rocket at launch. One downside to rockets is their inability to conduct statistical studies. Due to this constraint, it is difficult to make sweeping statements, using rocket data, about diffuse-like and dynamic aurora, which can be very different on an event-to-event basis.

1.4.2 Incoherent Scatter Radar

The incoherent scatter radar (ISR) is a device that fills the gap between optical observatories and rocket missions. ISRs are large and expensive, but once installed can take quality data for many years. See Figure 5 for an image of the Poker Flat Incoherent Scatter Radar (PFISR). These instruments work by transmitting a narrow beams of radio emissions into a region of the atmosphere called the ionosphere. The ionosphere is the portion of the atmosphere comprised of



Figure 4. Image of the LAMP rocket mission launching into an instance of pulsating aurora. Credit: Justin Hartney

charged particles. These particles become ionized either through solar UV radiation during the day or when energetic particles from the magnetosphere, such as auroral electrons, impact neutral molecules. Electrons in the ionosphere scatter the ISR radio waves, some of which returning back to the device. By measuring the back-scattered signal, ISRs can deduce electron density, temperature, and velocity as a function of altitude and time (Kaeppler, Sanchez, Varney, et al., 2020). With an accurate model of the upper atmosphere, we can estimate differential energy flux using the ionospheric electron density. See Section 5.1 for the specifics on how this works. I made extensive use of this technique for my work in Chapter 2.

1.4.3 Pulsating Aurora And The Atmosphere

Combining visual observations of pulsating aurora with rocket and ISR measurements, it has become clear that these electrons are different to those responsible for discrete aurora. Triangulation, spectral analysis, and ISR electron densities show that, statistically, pulsating aurora occurs at a lower altitude than discrete aurora (Brown, Davis, Hallinan, & Stenbaek-Nielsen, 1976; McEwen & Bryant, 1978; Jones, Lessard, Fernandes, et al., 2009; Samara, Michell, & Redmon, 2015). This indicates that the responsible electrons are more energetic. Rocket missions launched



Figure 5. Image of the Poker Flat Incoherent Scatter Radar (PFISR), located 30 miles north of Fairbanks, Alaska.

into pulsating aurora have directly measured these electrons and confirmed that they can indeed be more energetic (Whalen, Miller, & McDiarmid, 1971). However, these studies have also found that, between and even within the same event, pulsating aurora can be significantly varied. This necessitates a better statistical understanding of pulsating aurora.

One major consequence of energetic pulsating aurora electrons is ozone destruction in the middle atmosphere (Turunen, Kero, Verronen, et al., 2016). This stems from NO_x and HO_x molecules that are produced in collisions between the electrons and the neutral atmosphere. On occasion, extremely high energy electrons can penetrate down to 40 km, and create the NO_x and HO_x in the ozone layer. However, more commonly, collisions produce these molecules at higher altitudes and atmospheric convection transports them to lower altitudes. In some cases this has been linked to an almost 10% reduction in ozone (Verronen, Kero, Partamies, et al., 2021).

The energetic nature of pulsating aurora suggests that these electrons do not originate from the same place as discrete aurora. To understand the different sources we need to examine the planet's magnetic field.

1.5 Earth's Magnetic Field

Before space physics became a separate field of study, Galileo Galilei theorized that the aurora were formed when sunlight reflected off the atmosphere. He thus termed them aurora borealis, which is Latin for northern (borealis) dawn (aurora) (Davis, 1980; Hotea & Fritz, 2017). It's not too surprising that these first theories were incorrect; to understand what causes the aurora we need to visualize an invisible field surrounding the planet, our magnetic field, also called the magnetosphere. Using instruments similar to compasses, scientists like Carl Friedrich Gauss were able to determine that, close to the planet, the magnetic field resembles a dipole Gauss (1832). The mathematical description of a magnetic dipole comes from taking the second order term in the multipole expansion for the magnetic field of an infinitely small current loop (Griffiths, 2013). For a full derivation see Appendix B.1. In spherical coordinates, we can describe the dipole as follows:

$$\vec{B}(\vec{r}) = \frac{2M \cos \theta}{r^3} \hat{r} + \frac{M \sin \theta}{r^3} \hat{\theta} \quad (1.1)$$

where M is the magnetic dipole moment, which for Earth $M \approx 8 \times 10^{15} \text{ T} \cdot \text{m}^3$ (Kivelson & Russell, 1995). It can be useful to picture the magnetic field as a bundle of lines. Motion along a line is tangent to the field direction at every point. Visually, these lines look something like Figure 6. For Earth's field, one way of referring to a specific line is the radial distance where it crosses the equator ($\lambda = 0^\circ$). We refer to this distance, in units of Earth radii, as L . Using this, we can calculate the equation of a magnetic field line as:

$$r = R_E L \cos^2 \lambda \quad (1.2)$$

where R_E is the radius of the earth, and λ is latitude. Throughout this work, I will often refer to a region of space with an L value. At the equator, the region $5 < L < 6$ would be between 5 and 6 R_E away from the center of the planet.

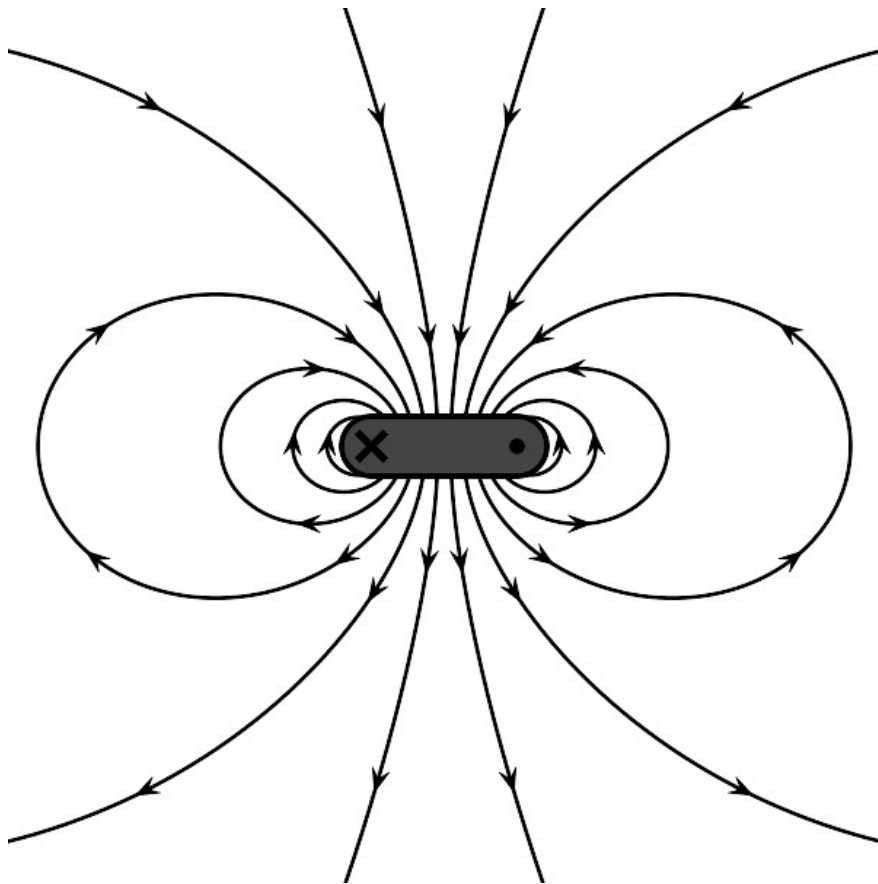


Figure 6. An example dipole field created by a current loop.

1.5.1 Magnetic Local Time

For processes that depend heavily on the magnetic field it is useful to define a new local time. We need a different system because the magnetic and geographic poles are not aligned. The dipole field is slightly off from the rotational axis. Conventional time is based on the geographic poles. When the north pole is directly between you and the sun, it is midnight, when you are directly between the sun and pole, it is noon. Therefore, magnetic local time is based on the location of the magnetic poles. This depends slightly on which magnetic model you use and is a function of longitude, but is around couple hours different from conventional time in Alaska, where our data comes from.

1.5.2 Ground-based Magnetometers

We use magnetometers to measure the magnitude of and fluctuations in Earth’s magnetic field. We can launch these instruments on rockets and satellites, but for now I will focus on ground-based instruments. In particular, SuperMAG, which is a global collaboration that operates more than 300 ground-based magnetometers (Gjerloev, 2009, 2012). These instruments measure magnetic field perturbations in the same coordinates system at a 1-minute temporal resolution. They report measurements in the following format:

$$\vec{B}(t) = [B_N(t), B_E(t), B_Z(t)] \quad (1.3)$$

where N is the local magnetic north direction, E is the local magnetic east direction, and Z is vertically down. With planet-wide measurements, we can construct indices that represent various aspects of how the field is evolving on a global sense. For instance, the Auroral Electrojet (AE) index is a good predictor of nightside auroral activity (Meredith, Horne, Johnstone, & Anderson, 2000; Newell & Gjerloev, 2011a). To calculate this index we let $AE = AU - AL$, where AU and AL are the largest and smallest values in the N direction among all the magnetometers. SuperMAG’s implementation of this index involves over 100 instruments and is known as the SME

index (Newell & Gjerloev, 2011a). Large perturbations in these indices are known as magnetic substorms and correspond well to the visual auroral substorms. This connection indicates that the magnetosphere is a driver of the aurora and that substorms are a central component.

1.6 The Magnetic Field In Context And Source of Discrete Aurora

If Earth and the magnetosphere existed in a vacuum there would be no need for magnetic indices because the field would not change. Clearly this is not true, so there must be something outside the system acting on it. At the end of the day, this something is the Sun. Our star is constantly spewing out plasma to create the solar wind. The solar wind travels radially out from the sun and carries its own magnetic field called the interplanetary magnetic field (IMF). Because the Sun spins, the solar wind and IMF trace out a spiral shape known as the Parker spiral. When the solar wind reaches us, our magnetosphere deflects it, but doesn't get away unscathed. The solar wind imparts a pressure, which deforms the magnetosphere, compressing it on the side closest to the Sun. Additionally, the IMF can couple with Earth's magnetic field. As the solar wind moves past the planet the IMF pulls and stretches Earth's field away from the Sun. If we could see magnetic field lines with our eyes, the magnetosphere would look something like Figure 7.

If the solar wind were constant, again, nothing would change. However, the solar wind does vary. Sometimes it flows faster, other times slower. Occasionally a region of strong magnetic fields on the surface of the Sun, associated with sun spots, will burst. This releases a fast, dense clump of plasma called a coronal mass ejection (CME). When a CME reaches Earth it can trigger a geomagnetic storm if the IMF is oriented southward. In this geomagnetic storm the IMF will couple with Earth's magnetic field and stretch it out behind the planet. Eventually it becomes so stretched that it uncouples, allowing the field to snap back to a dipolar shape in a process called reconnection. As the field snaps back it can carry electrons with it. Electric fields aligned parallel to the magnetic field then accelerate these electrons into the atmosphere where they cause discrete and substorm aurora (Korth, Zhang, Anderson, et al., 2014; Schroeder, Howes, Kletzing, et al., 2021).

1.6.1 Atmospheric Current Systems

During instances of auroral activity electrons stream into the atmosphere. This flow of charge produces magnetic field-aligned currents that originate in the magnetosphere, pass through the atmosphere, and then close back to the magnetosphere (Kivelson & Russell, 1995). Within the atmosphere, between around 90 to 140 km, this current is described as

$$j = \sigma E = n_i e (v_i - v_e) \quad (1.4)$$

where σ is the conductivity, and j can have components in three different directions. The Pedersen current is perpendicular to the magnetic field and parallel to the electric field, the Hall current is perpendicular to both, and the field-aligned or Birkeland current is parallel to the magnetic field. At higher altitudes electrons and ions would tend to drift in the same $\vec{E} \times \vec{B}$ direction, but at lower altitudes collisions become important and lead to a separation of the charge. These current systems, and the corresponding conductivities, are an essential component of discrete auroral physics, but they tend to be ignored in the case of diffuse-like aurora. This work is no exception and, besides this section, we will not consider the atmospheric currents in this thesis. However, there has been some recent work looking at how field aligned currents relate to pulsating aurora that we thought was relevant to cover. In their study, using the THEMIS ASIs and Swarm satellites, Gillies, Knudsen, Spanswick, et al. (2015) found that, for pulsating patches with clear boundaries, there were strong downward currents poleward and equatorward of the patch. This was matched by a weaker upward current in the patch interior. These findings indicate that currents carried by pulsating aurora electrons might close horizontally and return at the edge of the patch.

While not directly related to pulsating aurora, Olifer, Feltman, Ghaffari, et al. (2021) found that, in the dawn sector, the Pedersen conductivity was larger in the upward current region than in the downward. However, for the dusk sector the conductivities in the two regions were similar. They hypothesized that this asymmetry could be due to energetic electron precipitation that occurs more frequently after magnetic midnight. As we will show in Chapter 2, energetic electron pre-

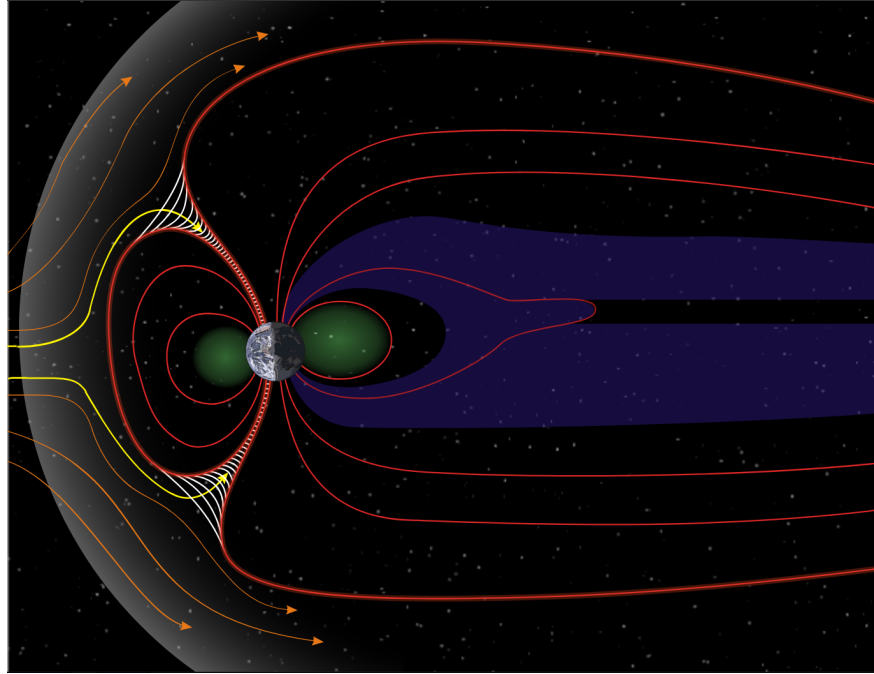


Figure 7. Artistic depiction of Earth's magnetosphere. The red lines represent Earth's magnetic field. The orange and yellow lines represent the incoming solar wind. The blue region is the plasma sheet. The green region represents the Van Allen radiation belts. Note, the planet is not to scale. Image credit: William Crochot, NASA.

cipitation is often associated with pulsating aurora. The findings of studies such as these indicate that the relationship between currents and pulsating aurora is an important dynamic that should be considered in future work.

1.7 The Outer Van Allen Radiation Belt And Source of Pulsating Aurora

Surrounding Earth are regions of magnetically trapped, highly energetic particles that drift around the planet. These regions are called the Van Allen radiation belts, named after University of Iowa physics department chair, James Van Allen, who discovered them. In space physics, particle energy is commonly referred to in units of electron-volts (eV), where $1 \text{ eV} = 1.6 \times 10^{-19} \text{ Joules}$. Radiation belt particles can range up to MeV energies. For context, discrete auroral electrons have energies typically between 1 to 10 keV, while pulsating aurora can range all the way up to 100 keV.

Particles in the radiation belts comprise a plasma. For a gas of charged particles to be

considered a plasma, it needs to meet a couple parameters. The first is that the gas must be quasi-neutral. This means that there are approximately the same number of positively charged particles as negative or

$$n_e \approx n_i \quad (1.5)$$

where e and i correspond to electrons (negative) and ions (positive). At a macroscopic scale this approximation holds. However, if we look closer, we will see that because the ions, usually protons, are much heavier than electrons, they will tend to attract electrons to them. Past a certain distance this perturbation will diminish. The distance over which this occurs is the Debye length.

$$\lambda_D^2 = \frac{\epsilon_0 k_B T_e}{n_0 e^2} \quad (1.6)$$

where k_B is the Boltzmann constant, n_0 is the number density assumed by quasi-neutrality, and T_e is the temperature of the electrons. See Appendix B for the derivation of this value. The number of particles within one Debye length of an ion is given by the plasma parameter, $N_D = n_0 \lambda_D^3$. For a plasma to behave ideally it must hold that $N_D \gg 1$.

As the name implies, there are usually two radiation belts. The inner belt occupies the region $1.5 < L < 2$, while the outer belt is located between $3 < L < 7$ (Van Allen, 1959). However, the outer belt is highly dynamic and can change location and size depending on geomagnetic conditions. In some cases even splitting into 2 to 3 smaller belts (Baker, Kanekal, Hoxie, et al., 2013). For the purpose of this work, we will focus only on the outer radiation belt. To understand how these belts form, we will examine what a charged particle does in Earth's dipole field. For the full derivation, see Appendix B.

1.7.1 Drifts

First we will look at why radiation belt electrons drift around the planet. These derivations, will skip many of the steps, for a more complete derivation see Appendix B. We will start with a simple uniform field in the \hat{z} direction. If we inject a charged particle into this field with a velocity

\vec{v} that is perpendicular to the magnetic field, it will gyrate around a field line as shown by the harmonic equation

$$\ddot{v}_{x,y} = - \left(\frac{qB}{m} \right)^2 v_{x,y} \quad (1.7)$$

where $v_{x,y}$ refers to either the x or y component of velocity, q is the charge of the particle, m is the mass of the particle, and B is the magnetic field strength. For an electron ($q < 0$), this gyration is in the right-handed sense. From now on I will only consider the electron case. The frequency of this oscillation in radians per second for an electron is

$$\Omega_e = \frac{q_e B}{m_e} \quad (1.8)$$

We'll refer to this as the electron cyclotron frequency and it is an important quantity for space plasma physics. Finally, the radius of this gyration is given by

$$\rho_c = \frac{m_e v_{\perp}}{q_e B} \quad (1.9)$$

where v_{\perp} is the component of the velocity perpendicular to the magnetic field. This this simple example $v = v_{\perp}$, though usually this isn't the case.

The angle between an electron's velocity and the magnetic field is the pitch angle α . If $\alpha < 90^\circ$ the electron will still gyrate around the magnetic field, but now also has an additional velocity component parallel to the field and $v^2 = v_{\parallel}^2 + v_{\perp}^2$. The result is an indefinite spiral motion along the field, assuming the field remains uniform. In Earth's dipole field, that is not a valid assumption. From Equation 1.1 we can see that the magnetic field is not constant along \hat{r} or $\hat{\theta}$. To explore this, let us first consider an electron with $\alpha = 90^\circ$ at the magnetic equator. When it is furthest from the planet B will be smaller and hence, from Equation 1.9, the radius will be larger. The opposite is true closer to the planet. This will cause the electron to drift perpendicular to the

magnetic field and in the eastward direction. The velocity of this gradient drift is described by

$$\vec{v}_\nabla = \frac{m_e v_\perp^2}{2q_e B^2} \hat{B} \times \nabla_\perp B \quad (1.10)$$

where \hat{B} is a unit vector in the direction of \vec{B} .

Now we'll assume that $\alpha < 90^\circ$, so the electron will spiral around a magnetic field line. However, a dipole field is curved and thus an electron travelling along it will feel a centripetal force. This force will cause another motion, which we call the curvature drift.

$$\vec{v}_c = \frac{m_e v_\parallel^2}{q_e B^2} \hat{B} \times \nabla_\perp B \quad (1.11)$$

Notice that the gradient and curvature drifts are very similar and point in the same direction. It is convenient to combine them into a gradient-curvature drift.

$$\vec{v}_{cg} = \frac{m v^2}{2q B^2} (1 + \cos^2 \alpha) \hat{B} \times \nabla_\perp B \quad (1.12)$$

The electrons that cause pulsating aurora are strongly linked to the gradient curvature drift. Therefore, it would be interesting to see how fast an electron would drift in a perfect dipole at the equator. The gradient-curvature drift then becomes

$$\vec{v}_{cg} = -\frac{3KE_{\text{total}} L^2 R_E^2}{q_e M} (1 + \cos^2 \alpha) \hat{\phi} \quad (1.13)$$

where we've replaced $m_e v^2/2$ with the electron's kinetic energy KE , r with L , and used the fact that $\vec{B} = M/r^3 \hat{\theta}$ at the equator.

Simplifying this further, the known values $R_E = 6.38 \times 10^6 \text{ m}$, $q = -1.6 \times 10^{-19} \text{ C}$, and $M = 8 \times 10^{15} \text{ T} \cdot \text{m}^3$ combine such that $R_E^2/q_e M = 3.18 \times 10^{16} [\text{s} \cdot \text{kg}^{-1} \cdot \text{m}^{-1}]$ (Kivelson & Russell, 1995; Mamajek, Prsa, Torres, et al., 2015). Finally, converting Joules to electron volts we get the

drift velocity of an electron at the equator, which will move in the $\hat{\phi}$ (eastward) direction:

$$v_{cg} = 1.53 \times 10^{-2} KE_{\text{total}} L^2 (1 + \cos^2 \alpha) [\text{m} \cdot \text{s}^{-1}] \quad (1.14)$$

1.7.2 Bounce Motion

As we showed in the previous section, electrons have a tendency to drift eastward, but what exactly is causing them to remain in the magnetic field? To answer this, we have to understand a property of charged particles in a magnetic field called the magnetic moment.

$$\mu = \frac{\frac{1}{2}mv_{\perp}^2}{B} = \frac{\left(KE_{\text{total}} - \frac{1}{2}mv_{\parallel}^2\right)}{B} \quad (1.15)$$

One property of the magnetic moment is that it remains constant, even as the electron's energy changes. However, this assumes the field changes slowly, meaning that the changes over a single gyration will be small. If μ is constant and the kinetic energy is constant then, for a larger magnetic field strength, the electron's velocity parallel to the magnetic field will be smaller. As B continues to increase the parallel velocity will go to zero. This is known as the mirror point. Here, the electron will stop moving and then begin moving in the opposite direction. For an electron following a dipole field line, B is weakest at the equator and strongest near the poles. Therefore, the electron will experience a mirror point near each pole causing it to bounce back and forth between the two poles, hence the magnetic trap.

However, we also have to remember that Earth has an atmosphere. If an electron's mirror point is at a low enough altitude it could collide with a neutral molecule, breaking the trap. What altitude this will happen at? In Appendix B we show that the mirror point will occur when

$$B_{\text{mirror}} = \frac{B_0}{\sin^2 \alpha_0} \quad (1.16)$$

where α_0 and B_0 are the pitch angle and magnetic field at some initial point. For simplicity, we'll let this be at the magnetic equator. Using the magnetic field at the equator and Equation 1.2 this

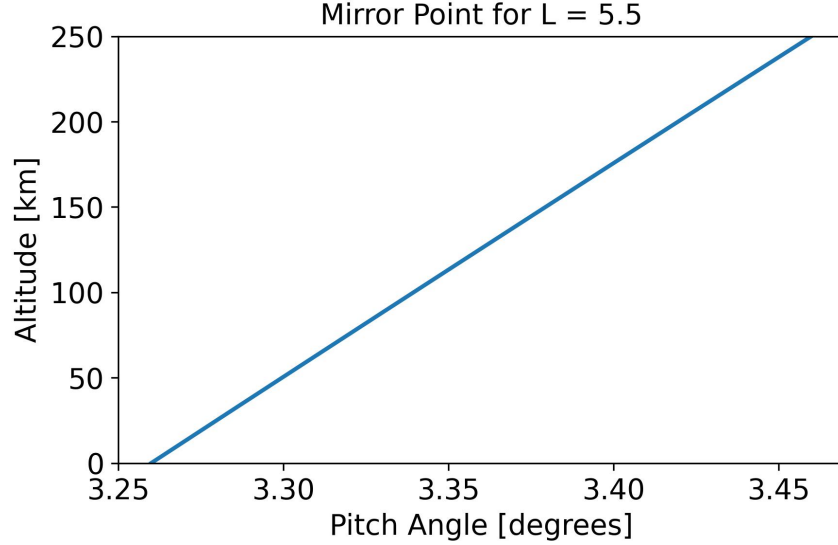


Figure 8. Altitude of the mirror point for particles with various pitch angles as measured at the magnetic equator on field line $L = 5.5$. This corresponds to a latitude of 64.8° , which is in the auroral oval.

becomes:

$$\frac{r_{\text{mirror}}^6}{L^6 R_E^6 \sin^4 \alpha_0} = 4 - \frac{3r_{\text{mirror}}}{R_E L} \quad (1.17)$$

To solve for the altitude we let $r_{\text{mirror}} = R_E + \delta r$, where δr is the altitude.

$$\frac{1}{\sin^4 \alpha_0} \left(\frac{1}{L} + \frac{\delta r}{LR_E} \right)^6 = 4 - 3 \left(\frac{1}{L} + \frac{\delta r}{LR_E} \right) \quad (1.18)$$

Letting $x = \left(\frac{1}{L} + \frac{\delta r}{LR_E} \right)$, the equation we need to solve is then

$$\frac{1}{\sin^4 \alpha_0} x^6 + 3x - 4 = 0 \quad (1.19)$$

Alternatively we can plot Eq. 1.18 over a variety of different altitudes to get Figure 8. When an electron collides with the atmosphere we say that it has precipitated. Assuming collisions will be frequent below 200 km, the pitch angles that cause electron precipitation are small. This range is called the loss cone. Here it is approximately 3.42° .

We've now built up a mathematical description of the outer Van Allen radiation belt. Elec-

trons spiral around magnetic field lines, bouncing back and forth between mirror points near each pole. This motion, combined with the average eastward drift traces out the donut shape of the radiation belt. See Figure 10 for an example of what each of these motions look like. To understand these three motions better we can get a rough estimate for the timescales of each. Figure 9 shows the bounce and gradient curvature drift periods for common pulsating aurora L-shells and energies using electrons with 5° and 90° pitch angles respectively. To see how we've done the calculations, we will estimate these periods for a 30 keV electron located on the equator at $L = 5$ and with a pitch angle $\alpha = 45^\circ$. The magnetic field here will be

$$B = \frac{m_e}{r^3} = \frac{8 \times 10^{15} \text{ T} \cdot \text{m}^{-3}}{(5 \cdot 6.4 \times 10^6 \text{ m})^3} = 2.44 \times 10^{-7} \text{ T} \quad (1.20)$$

It then follows that the electron cyclotron frequency will be

$$f_{ce} = \frac{q_e B}{2\pi m_e} = \frac{1.6 \times 10^{-19} \text{ C} \cdot 2.44 \times 10^{-7} \text{ T}}{2\pi \cdot 9.1 \times 10^{-31} \text{ kg}} \approx 7 \times 10^3 \text{ s}^{-1} \implies \tau_{ce} = 1.4 \times 10^{-4} \text{ s} \quad (1.21)$$

The bounce motion is our next quickest timescale. We can calculate this period with the following equation given by Soni, Kakad, and Kakad (2021).

$$\tau_b = 4 \frac{r}{v} \left[1.38 - 0.64(\sin \alpha)^{0.75} \right] \quad (1.22)$$

where r is the equatorial radial distance and v is the velocity of the electron. Before going any further we should check if our electron is in the relativistic range. To do this we first look at the mass energy of the electron $E_m = m_e c^2 = 8.19 \times 10^{-14} \text{ J}$. The kinetic energy of the electron $KE = 30 \text{ keV} = 30 \times 10^3 \cdot 1.6 \times 10^{-19} \text{ J} \cdot \text{eV}^{-1} = 4.8 \times 10^{-15} \text{ J}$. This is roughly 5% of the mass energy and so we should be fine making the approximation $KE = \frac{m}{2} v^2$.

$$\tau_b = 4 \cdot 5 \cdot 6.4 \times 10^6 \text{ m} \sqrt{\frac{9.1 \times 10^{-31} \text{ kg}}{2 \cdot 30 \times 10^3 \cdot 1.6 \times 10^{-19} \text{ J}}} \left[1.38 - 0.64(\sin 45^\circ)^{0.75} \right] \approx 1.1 \text{ s} \quad (1.23)$$

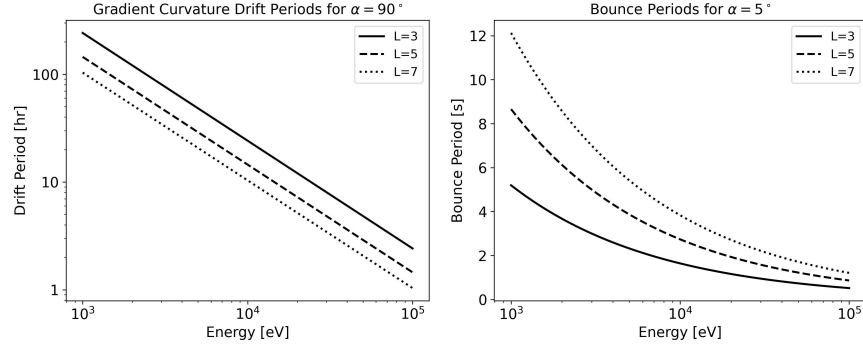


Figure 9. Gradient curvature drift and bounce periods over common pulsating aurora L-shells and energies. We've calculated the gradient curvature drifts for a 90° pitch angle. We've calculated the bounce period for a 5° pitch angle, which is close to the loss cone.

Finally, for the drift motion we can use 1.14, so get a drift velocity of $v_{cg} \approx 20 \times 10^3 \text{ m} \cdot \text{s}^{-1}$. The period of this motion will then be

$$\tau_{cg} = \frac{2\pi \cdot 5 \cdot 6.4 \times 10^6 \text{ m}}{20 \times 10^3 \text{ m} \cdot \text{s}^{-1}} \approx 10,000 \text{ s} \approx 2.75 \text{ hr.} \quad (1.24)$$

From these motions, it becomes clear that the dipolar approximation of the magnetosphere is critical to the outer radiation belt. Assuming an unchanging system, the electrons will remain trapped and the radiation belt will be static. However, this is usually not a good assumption. For instance, during a geomagnetic storm the magnetosphere gets compressed, sometimes so much that the outer radiation belt is no longer in the dipole field. When this is the case, electrons are no longer trapped and can escape into space. There are a multitude of other processes that can change the radiation belts. The one we'll focus on for the rest of this thesis are waves and their interaction with electrons.

1.7.3 Plasma Waves

The outer radiation belt is a plasma permeated by Earth's magnetic field. Because a plasma is composed of a collection of charged particles it reacts to electric and magnetic fields. Waves in those fields will thus perturb the plasma. This is known as an electromagnetic wave. Space

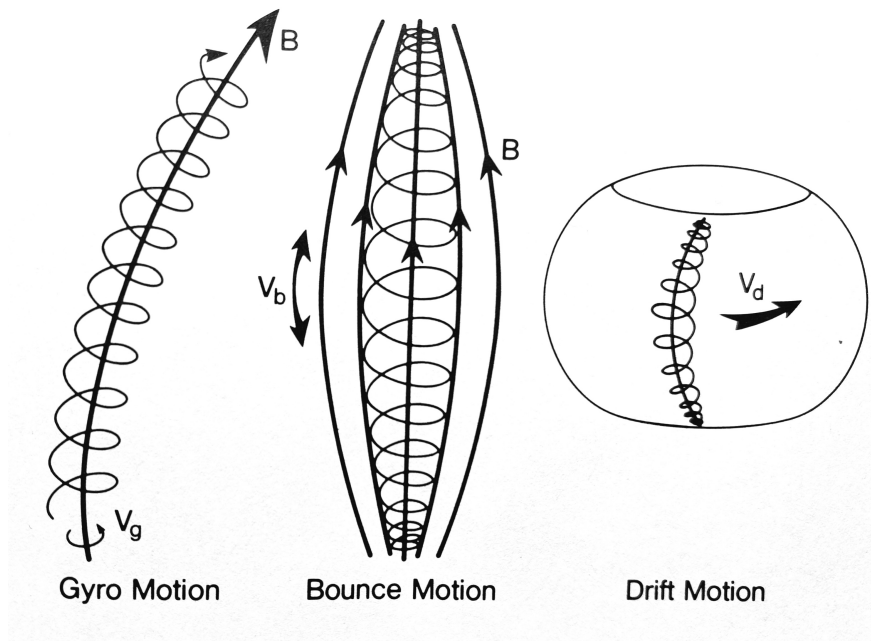


Figure 10. Image from Kivelson and Russell (1995) depicting the three most important electron motions for pulsating aurora in Earth's magnetic field. Electrons gyrate around field lines, bounce between mirror points near each pole, and drift eastward around the planet. For a 30 keV electron, located at $L = 5$, with a pitch angle $\alpha = 45^\circ$ at the equator, the respective timescales of these motions are 1.4×10^{-4} s, 1.1 s, and 1×10^4 s.

plasmas also behave like a gas, so they can have density and pressure waves similar to sound waves. A plasma wave is a combination of both these phenomena and so behaves differently from either. We'll start with the momentum equation, see Equation B.69. Next we will assume that solutions to this equation are periodic such that

$$\vec{y} = \vec{y}_0 e^{i(\vec{k} \cdot \vec{r} - \omega t)} \quad (1.25)$$

where \vec{y} is a perturbed quantity such as the electric field or current density, \vec{k} is the wave number, \vec{r} is the position vector and ω is the frequency. As we show in Appendix B, assuming solutions of this form, we can relate the bulk perturbed velocity of the particles \vec{u} to the electric field with:

$$\omega^2 \vec{u} - \frac{\gamma_s K T_e}{m_e} \vec{k} (\vec{k} \cdot \vec{u}) = i \omega \frac{q_e}{m_e} (\vec{E} + \vec{u} \times \vec{B}_0) \quad (1.26)$$

where γ_e is the ratio of specific heats for the electrons, K is the Boltzmann constant, and T_e is the temperature of the electrons. The radiation belts can be considered a cold plasma such that

$$\frac{\omega^2}{k^2} \gg \frac{\gamma_e K T_e}{m_e} \quad (1.27)$$

This allows us to ignore the effects of plasma pressure in Equation 1.26, which then becomes

$$\vec{u} = i \frac{q_e}{\omega m_e} (\vec{E} + \vec{u} \times \vec{B}_0) \quad (1.28)$$

We can express this in terms of the current density, \vec{j} given that $\vec{J} = \vec{u} n_e q_e$

$$j_x = i \frac{\omega_{pe}^2}{(\omega^2 - \Omega_e^2)} \epsilon_0 (\omega E_x + i \Omega_e E_y) \quad (1.29)$$

$$j_y = i \frac{\omega_{pe}^2}{(\omega^2 - \Omega_e^2)} \epsilon_0 (\omega E_y - i \Omega_e E_x) \quad (1.30)$$

Here the electron plasma frequency

$$\omega_{pe} = \frac{n_e q_e^2}{\epsilon_0 m_e} \quad (1.31)$$

is the frequency that a perturbed electron will naturally oscillate at in a plasma. We can get another equation relating the current density and electric field by combining Faraday's law and the time derivative of Ampere's law. Again, assuming the harmonic solution, this leads to:

$$(\mu^2 - 1) \vec{E} - \mu^2 \hat{k} (\hat{k} \cdot \vec{E}) = \frac{i}{\omega \epsilon_0} \vec{j} \quad (1.32)$$

where the refractive index $\mu = kc/\omega$. Then by combining Equations 1.29, 1.30, and 1.32 for a wave propagating parallel to the ambient magnetic field, such that $\hat{k} \parallel \vec{B}_0$, we get the following dispersion relation:

$$\mu^2 = 1 - \frac{\omega_{pe}^2}{\omega (\omega \pm |\Omega_e|)} \quad (1.33)$$

A dispersion relation relates the wave number k to the wave frequency ω . There is a resonance in this equation when the refractive index goes to infinity. This occurs if we use the negative sign and let $\omega = |\Omega_e|$. The solution looks like $E_x + iE_y = 0$. Because the y-component is imaginary, it lags the x-component by 90° or $1/4$ period. This represents a right-hand circularly polarized wave (R mode). The positive sign corresponds to a left-hand polarized wave (L mode).

In both cases, the electric field rotates around the ambient magnetic field. Electrons gyrate around the magnetic field in a right-handed sense, thus energy can transfer between electron and wave when an R-mode wave oscillates at the cyclotron frequency. However, it is important to note that the resonance must take place in the electron's frame of reference. Because of this, electrons with different energies will resonate with waves of different frequencies.

While wave frequency is a continuous spectrum, it is possible to make some distinctions. Since the refractive index cannot be less than 0, there is a cutoff frequency when $\mu^2 = 0$. For R-mode waves this is

$$\omega_R = \sqrt{\omega_{pe}^2 + \frac{\Omega_e^2}{4}} + \frac{|\Omega_e|}{2} \quad (1.34)$$

There are two branches of the R-mode waves. One with $\omega > \omega_R$, the other with $\omega < |\Omega_e|$. The latter is what we are interested in and are known as whistler-mode waves. Even more specific, chorus are a type of whistler-mode waves that fall between Ω_e and $\Omega_e/10$. There happens to be a clear gap, due to Landau damping, in wave power at $\Omega_e/2$, such that lower-band chorus waves fall between $\Omega_e/2$ and $\Omega_e/10$ and upper-band between Ω_e and $\Omega_e/2$ (Bortnik, Inan, & Bell, 2006).

1.7.4 Pitch Angle Scattering

As we showed in Appendix B, the resonance condition between chorus waves and non-relativistic electrons is

$$v_{\parallel} \cos \theta = v_p \frac{\omega - \Omega_e}{\omega} \quad (1.35)$$

where v_{\parallel} is the electron velocity parallel to the magnetic field and v_p is the phase velocity of the chorus wave. Because chorus waves occur at frequencies below the electron cyclotron frequency (Ω_e), the wave and electron need to be travelling opposite, such that the Doppler-shifted frequencies match.

Equation 1.35 doesn't directly solve for the energy, instead we get the parallel velocity. If we know the particles pitch angle we can determine the total velocity and from this the kinetic energy. To get a sense of these resonant energies we'll explore what they would be for some common situations. We'll consider whistler mode waves at the magnetic equator on the field line $L = 5$. At this location, from Equation 1.1 the magnetic field strength will be

$$|\vec{B}| = B_{\theta} = \frac{M}{r^3} \approx \frac{8 \times 10^{15} \text{ T} \cdot \text{m}^3}{(5 \cdot 6.4 \times 10^6 \text{ m})^3} \approx 2.4 \times 10^{-7} \text{ T} = 240 \text{ nT} \quad (1.36)$$

In this magnetic field, the electron cyclotron frequency is

$$\Omega_e = \frac{q_e B}{m_e} = \frac{(1.6 \times 10^{-19} \text{ C}) (2.4 \times 10^{-7} \text{ T})}{(9.1 \times 10^{-31} \text{ kg})} \approx 4.2 \times 10^4 \text{ rads} \cdot \text{s}^{-1} \quad (1.37)$$

Now we need to determine the phase velocity of the wave. Using the knowledge that $v_p = \omega/k$,

and that $\mu = kc/\omega = c/v_p$, we can use Equation 1.33 to solve for v_p . To do that we need to solve for ω_{pe} . From Equation 1.31, this is possible if we know the electron density.

Based on previous models, we'll assume the electron density in this region is 10 cm^{-3} or $1 \times 10^7\text{ m}^{-3}$ (Sheeley, Moldwin, Rassoul, & Anderson, 2001). We next calculate the electron plasma frequency.

$$\omega_{pe}^2 = \frac{n_e q_e^2}{\epsilon_0 m_e} = \frac{(1 \times 10^7\text{ m}) (1.6 \times 10^{-19}\text{ C})^2}{(8.85 \times 10^{-12}\text{ F} \cdot \text{m}^{-1}) (9.1 \times 10^{-31}\text{ kg})} \approx 3.2 \times 10^{10}\text{ rad}^2 \cdot \text{s}^{-2} \quad (1.38)$$

It then follows, from Equation 1.33, that the phase velocity of the wave is

$$v_p^2 = c^2 \left[1 - \frac{3.2 \times 10^{10}\text{ rad}^2 \cdot \text{s}^{-2}}{\omega(\omega - \Omega_e)} \right]^{-1} \quad (1.39)$$

Before substituting in the value we calculated for Ω_e , we'll determine what wave frequencies, ω , that we'd like to solve v_p for. The two frequencies that define lower-band chorus waves are $\Omega_e/2$, and $\Omega_e/10$. For each of these: $\omega(\omega - \Omega_e) = -\Omega_e^2/4$, and $-9\Omega_e^2/100$. Substituting these into Equation 1.39 we get that $v_p^2 = 1.24 \times 10^{15}\text{ m}^2 \cdot \text{s}^{-2}$, and $4.47 \times 10^{14}\text{ m}^2 \cdot \text{s}^{-2}$ respectively. From Equation 1.35

$$v_{\parallel}^2 = v_p^2 \left(\frac{\omega - \Omega_e}{\omega} \right)^2 \quad (1.40)$$

For $\omega = \Omega_e/2$ and $\Omega_e/10$ this becomes

$$v_{\parallel, \Omega_e/2}^2 = v_p^2 = 1.24 \times 10^{15}\text{ m}^2 \cdot \text{s}^{-2} \quad (1.41)$$

and

$$v_{\parallel, \Omega_e/10}^2 = 9^2 v_p^2 = 3.62 \times 10^{16}\text{ m}^2 \cdot \text{s}^{-2} \quad (1.42)$$

From here the energy of the electron will be

$$KE = \frac{m_e}{2} \left(v_{\parallel}^2 + v_{\parallel}^2 \tan^2 \alpha \right) \quad (1.43)$$

where α is the pitch angle. Assuming $\alpha = 45^\circ$, the resonant energies for the two frequencies are

$$KE_{\Omega_e/2} [\text{eV}] = \frac{(1.13 \times 10^{-15} \text{ J})}{1.6 \times 10^{-19} \text{ J} \cdot \text{eV}^{-1}} \approx 7 \text{ keV} \quad (1.44)$$

$$KE_{\Omega_e/10} [\text{eV}] = \frac{(3.29 \times 10^{-14} \text{ J})}{1.6 \times 10^{-19} \text{ J} \cdot \text{eV}^{-1}} \approx 206 \text{ keV} \quad (1.45)$$

For a larger pitch angle of $\alpha = 75^\circ$ these would be

$$KE_{\Omega_e/2} = 17 \text{ keV} \quad \text{and} \quad KE_{\Omega_e/10} = 490 \text{ keV} \quad (1.46)$$

For a smaller pitch angle near the loss cone of $\alpha = 5^\circ$

$$KE_{\Omega_e/2} = 3.8 \text{ keV} \quad \text{and} \quad KE_{\Omega_e/10} = 112 \text{ keV} \quad (1.47)$$

In this resonant interaction energy is transferred from the electron to the chorus wave. The parallel velocity of the electron actually increases slightly, but the perpendicular velocity decreases more. This lowers both the electrons energy and the pitch angle. The change can be described with the equation

$$\Delta\alpha = \frac{\tan \alpha}{2(1 + \tan^2 \alpha)} \left[\frac{\Omega_e}{\omega \sin^2 \alpha} + \frac{\Omega_e - \omega}{\omega \cos^2 \alpha} \right] \frac{\Delta KE}{KE} \quad (1.48)$$

Again, see Appendix B for a full derivation of this equation.

1.7.5 Lower-band Chorus As a Driver of Pulsating Aurora

As we showed in Section 1.7.3, when chorus waves resonate with an electron they can reduce the pitch angle. If this happens enough, the electron will enter the loss cone and precipitate into the atmosphere. In addition, the resonant energies we derived align with the electron energies measured in the atmosphere during pulsating aurora (Whalen, Miller, & McDiarmid, 1971; Sandahl, Eliasson, & Lundin, 1980; Tesema, Partamies, Tyssøy, et al., 2020). Finally, we know that chorus wave intensity often modulates quasi-periodically with similar periods to pulsating aurora

patches (A. N. Jaynes, Lessard, Takahashi, et al., 2015). These points beg the question, are lower-band chorus waves responsible for pulsating aurora? To some degree, previous work has provided an answer. Nishimura, Bortnik, Li, et al. (2010) and the follow up Nishimura, Bortnik, Li, et al. (2011) identified near one-to-one correlations between modulating lower-band chorus measured by the THEMIS spacecraft and pulsating aurora at the satellites magnetic footprint. The magnetic footprint corresponds to the point where the magnetic field line, that the satellite is on, crosses the planet's surface. Following this, A. N. Jaynes, Lessard, Rodriguez, et al. (2013) observed one-to-one correlations with pulsating aurora and equatorial precipitating electrons. This confirmed the theory that pulsating aurora electrons originate near the equator. These findings were later corroborated by Kasahara, Miyoshi, Yokota, et al. (2018) and Hosokawa, Miyoshi, Ozaki, et al. (2020), both of which observed pulsating aurora corresponding to chorus waves and energetic particle precipitation near the equator, as measured by the Arase spacecraft. While it is clear that lower-band chorus can cause pulsating aurora, these studies have only investigated a handful of events, so the statistical significance is still an open question. It is that question which guided my research in Chapter 3. However, the story begins in Chapter 2 where we uncovered a characteristic timescale associated with > 30 keV pulsating aurora electrons.

CHAPTER 2: THE ENERGY CONTENT OF PULSATING AURORA

2.1 Introduction

Pulsating aurora are much different than the bright curtains of discrete aurora that often precede them. Diffuse-like and barely visible to the naked eye, this type of aurora is most often observed a few hours after magnetic midnight (e.g., Oguti, Kokubun, Hayashi, et al., 1981; Jones, Lessard, Rychert, et al., 2011). Often lasting for many hours, pulsating aurora can cover large portions of the sky and in some cases expand over entire sections of the auroral region (Jones, Lessard, Rychert, et al., 2013). Using SuperDarn and imager data, E. Bland, Tesema, and Partamies (2021) found that around half of pulsating aurora events extend between 4-5 hours of magnetic local time and between 62° to 70° in magnetic latitude. Over this area, auroral patches blink on and off with periods ranging up to around 20 seconds Davis (e.g., 1978) and Lessard (2013). Adding to the auroral display, individual patches can be remarkably varied with differing periods, shapes, and sizes typically between 10s to 100s of kilometers (Johnstone, 1978; Lessard, 2013). Figure 11 panels A1-A3 shows a typical example of pulsating aurora that occurred on October 13, 2016 over the Poker Flat Research Range. The red oval highlights a patch that turns on and off during the three images.

Numerous studies have shown that the electrons responsible for pulsating aurora originate in the equatorial region of the outer Van Allen radiation belt. These electrons are pitch-angle scattered into the upper-atmosphere through wave-particle interactions, most likely with lower-band chorus waves (Nishimura, Bortnik, Li, et al., 2010; Nishimura, Bortnik, Li, et al., 2011; A. N. Jaynes, Lessard, Rodriguez, et al., 2013; Kasahara, Miyoshi, Yokota, et al., 2018; Hosokawa, Miyoshi, Ozaki, et al., 2020). Previous studies have found that the energy range of pulsating aurora electrons is substantially higher than other auroral types, ranging between 10s to 100s of keV Whalen, Miller, and McDiarmid (e.g., 1971) and Sandahl, Eliasson, and Lundin (1980). Tesema, Partamies, Tyssøy, et al. (2020) verified this statistically using 253 pulsating aurora events observed by the DMSP, POES, and FAST spacecraft. Within a single event, the total energy flux and hardness

can vary. Jones, Lessard, Fernandes, et al. (2009) notes often seeing a decrease in the differential energy flux of 0.5 to 32.5 keV electrons throughout an event. Hosokawa and Ogawa (2015) found, using the European Incoherent Scatter Radar, that the energy spectrum of pulsating aurora is harder when a patch is “on” versus when it is “off” with only background aurora present.

Some studies have attempted to classify different types of pulsating aurora. For instance, Royrvik and Davis (1977) classified events into patches, arcs, and arc segments. More recently, Grono and Donovan (2018) made a distinction between the quickly varying amorphous pulsating aurora (APA), more regular patchy pulsating (PPA) aurora, and non-pulsating patchy aurora (nPPA). Tesema, Partamies, Nesse Tyssøy, and McKay (2020) used incoherent scatter radar to look at the electron density profile between APA, PPA, and nPPA. They found that PPA and nPPA were associated with enhanced electron densities below 100 km when compared with APA.

Several papers regarding the height of pulsating aurora indicate that there may be a relation between peak differential energy flux of precipitating electrons and substorm onset. In the two events that Oyama, Kero, Rodger, et al. (2017) analyzed, they found a drop to lower altitudes following substorm onset in the atmospheric electron densities of pulsating aurora. This would indicate an influx of higher energy electrons capable of penetrating further into the atmosphere. These results are similar to the statistical study of Hosokawa and Ogawa (2015) who showed that the electron density profile of pulsating aurora extends lower in altitude during periods with a large AE index (> 500 nT). This previous work is a strong indicator of the increase in higher energy electrons, or hardening, during geomagnetic activity that coincides in time with an increase in AE index. However, altitude is only a proxy for energy because the relation between the two is not one-to-one. Wing, Gkioulidou, Johnson, et al. (2013) did conduct a statistical study of auroral energies associated with substorm onset. They made distinctions between broadband (Alfvén accelerated) electrons, monoenergetic (parallel electric field accelerated) electrons, and diffuse (whistler mode wave scattered) electrons. They found that total energy flux increases in association to substorm onset for all types, with the largest for diffuse electrons. However, they made no distinction between diffuse and pulsating aurora.

These previous investigations make a strong case for a link between substorm onset and AE index and both the total energy flux and spectral hardness of pulsating aurora. More energetic events seem to occur right after substorm onset and for higher AE indices. However, direct evidence supporting this hypothesis has yet to be established. Providing this evidence will be an important step in understanding how energy is transferred from the magnetosphere to the atmosphere. There are many reasons why this is important, but one which has recently become more apparent is the depletion of ozone due to pulsating aurora produced NO_x and HO_x (Turunen, Kero, Verronen, et al., 2016; Verronen, Kero, Partamies, et al., 2021). In this paper, we provide statistical evidence, using inverted energy content, that substorm onset and AE index are correlated with both a larger and harder differential energy flux during pulsating aurora. The results shown here both confirm the high-energy nature of pulsating aurora and specify how pulsating aurora energies are correlated with substorm onset and AE index.

2.2 Data

This chapter presents a data set of 57 pulsating aurora events between 2012 and 2021, four of which (2015-01-13, 2017-08-17, 2018-12-30, and 2021-01-13) were not usable for our energy inversion. We visually identified pulsating aurora using all sky images and used the classifications of both Royrvik and Davis (1977) and Grono and Donovan (2018) when doing so. This data was captured over 51 days with the Poker Flat Research Range All Sky Imager (PFRR ASI) and can be found in R. Troyer, Jaynes, Jones, et al. (2022). The PFRR ASI takes an image approximately every 12 seconds at 428 nm, 557 nm, and 630 nm. We used the 428 nm images. It is worth noting that despite the 12 second period of the camera, we can still accurately identify pulsating aurora, see Figure 11 panels A1-A3 as an example.

For each of these pulsating aurora events, the Poker Flat Incoherent Scatter Radar (PFISR) was running one of the D-region modes (MSWinds23, MSWinds26, or MSWinds27). For more details about these modes, see Kaeppler, Sanchez, Varney, et al. (2020). These modes all use 13-baud Barker codes with $10 \mu\text{s}$ baud, oversampled at $5 \mu\text{s}$ (0.75 km range resolution) to provide

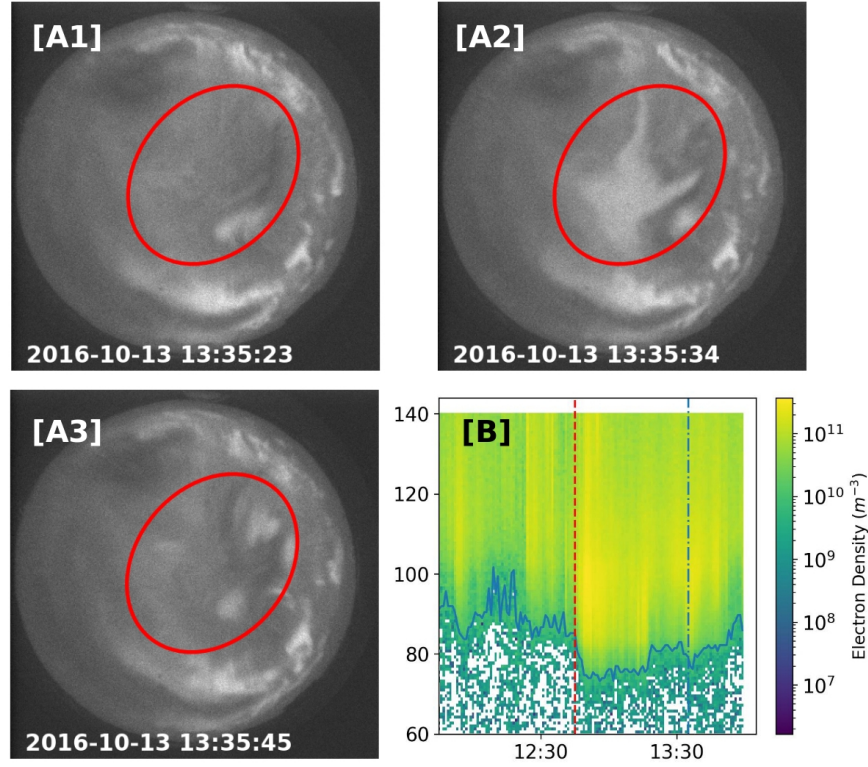


Figure 11. Panels A1-A3 show a series of 428 nm images from the Poker Flat Research Range All Sky Imager with several pulsating aurora patches of differing sizes. Even though the imaging cadence of 12 seconds is longer than some pulsating periods, we can still identify pulsating aurora. The red dot indicates the center of each image and thus the approximate location of the vertical PFISR beam. Panel B is the PFISR electron number density data for a pulsating aurora event on October 13, 2016. The data is plotted vs. altitude in km and universal time. The dashed red line indicates the start of pulsating aurora. The dashed and dotted blue line indicates when the images were taken. The radar stopped taking data before the pulsating aurora ended. The solid blue line indicates the lowest altitude where $N_e = 10^{10} \text{ m}^{-3}$.

electron density as function of range and time over ranges between 40 to 144 km. This study uses one minute integration times, which means the electron density profiles are averaged over many cycles of the pulsating aurora. These modes all use four beam directions (magnetic zenith, vertical, north-west, and north-east). This study uses the vertical beam data since it is systematically more sensitive than the magnetic zenith direction at PFISR. The magnetic zenith is close to the phased-array antenna grating lobe steering limit. Furthermore, the MSWinds27 modes revisit the beams unevenly such that the vertical beam receives 16 times more pulses than the other beam directions, resulting in a factor of 4 improvement in the statistical uncertainty relative to the other beam directions. The vertical beam is $< 20^\circ$ away from the magnetic zenith direction which is sufficiently small for our inversions to neglect any variations across magnetic field lines. The result of using the 1-minute integrated vertical beam is a data set of approximately 3800 electron density profiles split over the 57 pulsating aurora events. Chapter 5.1.1 gives additional information on the PFISR experiments and data processing. Figure 11 panel B shows an example of electron densities measured by PFISR MSWinds23 during a period of typical pulsating aurora on October 13, 2016. This event began less than 15 minutes after a substorm onset and continued until the end of the PFISR experiment.

2.3 Analysis

In this chapter, we quantify the differential energy flux of pulsating aurora, in particular, the higher energy portion. Previous investigations have indicated that the energy of pulsating aurora varies significantly both within and between events, and is correlated with substorm activity (Jones, Lessard, Fernandes, et al., 2009; Wing, Gkioulidou, Johnson, et al., 2013; Hosokawa & Ogawa, 2015). Based on these results, we chose to examine variations related to magnetic local time (MLT), AE index, and an epoch associated with substorm onset temporal proximity. We set an epoch time of 0 to substorm onsets taken from lists created by Newell and Gjerloev (2011b), Forsyth, Rae, Coxon, et al. (2015), and Ohtani and Gjerloev (2020). We chose these three lists because they cover a time period that covers the range of dates in our data. Each method identifies

substorms in a slightly different way, so by including all three we can identify more events over a broader range of criteria. To make sure that one method isn't biasing the results, we repeated our analysis using each individual list and found that they all had similar behaviors. If a substorm onset is repeated in more than one list, we use the onset closest to the pulsating aurora event. We limited these substorms to those that occurred within $\pm 15^\circ$ longitude and $\pm 8^\circ$ latitude of the Poker Flat Research Range. The substorm onset lists may not be as precise as a skilled observer, but due to the statistical nature of this study we were unable to classify by hand. However, we believe any associated error will be smaller than the 20 minute time bins that we use. For the AE indices, we used archived 10-minute averaged predicted values (Luo, Li, Temerin, & Liu, 2013). For every 1-minute electron density profile we find the closest in time AE index and assign that to the data point.

As a proxy for energy, we chose the lower altitude boundary that PFISR measured a number density of $N_e = 10^{10} \text{ m}^{-3}$ for each 1-minute integrated altitude profile. Additionally, to meet this criteria, the associated error had to be less than $5 \times 10^9 \text{ m}^{-3}$. We chose these values somewhat arbitrarily given that they are round numbers near the detection limit of PFISR. However, we did test the sensitivity by varying the threshold up to an order of magnitude higher and rerunning the analysis. When doing this, we found that the behavior did not change. Future, more sensitive instruments could use a smaller density threshold and thus detect lower altitudes. Finally, we implemented an outlier-rejection algorithm to remove high power returns that are not consistent with the expected electron density profile from precipitation. The D-region data can be cluttered by range-aliased satellite echoes, airplanes in antenna sidelobes, and various types of interference. Most of these clutter sources appear as localized outliers in the power data confined to one or two range-gates. We expect a realistic electron density profile to extend over 10s of km in altitude and be monotonically decreasing with altitude. We compute the median electron density over 5 km around a data point and check that it is less than the median electron density 20 km above that point. Furthermore, we check that there are not any NaN or negative electron density estimates in the 20 km above that point. If any of these checks fails, we continue the search at a higher altitude.

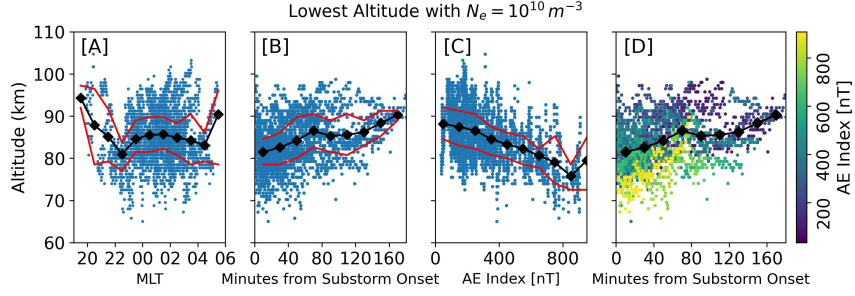


Figure 12. Lowest altitude PFISR measurements during pulsating aurora with $N_e = 10^{10} \text{ m}^{-3}$ plotted versus magnetic local time [A], time from the nearest substorm onset [B], AE index [C], and combined substorm and AE [D]. The black diamonds indicate the average altitude for the surrounding hour, 20 minutes, 200 nT of AE, and 20 minutes respectively. The red lines indicate the 25% and 75% quartiles.

For context, we have also included plots using the altitude of the peak electron density. These are shown in Figure 13. Overall, the trend are similar but less pronounced than in Figure 12, with the exception of magnetic local time.

2.3.1 Magnetic Local Time

Figure 12 panel A shows the altitude boundary values compared to MLT as calculated from the IGRF model for 2020. As we would expect, a majority of the measurements during pulsating aurora occurred several hours after magnetic midnight. Previous studies have shown that this is the most common time for pulsating aurora (Oguti, Kokubun, Hayashi, et al., 1981; Jones, Lessard, Rychert, et al., 2011). The hourly averages shown by the black diamonds centered on each hour indicate that there is little, if any, dependence on MLT. The peak electron density shows a stronger MLT dependence as illustrated in Figure 13. This is in agreement with previous studies of peak electron density altitude and MLT (Hosokawa & Ogawa, 2015; Partamies, Whiter, Kadokura, et al., 2017; E. C. Bland, Partamies, Heino, et al., 2019; Tesema, Partamies, Nesse Tyssøy, & McKay, 2020; Nanjo, Hozumi, Hosokawa, et al., 2021). This indicates that the more energetic electrons depend less on MLT and more on substorm activity, while the opposite is true of the lower energy electrons. However, it's also possible that our data is not an accurate representation in relation to

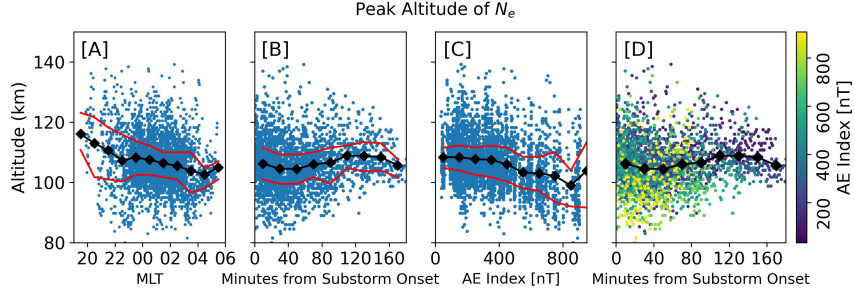


Figure 13. Altitude of the peak electron density in PFISR measurements during pulsating aurora plotted versus magnetic local time [A], time from the nearest substorm onset [B], AE index [C], and combined substorm and AE [D]. The black diamonds indicate the average altitude for the surrounding hour, 20 minutes, 200 nT of AE, and 20 minutes respectively. The red lines indicate the 25% and 75% quartiles.

MLT due to the wide scatter and limited statistics for several time bins. In addition, we requested instrument runs during the most common time for pulsating aurora, so the data is biased towards that period. It would be interesting to investigate this disparity in future studies.

2.3.2 Substorm Onset And Ae Index

Figure 12 panel B shows the altitude boundary with $N_e = 10^{10} \text{ m}^{-3}$ compared to substorm onset. Here we see that lower altitudes are more common closer to substorm onset, indicating a hardening of the energy content. These results are similar to that of Oyama, Kero, Rodger, et al. (2017), who found both an enhancement and lowering of electron densities just after substorm onsets for several case study pulsating aurora events. Our work extends these findings to a statistical dataset.

Figure 12 panel C shows the altitude boundary with $N_e = 10^{10} \text{ m}^{-3}$ compared to the closest in time 10-minute averaged AE index. Similar to substorm onset temporal proximity, there is a clear relation between a higher AE value and lower altitudes. This is similar to the results of Hosokawa and Ogawa (2015) who found that the peak altitude of pulsating aurora lowers during higher AE indices. However, our measurements differ in that the peak altitude is a proxy for an average energy flux, whereas our lower altitude boundary is more representative of the energy

content hardness.

We combined Figures 12B and 12C to produce Figure 12 panel D. Here we have colored the markers of Figure 12B based on AE index. This result shows that both substorm onset temporal proximity and AE index play a role in varying the lower altitude boundary. The lowest altitudes tend to occur with both a high AE index and close temporal proximity to a substorm. In regards to the statistics, our events cover a wide range of AE indices with 10 occurring during periods with $AE > 600$ nT and of those 3 with $AE > 800$ nT.

In Figure 14 we repeated the above analysis with the AL index and obtained similar results. A more negative AL index corresponded to lower altitudes.

It is more typical for studies to concentrate on the altitude of the peak electron density (Oyama, Kero, Rodger, et al., 2017; Hosokawa & Ogawa, 2015; Jones, Lessard, Fernandes, et al., 2009). We chose a different metric as we wanted a proxy that would more closely represent the flux of higher energy particles. This approach isn't perfect as a higher flux of slightly lower energy particles could produce a similar boundary to a lower flux of higher energy particles. While systematic changes in the background density dependent on time of day, season, etc. could bias these results, we believe that because the background density is usually below the detection limit of PFISR, this effect will be small enough that it won't have a meaningful impact (Kaeppeler, Sanchez, Varney, et al., 2020). Any altitude metric is still only a proxy for energy, but this one also contains other useful information. One of the main goals of this work is to provide data to help understand the atmospheric effects of pulsating aurora such as ozone depletion. In this regard, atmospheric changes are more important than the original energy flux. For instance, studies of energetic particle precipitation indicate that an energy flux deposited at 100 km may have less of an impact on ozone production than an energy flux deposited at 80 km (Verronen, Kero, Partamies, et al., 2021). Thus, by choosing to measure altitude from a lower boundary instead of the peak electron density, we are able to more closely connect our measurements to possible atmospheric effects. Finally, due to the limitations of a proxy such as this, the reader should view Figure 12 as additional contextual information. For explicit values, we performed inversions of the full electron density profile to

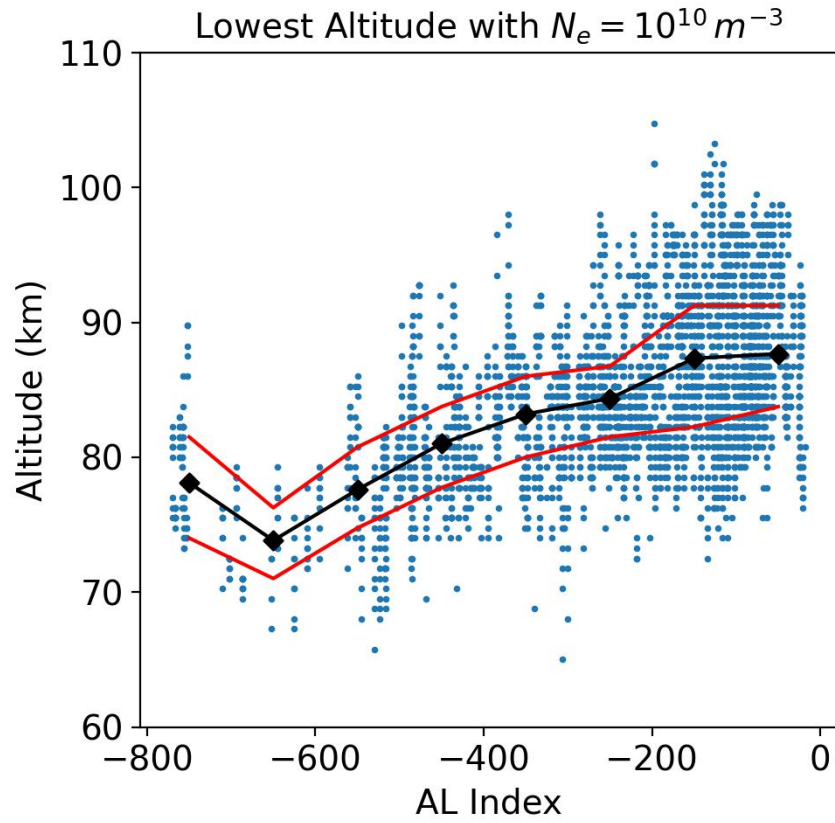


Figure 14. Lowest altitude PFISR measurements during pulsating aurora with $N_e = 10^{10} \text{ m}^{-3}$ plotted versus AL indices. The black diamonds indicate the average altitude for the surrounding hour, 20 minutes, 200 AE units respectively. The red lines indicate the 25% and 75% quartiles.

estimate the incoming differential energy flux. See Section 2.3.3 for these results.

2.3.3 Energy Spectra From Electron Density Inversion

Our analysis of the lower altitude boundary with $N_e = 10^{10} \text{ m}^{-3}$ indicates that both AE index and substorm onset have substantial impacts on how hard the pulsating aurora energy content can be. However, this metric is only a proxy for hardness. To investigate further, we solved the inverse problem required to convert the PFISR electron densities into a differential energy flux. To do this, we used the process outlined in Semeter and Kamalabadi (2005). We assumed that the pitch angle distribution was isotropic (Whalen, Miller, & McDiarmid, 1971; Sandahl, Eliasson, & Lundin, 1980). We also assumed that the 1-minute PFISR integrated electron density varied slowly. While Hosokawa and Ogawa (2015) showed that the electron density can vary between the on and off phases of pulsating aurora, these changes occur at a sub-minute frequency and so will be smoothed over in the PFISR integration. However, if these assumptions are not valid it could change our results. We describe our exact implementation of the inversion process in Chapter 5.1. In an inverse problem such as this, there are multiple spectra that could result in a reasonably good fit of the density profile, making the problem ill-defined. To pick the best fit, we chose the solution that maximized the Berg Entropy. As Semeter and Kamalabadi (2005) states, this solution “may be viewed as the most noncommittal approach with respect to the unavailable information.” Because of these uncertainties that are inherent to the inversion process, it is not useful to look at the finer shape of the differential energy flux. Instead, to provide a more robust analysis, we chose an energy threshold of 30 keV to separate the low and high portions of the differential energy flux and integrated the two regions. This gives us an average low and high energy flux and limits the dependence of our results on the smaller scale details.

The largest source of error in the inversion process is likely the assumed atmospheric chemistry that connects PFISR observations to an ionization rate via a recombination coefficient. This is still an ongoing area of research, especially for the D-region. As our primary chemistry model, we used the Glukhov-Pasko-Inan (GPI) model (Glukhov, Pasko, & Inan, 1992; Lehtinen

& Inan, 2007). This has been shown to perform well for the D-region (Marshall, Xu, Kero, et al., 2019). For the E-region, we set the coefficient values above 90 km to those calculated by Gledhill (1986) for nighttime aurora. The Gledhill model is suitably close to that of Vickrey, Vondrak, and Matthews (1982) above 90 km and the Vickrey model performs well in this region (Sivadas, Semeter, Nishimura, & Kero, 2017). While we could have used the Vickrey model, we believe the Gledhill model is more relevant for this data as it was derived for nighttime auroral activity. However, both models are only rough estimates of the recombination coefficient. We refer to this adjusted model as GPI+. To provide context to our results calculated using GPI+, we inverted each density profile using three additional chemistry models. These results can be found in Chapter 5.1.

After performing the inversions, we found the geometric mean of the differential energy flux for ≥ 30 keV and < 30 keV electrons in bins relative to substorm onset and AE index. Figure 15 demonstrates the link between energy and substorm activity. It shows how the energy composition of pulsating aurora varies with respect to both substorm onset temporal proximity [A] and AE index [B]. Within an hour of a substorm around a third of the total differential energy flux is carried by ≥ 30 keV electrons. At > 60 minutes this drops to around a sixth. While the total differential energy flux is higher closer to a substorm onset, the relative energy composition does not change until an hour after onset. This indicates that the initial substorm “kick” hardens the energy content and it remains hard up to an hour afterwards, even as the total differential energy flux decreases. Some of this behavior could be related to a mixing of expansion and recovery substorm phases in the 20-40 minute and 40-60 minute bins. However, due to limitations in our data, we were unable to classify based on substorm phase.

The differential energy flux associated with AE index varies even more dramatically. In highly perturbed times of $AE > 600$ nT over a half of the average differential energy flux is carried by the ≥ 30 keV electrons. This again drops to just over a tenth for quiet periods of $AE \leq 200$ nT. We also looked at the differential energy flux relative to AL indices, but found no difference to AE beyond a few percent.

Assumptions about the atmospheric chemistry can vary the absolute differential energy flux,

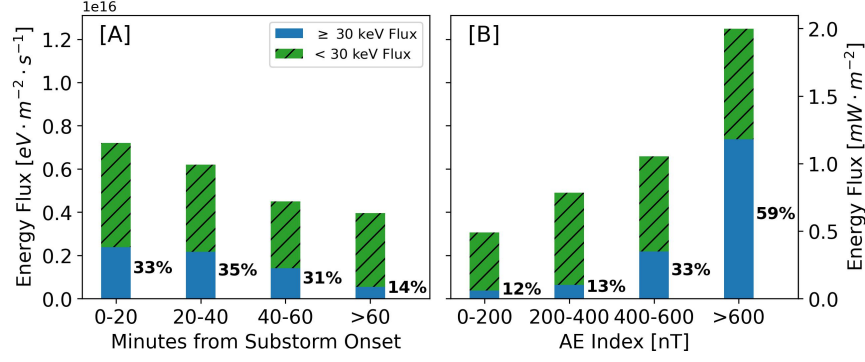


Figure 15. The high ($\geq 30 \text{ keV}$) and low ($< 30 \text{ keV}$) differential energy flux contributions to pulsating aurora events occurring in four temporal bins relative to substorm onset [A] and AE index [B].

but for every model we found the same relative behavior. While not shown here, the relative behavior was also the same when we used threshold values of 50 keV and 100 keV. For $< 20 \text{ min}$ the high energy contributions were 13.9% and 1.2% respectively. For $\text{AE} > 600 \text{ nT}$ these were 37.8% and 2.4% respectively. Thus, we conclude that pulsating auroral energy content is varied by both the strength of a substorm as well as temporal proximity to it.

2.4 Discussion

Our work builds on Wing, Gkioulidou, Johnson, et al. (2013), Hosokawa and Ogawa (2015), and Oyama, Kero, Rodger, et al. (2017), whose studies showed that the altitude of pulsating aurora can decrease after substorm onset and for periods of high AE index. It also builds on papers such as Jones, Lessard, Fernandes, et al. (2009), which demonstrated that the inverted differential energy flux of particular pulsating aurora events can vary throughout the event. These studies suggest that the total energy flux and spectral hardness of pulsating aurora could be influenced by substorm onset and AE index, but does not make a direct statistical connection.

Figure 15 demonstrates, statistically, that the total differential energy flux of pulsating aurora is highly variable. Second, they show that pulsating aurora events can have large, and in some cases majority, contributions from $\geq 30 \text{ keV}$ electrons, which represents a hard energy content relative to other auroral types. Third, it shows that these quantities are strongly correlated with

substorm onset and AE index. These statistical links have never been demonstrated before with inverted differential energy flux and they suggest a process connecting substorms and pulsating aurora.

The link between substorms and pulsating aurora is likely through whistler-mode waves, which are known to drive instances of pulsating aurora (Nishimura, Bortnik, Li, et al., 2010; Nishimura, Bortnik, Li, et al., 2011; A. N. Jaynes, Lessard, Rodriguez, et al., 2013; Kasahara, Miyoshi, Yokota, et al., 2018; Hosokawa, Miyoshi, Ozaki, et al., 2020). There is a well documented relation between substorm activity post-midnight and whistler-mode wave generation near the equator (Tsurutani & Smith, 1974; Thorne, Smith, Fiske, & Church, 1974). The proposed mechanism connecting them is Doppler-shifted cyclotron resonance with 10-100 keV substorm injected electrons (Dungey, 1963; Kennel & Petschek, 1966). In addition, the amplitude of already present whistler-mode waves can vary with substorm injection. Meredith, Horne, Johnstone, and Anderson (2000) showed that between $3.8 < L < 6$ whistler-mode amplitudes increased after a substorm and then decayed with a timescale of $\tau \approx 1.1$ hours. Given that whistler-mode waves are known to drive pulsating aurora, could this be one likely explanation? We investigate this connection more in Chapter 3.

Also, Figure 15 confirms the inherent energetic nature of pulsating aurora that previous case studies have suggested. Understanding the nature of pulsating aurora is important when assessing their atmospheric impact. Pulsating aurora are very common (Oguti, Kokubun, Hayashi, et al., 1981) and can be long-lasting (Jones, Lessard, Rychert, et al., 2013), thus they could represent an important transfer of energy between the magnetosphere and lower ionosphere. To assess the subsequent impact, both the total energy flux and the hardness of the spectra are of high relevance. Higher energy electrons reach further into the atmosphere and thus have a higher probability of influencing terrestrial climate through processes like NO_x and HO_x based ozone depletion (Turunen, Kero, Verronen, et al., 2016; Verronen, Kero, Partamies, et al., 2021, & and references therein). We found that the hardest events occur close in time to substorm onset and for high AE indices. In short, our results can be used to more accurately parameterize the atmospheric consequences of

pulsating aurora. For instance, combining the results of Figure 15 with those of E. Bland, Tesema, and Partamies (2021), we can perform a back-of-the-envelope calculation to estimate the incoming power of a typical pulsating aurora event. We will assume an event extending between 62° and 70° magnetic latitude and 4 hours of magnetic local time. Using this, approximately 4.8 gigawatts (GW) of power would be entering the atmosphere during periods with $AE > 600$ nT with 2.8 GW coming from ≥ 30 keV electrons. For periods < 20 minutes after substorm onset and all AE indices these values are 2.5 GW and 0.8 GW respectively.

In Figure 12B it appears that within 20 minutes of substorm onset, what could be considered the expansion phase, is the most common time for our pulsating aurora. That statistic seems to be in contradiction to Partamies, Whiter, Kadokura, et al. (2017), who found that the most common substorm phase for pulsating aurora was the recovery phase. While occurrence rates were not the focus of this work, it is worth examining where this difference could come from. There are two potential reasons. One, our search for pulsating aurora differs. Partamies, Whiter, Kadokura, et al. (2017) only identified pulsating aurora when it was the most dominant type, stating that "...our event selection criteria favors recovery phases over the expansion phases where brighter aurora plays a major role in the auroral displays." Our search included pulsating aurora when it was the most visually dominant type of aurora directly overhead, but not necessarily across the entire field of view. Two, Partamies, Whiter, Kadokura, et al. (2017) used a magnetometer at the imager locations while our search was semi local and encompassed a much larger geographic region, so our ratio of substorms to pulsating aurora events was likely higher.

It is worth describing possible sources of systematic error in our results. One, several previous studies found that the energy content becomes harder during the on phase of pulsating aurora (Hosokawa & Ogawa, 2015; Whalen, Miller, & McDiarmid, 1971). Our data is integrated over one minute, so these variations will likely be smoothed out, thus reducing the hardness. Two, we are not capturing the full range of the energy flux. Ionization associated with electron energies less than about 1 keV usually peaks above the altitudes that PFISR measures in the D-region mode (Fang, Randall, Lummerzheim, et al., 2010). If the energy flux for this portion of the spectrum is

significant, we could be overestimating the hardness and underestimating the total energy. Three, the sensitivity of PFISR limits our ability to detect higher energy, lower flux electrons. If populations such as these are present, we could be underestimating the hardness. Four, we only selected pulsating aurora that were in the center of the imager, but we didn't account for times that the PFISR beam wasn't directly on a pulsating patch. If the precipitating flux is highly local, we could be underestimating the energy flux during such periods.

The statistical spread of energies in most of our bins is greater than an order of magnitude. This is an indication of how variable pulsating aurora energies can be, but also suggests other variables are involved than just the ones we looked at. One possibility is the type of pulsating aurora. As Tesema, Partamies, Nesse Tyssøy, and McKay (2020) found, the electron density profile, and thus likely the energy, varies between the types identified by Grono and Donovan (2018). Given the image cadence of our data, we could not accurately distinguish between the different types. Another possibility is substorm phase. Due to the nature of our substorm onset lists, it was not feasible for us to classify based on substorm phase. However, the length of the expansion and recovery phase of different substorms can vary (Chu, McPherron, Hsu, & Angelopoulos, 2015). Given that our metric was based only on time from substorm onset, it's likely that some of our bins include events from multiple different phases. If there is a difference in energy content between the expansion and recovery phase, this would be another unaccounted for variable. Future studies that include pulsating aurora type and substorm phase might see an even stronger correlation.

2.5 Summary

It has been suspected that substorm onset and AE index are linked to variations in the energy flux of incoming electrons responsible for pulsating aurora. Studies investigating proxies for energy, such as the altitude of the peak electron density are the basis of this hypothesis. In this chapter, we presented statistical evidence, using inverted energy content, which supports this hypothesis. Pulsating aurora that occur right after substorm onset and/or are associated with high AE values are more likely to have a higher energy flux, and a harder energy spectrum.

- The differential energy flux of pulsating aurora correlates strongly with the substorm onset and AE index.
- In relation to substorm onset the total differential energy flux varies between 1.15 and $0.63 \text{ mW} \cdot \text{m}^{-2}$ for ≤ 20 and > 60 minutes. The associated contribution to the total differential energy flux from ≥ 30 keV electrons are 33% and 14%.
- In relation to substorms, the differential energy flux remains hard out to 1 hour after onset before softening.
- In relation to AE index the total differential energy flux varies between 2.00 and $0.49 \text{ mW} \cdot \text{m}^{-2}$ for $\text{AE} > 600$ nT and ≤ 200 nT. The associated contributions to the total differential energy flux from ≥ 30 keV electrons are 59% and 12%.
- We estimate that for a typically pulsating auroral event occurring < 20 min after substorm onset ($\text{AE} > 600$ nT), approximately 2.5 (4.8) GW of power enters the atmosphere over 8° magnetic latitude and 4 hours of MLT. The contributions from ≥ 30 keV electrons are 0.8 (2.8) GW.

2.6 The Lamp Rocket Mission

We used the results of this chapter to help successfully launch the Loss Through Auroral Microburst Pulsations (LAMP) rocket mission. Originally scheduled to launch in 2019, but then delayed due to a government shutdown and COVID-19, the rocket blasted off into pulsating aurora on March 5, 2022. The rocket's mission was to better understand the connection between microbursts and pulsating aurora. Microbursts are typically classified into two types.

Auroral microbursts are burst of precipitating electrons with energies < 100 keV that were originally measured in bremsstrahlung x-ray emissions. These bursts have a width-at-half-maximum of around 0.25 seconds and can occur singularly or in trains of on average 5 (Anderson & Milton, 1964).

Relativistic microbursts are usually considered separate from auroral microbursts and appear as bursts in electron fluxes in the outer radiation belt. The energy of these electrons is > 1 MeV and are thought to be a major contributor to relativistic electron loss in the radiation belt (Lorentzen, Looper, & Blake, 2001).

As Hosokawa, Miyoshi, Ozaki, et al. (2020) and Miyoshi, Hosokawa, Kurita, et al. (2021) showed, the sub-second rising/falling tones often observed during periods of chorus could cause both auroral microbursts and the 3 Hz modulation of pulsating aurora patches. LAMP combined electron instrumentation aboard the rocket with high speed auroral cameras at three ground locations (Poker Flat Research Range, Venetie, Fort Yukon) to observe this connection during a period of pulsating aurora.

Another aspect of the LAMP mission is to better understand the relationship of MeV electrons to pulsating aurora. There is some evidence to suggest that MeV electrons may be present during pulsating aurora, however as we showed in Section 1.7.4, the resonant energies of lower-band chorus are well below the MeV range (Miyoshi, Hosokawa, Kurita, et al., 2021). While this is true at the equator, Miyoshi, Saito, Kurita, et al. (2020) showed that at higher latitudes it is possible to resonant with these higher energy electrons. By including electron instrumentation designed to measure energies from a few eV to 2 MeV, LAMP was equipped to answer this question. We used the results in this chapter to time the rocket launch in coordination with a substorm onset.

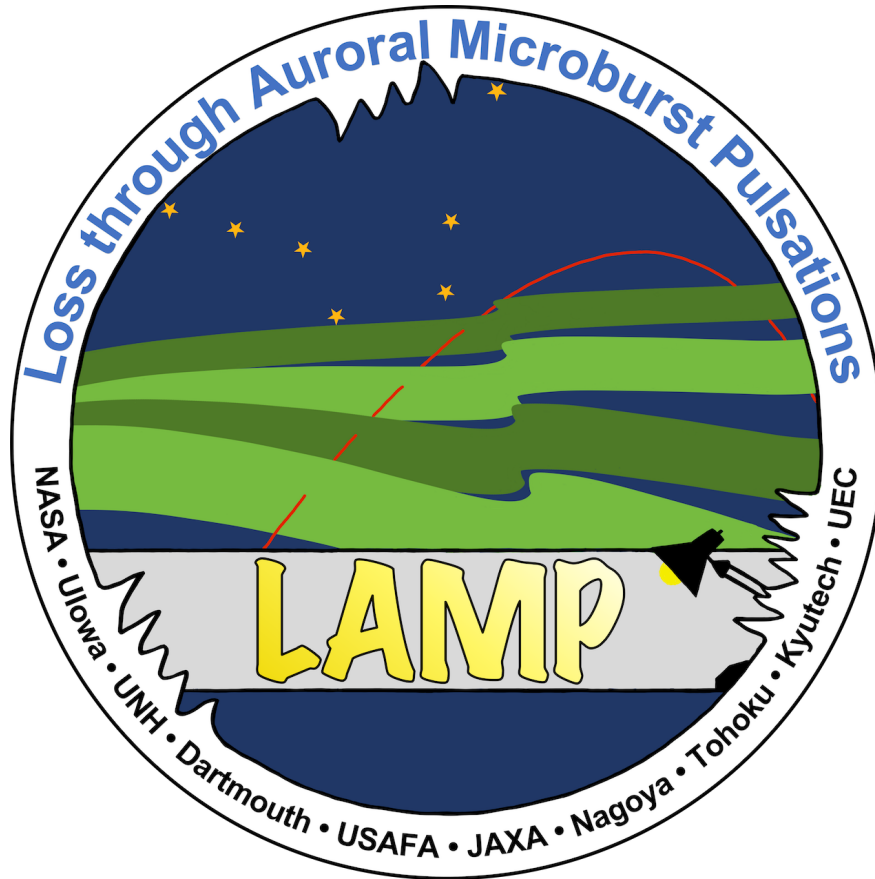


Figure 16. Loss Through Auroral Microburst Pulsations (LAMP) rocket mission logo. As the logo designer, I had to shamelessly include this in my thesis. There are several hidden gems in the logo. The blue background and big dipper star constellation are the colors and constellation of the Alaska State flag. This represents the rocket launching from Alaska. The modulating light and dark auroral arcs represent pulsating aurora. The microburst wiggles that break up the inner boarder are pulled directly from the original microburst paper (Anderson & Milton, 1964). There are three of these trains to represent the 3 Hz flicker of pulsating aurora. Finally, the lamp (besides the obvious) represents the mission phrase "shinning a light on pulsating aurora".

CHAPTER 3: THE SOURCE MECHANISM OF PULSATING AURORA

3.1 Background

The outer Van Allen radiation belt is a region of space surrounding Earth, usually between $3 < L < 7$, that is filled with energetic ions and electrons (Baker, Kanekal, Hoxie, et al., 2013). These particles are trapped in the magnetic mirror created by the planet's approximate dipole magnetic field. During periods of low magnetic activity, particles are generally stable and $\vec{E} \times \vec{B}$, gradient, and curvature drift around the planet (Roederer, 1970). However, there are several processes that can perturb these populations, causing them to precipitate into the atmosphere. In this chapter, we focus on the interaction between the energetic electrons and electromagnetic chorus waves. This interaction can precipitate energetic electrons into the atmosphere. Energetic electron precipitation (EEP) is an important dynamic to the magnetosphere-ionosphere-thermosphere coupled system (Lam, Horne, Meredith, et al., 2010). It represents a significant transfer of energy from magnetosphere to upper atmosphere and can result in ozone depletion (Verronen, Kero, Partamies, et al., 2021; Turunen, Kero, Verronen, et al., 2016). Pulsating aurora is a visual manifestation of the precipitating electrons and can be an excellent way to study EEP (E. Bland, Tesema, & Partamies, 2021). There are still many unknowns in the process that produces EEP and pulsating aurora (Lessard, 2013; Partamies, Tesema, & Bland, 2022). In this chapter, we provide additional statistical evidence for substorm driven lower-band chorus waves as a source of energetic pulsating aurora. We do this by measuring chorus decay e-folding timescales after substorms and comparing them to known pulsating aurora timescales.

Chorus waves are an important feature of the outer Van Allen radiation belt and drive many of this regions dynamics (Meredith, Horne, Shen, et al., 2020; Hua, Bortnik, Kellerman, et al., 2023; Hua, Bortnik, Spence, & Reeves, 2023). They are characterized by frequency, which typically ranges between the electron cyclotron frequency (f_{ce}) and one tenth of f_{ce} . There is a clear gap at one half f_{ce} , due to Landau damping, such that lower-band chorus waves (LBC) occur between $0.1 f_{ce}$ and $0.5 f_{ce}$ while upper-band chorus waves (UBC) occur between $0.5 f_{ce}$ and f_{ce}

(Bortnik, Inan, & Bell, 2006). In some cases low-frequency chorus can extend to $0.05 f_{ce}$ or lower at magnetic latitudes greater than 20° (Meredith, Horne, Li, et al., 2014). For our analysis we only looked at data with magnetic latitude less than 20° and so did not consider this low-frequency chorus. Chorus waves are named for their resemblance to the sound of birds chirping caused by sub-second rising and falling tones in their frequency distributions (Isted & Millington, 1957; Tsurutani & Smith, 1974). In addition to the sub-second timescales, chorus waves can also be modulated on the order of seconds (A. N. Jaynes, Lessard, Takahashi, et al., 2015). Studies have directly linked modulations over seconds in the chorus power spectral density (SD) and electron flux in the chorus region to instance of pulsating aurora, where an intensification corresponds to the brightening of an auroral patch (Nishimura, Bortnik, Li, et al., 2011; A. N. Jaynes, Lessard, Rodriguez, et al., 2013; Kasahara, Miyoshi, Yokota, et al., 2018). Due to the difficulty in connecting chorus activity to ground observations, these studies have only been able to analyze a handful of events.

As we discussed in Chapter 2, pulsating aurora are a common subset of diffuse-like aurora. They appear as an uncoordinated symphony of dim auroral patches that blink on and off across wide portions of the sky. The period of this blinking can range up to around 20 seconds. Individual patches can be remarkably varied with differing periods, shapes, and sizes typically between 10s to 100s of kilometers (Johnstone, 1978; Lessard, 2013). Pulsating aurora often develop near the end of a substorm display and can continue for hours after (Jones, Lessard, Rychert, et al., 2011). There also is a relation between greater energy flux and closer temporal proximity to the substorm (Hosokawa & Ogawa, 2015; Oyama, Kero, Rodger, et al., 2017; R. N. Troyer, Jaynes, Kaeppler, et al., 2022). Substorms are characterized by a rapid dipolarization of Earth's nightside magnetic field that accelerates and injects electrons into the inner magnetosphere (Akasofu, 1966). Some of these electrons accelerate directly into the atmosphere, causing discrete and substorms aurora (Korth, Zhang, Anderson, et al., 2014; Schroeder, Howes, Kletzing, et al., 2021). Others are injected into the radiation belts and can drive wave activity (Tsurutani & Smith, 1974; Chepuri, Jaynes, Turner, et al., 2023). Ground-based magnetometers can detect substorms as an enhancement of the auroral

electrojet and report this in the AE index.

While a correlation does exist between LBC waves and pulsating aurora for certain events, it is still an open question as to how statistically important this relationship is (Lessard, 2013; Borovsky & Partamies, 2022). That being said, there are known, indirect, statistical links between the two. For instance, both LBC and pulsating aurora occur most frequently and with the strongest intensity between 3 and 6 MLT (Oguti, Kokubun, Hayashi, et al., 1981; Jones, Lessard, Rychert, et al., 2011; Meredith, Horne, Shen, et al., 2020). Additionally, pulsating aurora frequently have significant energy contributions from 10s to 100s of keV electrons, which, as we showed in Chapter 1.7.4, is the resonant energy range for lower-band chorus (Tesema, Partamies, Tyssøy, et al., 2020; R. N. Troyer, Jaynes, Kaeppler, et al., 2022). In this chapter we add to that evidence by showing that lower-band chorus and pulsating aurora have similar decay timescales after substorms.

A proposed process for this interaction is Doppler shifted cyclotron resonance between 10s of keV electrons and lower-band chorus, which can simultaneously drive wave growth and pitch angle scatter electrons (Brice, 1964; Trakhtengerts, Demekhov, Titova, et al., 2004; Miyoshi, Saito, Kurita, et al., 2020). Therefore, assuming pitch angle scattered electrons are responsible for pulsating aurora, a timescale in the aurora should correspond to a timescale in the waves. In Chapter 2 we found such a timescale for ≥ 30 keV electrons associated with pulsating aurora. We saw that the differential energy flux from these electrons decayed after substorms with an e-folding time of just under an hour, suggesting that substorms are a primary driver of pulsating aurora EEP. Complementing this, Meredith, Horne, Johnstone, and Anderson (2000) found a similar timescale when looking at post-substorm decay of chorus electric field amplitudes from the CRRES spacecraft. We hypothesize that energetic electrons injected into the outer radiation belt during substorms drive chorus waves, and that pitch angle scattering from this interaction causes pulsating aurora. We provide evidence towards that hypothesis by expanding on Meredith, Horne, Johnstone, and Anderson (2000) using the more recent and expansive Van Allen Probes dataset. In doing so, we confirmed that lower-band chorus waves decay after substorms with a similar timescale to pulsating aurora. We also discovered that this decay time depends on magnetic local time (MLT), magnetic latitude

(MLAT), and wave frequency. Our quantified decay timescales add statistical evidence linking chorus waves, substorms, and pulsating aurora.

3.2 Data

3.2.1 Electric And Magnetic Fields

Our primary dataset is from the Electric and Magnetic Field Instrument Suite and Integrated Science (EMFISIS) instruments aboard the Van Allen Probes. The Van Allen Probes were two identical spacecraft that orbited through the planet's outer radiation belt between 2012 and 2019 (Mauk, N. J. Fox, Fox, et al., 2013). EMFISIS uses a tri-axial fluxgate magnetometer (MAG) and a tri-axial search coil magnetometer (MSC) to measure DC and wave magnetic fields respectively (Kletzing, Kurth, Acuna, et al., 2013). EMFISIS also takes an analog electric field signal from the Electric Fields and Waves (EFW) experiment to measure the wave electric field (Wygant, Bonnell, Goetz, et al., 2013). The collective wave electric and magnetic field measurements are called the Waves experiment and cover the frequency range from 10 Hz up to 12 kHz. In survey mode, the Waves experiment provides a 6-second power spectral density (SD) for both the electric and magnetic fields in three orthogonal directions. We used the total electric/magnetic SD, which is a sum of all three components.

A property of the double probe electric field sensors on the Van Allen Probes is that they become electrically coupled to the local plasma. To account for this, we use the sheath corrected electric field measurements that provide an adjustment based on local electron density (Hartley, Christopher, Kletzing, et al., 2022). In addition, the electric field measurements contain noisy frequency bands at 1781 Hz and 3555 Hz, so we omitted this data for our analysis. We are more confident in the magnetic field measurements and used these for most of our findings.

3.2.2 Post-substorm Identification

To detect substorm activity we used the SuperMAG collaboration's 1-minute SME index (Gjerloev, 2012). This index is designed to replicate the AE index using at least 100 of the Super-

MAG magnetometers. Similar to AE, SME is measured in nT with larger positive values corresponding to a stronger auroral electrojet (Newell & Gjerloev, 2011a).

The AE index, and thus SME, correlates well with particle injections in the inner magnetosphere (Meredith, Horne, Johnstone, & Anderson, 2000). These injections are linked with substorms and reconnection in the magnetotail (DeForest & McIlwain, 1971; Chepuri, Jaynes, Turner, et al., 2023). We looked at the behavior of chorus wave events during the quiet period following an injection. We identified these events with the following process:

1. Smooth the SME index with a rolling average of 6 minutes.
2. Identify periods where the SME index stayed below 150 nT for at least 10 minutes.
3. From these periods, select only those that were preceded by an enhancement in SME of > 250 nT.

Our threshold of < 150 nT, representing the start of a quiet period, is based on Meredith, Horne, Johnstone, and Anderson (2000) and we found that > 250 nT was sufficient to identify enhanced periods without over-identifying.

We also measured the approximate injection length from the time when SME went above 250 nT to when it dropped below 150 nT. Our median injection length from 6241 events was 1.73 ± 0.02 hr.

3.2.3 Chorus Selection

Within the quiet periods after injections, we further limited our search to the outer radiation belt ($3 \leq L \leq 6.6$) and considered all MLTs, and all magnetic latitudes sampled by the Van Allen Probes ($-20^\circ \leq \text{MLAT} \leq 20^\circ$).

To identify chorus we determined the local electron cyclotron frequency (f_{ce}) using the magnetic field amplitude from the EMFISIS flux gate magnetometer (MAG) and the approximation $f_{ce}[\text{Hz}] = \left| \vec{B}[\text{nT}] \right| \times 28$. We then used local f_{ce} to select chorus from the power spectral density (SD) data. To qualify as a measurement of LBC or UBC we required that the max magnetic

field SD over the respective frequency range be $\geq 10^{-7} \text{ nT}^2/\text{Hz}$ (Hartley, Kletzing, Chen, et al., 2019). To reduce hiss noise, we ensured that the probes were outside the plasmasphere by limiting our measurements to times when the electron density was less than the smaller of $10 \times (6.6/L)^4$ or 50 cm^{-3} (Lawrence, Thomsen, Borovsky, & McComas, 1999; Sheeley, Moldwin, Rassoul, & Anderson, 2001; Aryan, Bortnik, Sibeck, & Hospodarsky, 2022). Note that in Sheeley, Moldwin, Rassoul, and Anderson (2001) the equation is written as $10 \times (6.6/L)^{-4}$, but we believe that this is a typo. Subsequent studies have implemented the equation we used to good results and it is intuitive that the density threshold would decrease at larger L values. For the density we used the estimated values provided by EMFISIS.

3.3 Analysis

In total, we found 224,165 chorus measurements. Each measurement contains an integrated LBC and/or UBC wave power for both the magnetic and electric fields, probe location, and a time since the start of the respective quiet period. We can use this dataset to better understand how chorus waves behave after a substorm.

3.3.1 Variations With Magnetic Local Time

We further subdivided our dataset into the following regions of MLT: 21 to 3, 3 to 6, 6 to 9, 9 to 12, 12 to 15, and 15 to 18. We excluded 18 to 21, and combined 21 to 24 and 0 to 3 due to limited chorus observations in these region. While it isn't the purpose of this study, it is worth noting that our statistical distribution does roughly agree with the previous understanding of chorus occurrence and wave power in relation to MLT (Li, Santolik, Bortnik, et al., 2016; Meredith, Horne, Shen, et al., 2020). Occurrence and wave power peaks post-midnight and are lowest between 18 and 21 MLT.

For each MLT region we fit an exponential decay in form of

$$B = B_0 e^{-t/\tau}$$

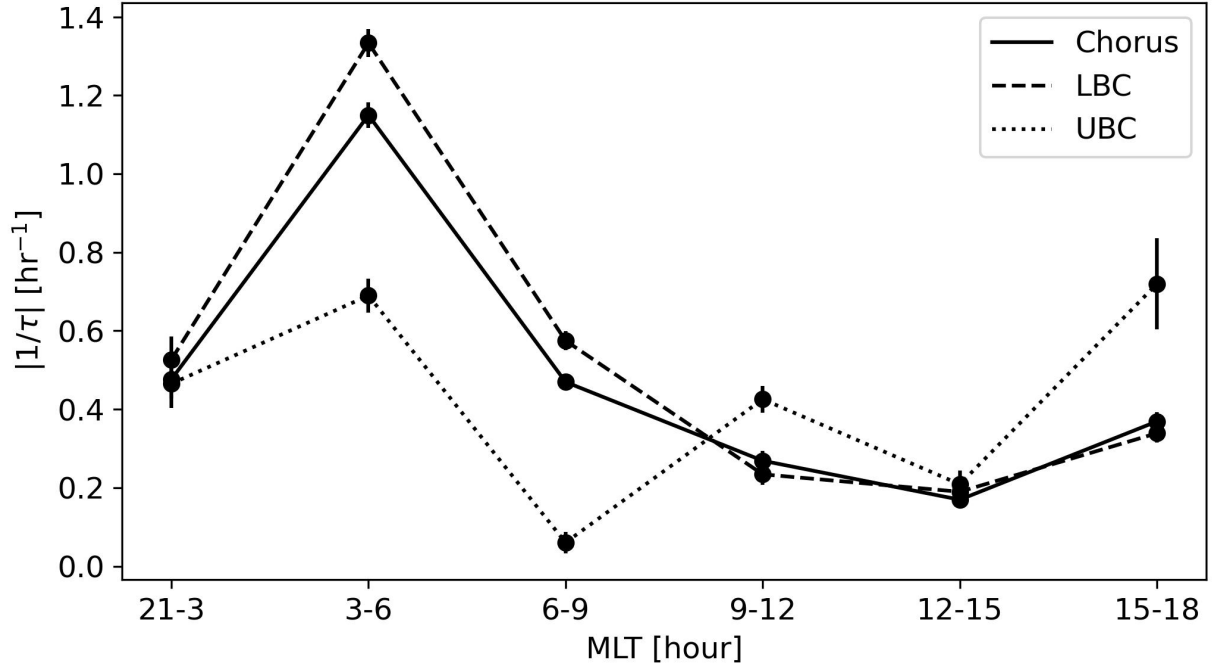


Figure 17. The inverse of magnetic field wave power decay timescales for the entire chorus range (solid), LBC (dashed), and UBC (dotted) versus MLT. For many of the points, the associated errors are smaller than the marker size. We combined the region 21 to 24 and 0 to 3 MLT and omitted 18 to 21 MLT due to statistical limitations.

to the integrated magnetic wave power. Where t is the time since the start of a quiet period. We limited this fit to the first 75 minutes. Figure 17 shows how the inverse of this decay e-folding time (τ) varies across our MLT regions. We chose to plot $|1/\tau|$ to better distinguish between differences in decay timescales. We split the decays into full chorus (solid), LBC (dashed), and UBC (dotted) lines to visualize the differences between wave frequency. Using Figure 17 we find that the fastest decays occur in the night to early morning regions, with larger timescales in the daytime. The fastest decay occurs between 3 to 6 MLT and in this region the LBC decays about twice as fast as the UBC. This region of MLT also happens to be the most common time for pulsating aurora (Kvifte & Pettersen, 1969) and we will discuss that connection in Section 3.3.4.

3.3.2 Variations With Magnetic Latitude

In Figure 17 we saw that decay timescales in the night and early morning were faster than in the daytime. To look at changes with magnetic latitude (MLAT), we divided our data into two MLT bins: 21 to 9, and 9 to 18. In Figure 18 we plotted the difference in decay timescales between these two regions and for 0° to 10° and 10° to 20° MLAT. From this we find that the fastest decay occurs near the equator in the 21 to 9 MLT region. The timescale at higher latitudes is slower and not as uniform with an increase in wave power around 0.5 hours after the quiet period start. In the 9 to 18 MLT region the opposite is true. At high latitudes the decay is more uniform and faster than near the equator. Near the equator there is very little decay in wave power until around 1.25 to 1.5 hours after the quiet period start. We do not have enough information to say for sure what could be causing these variations, but one possibility is particle energy. Chorus waves resonate with higher energy electrons at higher latitudes (Horne & Thorne, 2003; Miyoshi, Saito, Kurita, et al., 2020). Higher energy electrons have a larger drift velocity and so we would expect chorus waves to react faster at high latitudes after an injection. From Equation 1.14, it takes about 1.5 hours for a 30 keV electron to drift 12 hours of MLT at $L=5$. If electrons with energies larger than this resonate mostly above 10° then the delayed decay in Figure 18 Panel B could be due to this drift time.

The increase in wave power at 0.5 hours in Figure 18 Panel C is mostly from the 6 to 9 MLT region. Because this signature does not show up at lower latitudes, it may be due to higher energy electrons that have completed one full drift period and are continuing to drive chorus on their second pass through the region. From Gabrielse, Angelopoulos, Runov, and Turner (2014), 23 MLT is the most common region for dispersionless electron injections at $L<12$. Given this and our median injection length of 1.7 hours, an electron would need to drift roughly 31 MLT over 2.2 hours. This would correspond to approximately 60 keV electrons at $L=5$.

3.3.3 Comparison With Meredith Et Al. (2000)

Meredith, Horne, Johnstone, and Anderson (2000) used electric field measurements from the CRRES spacecraft and found a chorus amplitude decay timescale after injections of 1.1 ± 0.2

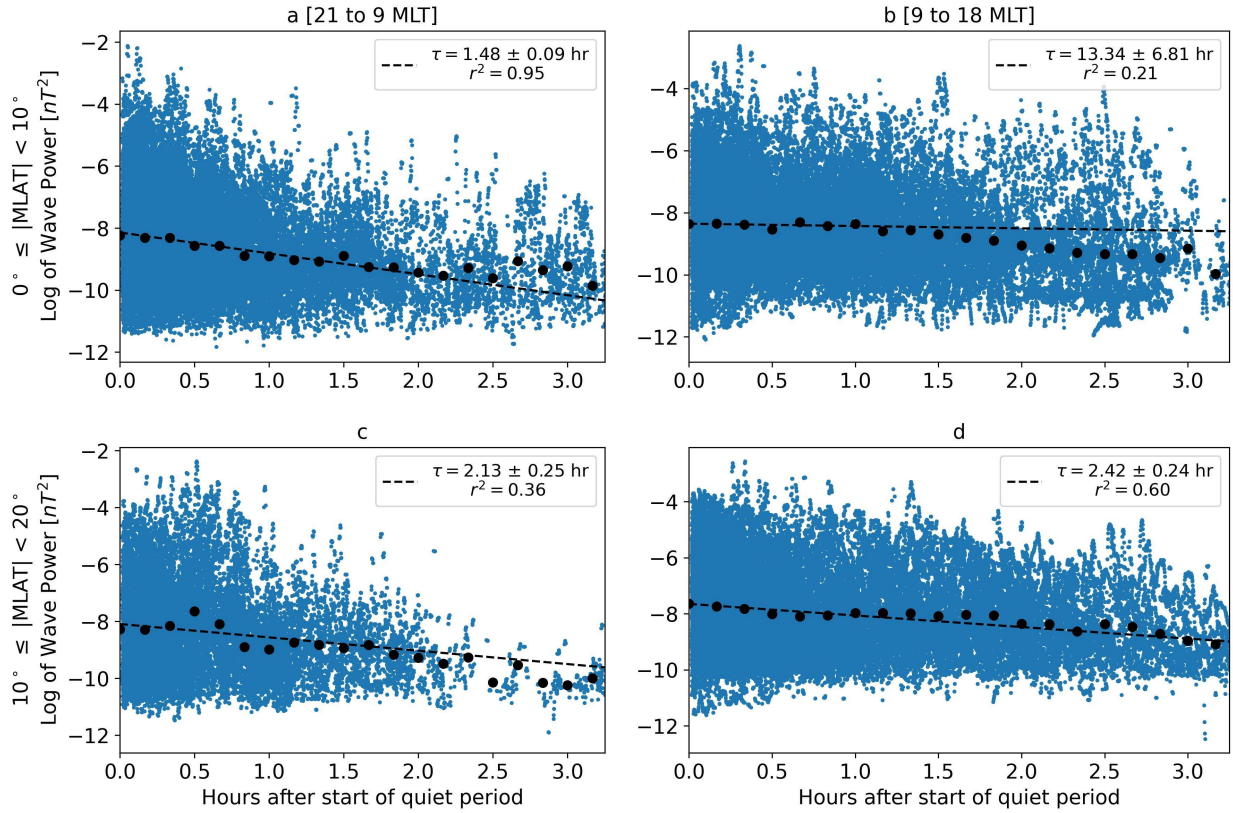


Figure 18. Statistical behavior, during the quiet period following substorms, of magnetic chorus wave power. The left (right) column of figures shows the behavior in the 21 to 9 MLT (9 to 18 MLT) region. The top (bottom) row of figures shows the behavior for 0° to 10° (10° to 20°) MLAT. The blue scatter points are the underlying data, the black scatter points are the geometric mean value of the proceeding 10 minutes of data. The dashed line is the best exponential decay to the first 75 minutes of data. Note that the wave power is natural log transformed.

hr in the region 21 to 6 MLT and $3.8 \leq L < 7$. This would correspond to a 0.55 hr decay in the wave power. To compare our data to this value we used the EMFISIS electric field measurements. We then found the electric wave power decay in the region 21 to 6 MLT, $\pm 5^\circ$ magnetic latitude, $3.8 \leq L \leq 6.6$, and fit our decay to the first 3 hours. Given these parameters we find that the electric wave power decays with a timescale of 1.20 ± 0.07 hr. This more than double that of Meredith, Horne, Johnstone, and Anderson (2000). There are a several possible reasons for this. One is the statistical sample size as they were working with < 20 data points compared to our much larger dataset. A second is the method of identifying injection periods. Our automated identification allows us to analyze the large EMFISIS dataset, but may include weaker injection periods that a human identifier would overlook. A third could be variations between our statistical sets. From Figure 3 of Meredith, Horne, Johnstone, and Anderson (2000) it appears that they had the most measurements in the MLT bins around midnight, while we had comparatively few in this region. As we've seen in Figure 17, decay time is highly dependent on MLT. Thus, when averaging over a large region of MLT, differences in the statistical distribution would likely change the results.

3.3.4 Comparison With Pulsating Aurora

In Chapter 2 we found that the contribution to the total energy flux from ≥ 30 keV electrons during pulsating aurora decayed after substorms. Figure 19 shows a best fit decay plot using the data from Chapter 2. The blue scatter points are the underlying data, the black points represent the geometric mean value of the surrounding 20 minutes, and the red line is the best fit exponential. Here we see that ≥ 30 keV pulsating aurora electrons decay with a timescale of 0.95 ± 0.11 hr after substorms. The method we used to calculate the uncertainty in the decay time is described in Section 3.3.6. To compare that decay time to the data in this chapter we considered the difference between chorus types since LBC has been directly linked to pulsating aurora, while UBC is more commonly associated with the less energetic non-pulsating diffuse aurora (Meredith, Horne, Thorne, & Anderson, 2009; Nishimura, Bortnik, Li, et al., 2010). This is not surprising as LBC waves resonate with higher energy electrons (> 5 keV) compared to UBC waves (< 5 keV) (Ni,

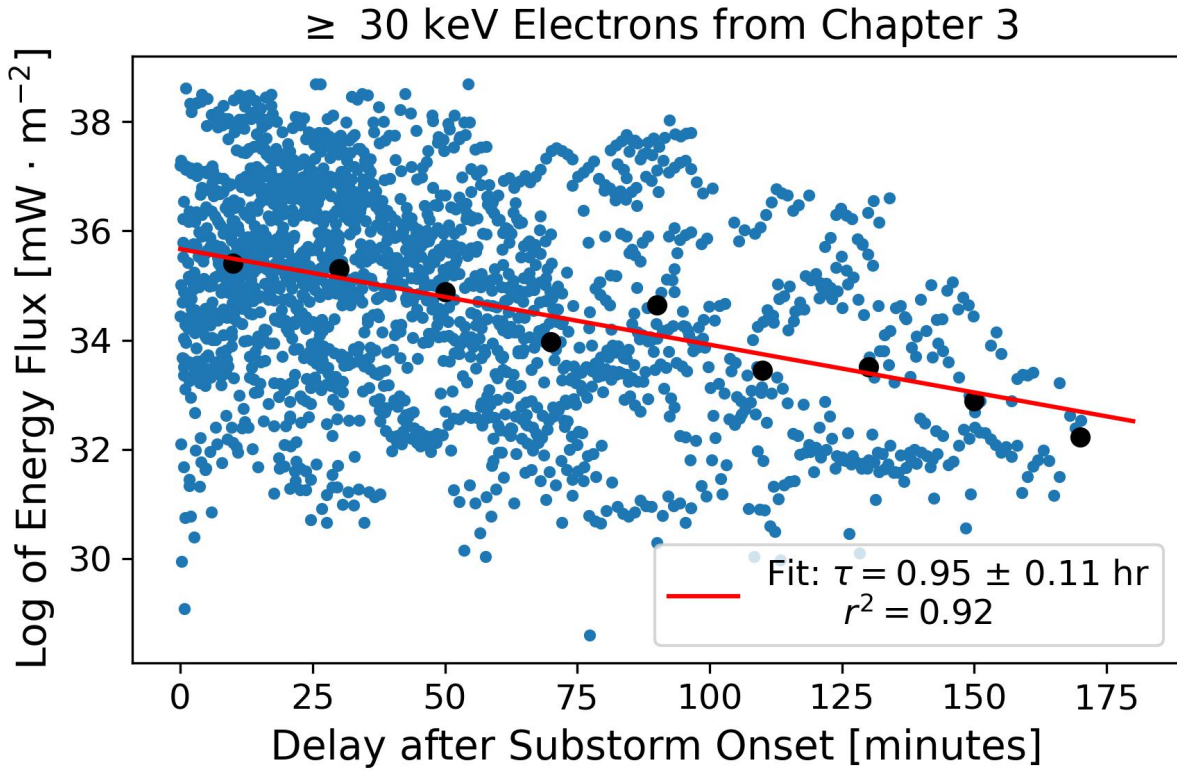


Figure 19. Figure using the data from Chapter 2 showing the decay of ≥ 30 keV pulsating aurora electrons after substorms. The blue scatter points indicate the underlying data, the black scatter points are the geometric mean values of the surrounding 20 minutes of energy flux, and the red line is the best fit exponential decay. The r^2 value is based on the fit to the black scatter points. Note that the energy flux is natural log transformed.

Thorne, Shprits, & Bortnik, 2008). In Figure 17 we binned by chorus type in addition to MLT and saw that during the most common time for pulsating aurora (3 to 6 MLT), LBC decays with a faster timescale than UBC (Kvifte & Pettersen, 1969; Jones, Lessard, Rychert, et al., 2011). For a more direct comparison to the decay timescale of Chapter 2, in Figure 20, we show the difference between LBC and UBC in the region 21 to 5 MLT, $3 < L < 6.6$, and -20° to 20° MLAT. Here we can see a clear difference between the two chorus types with LBC decaying nearly twice as quickly compared to UBC. Additionally, comparing the timescale of the LBC decay to the timescale of ≥ 30 keV electrons from Figure 19 we see that they match within uncertainty.

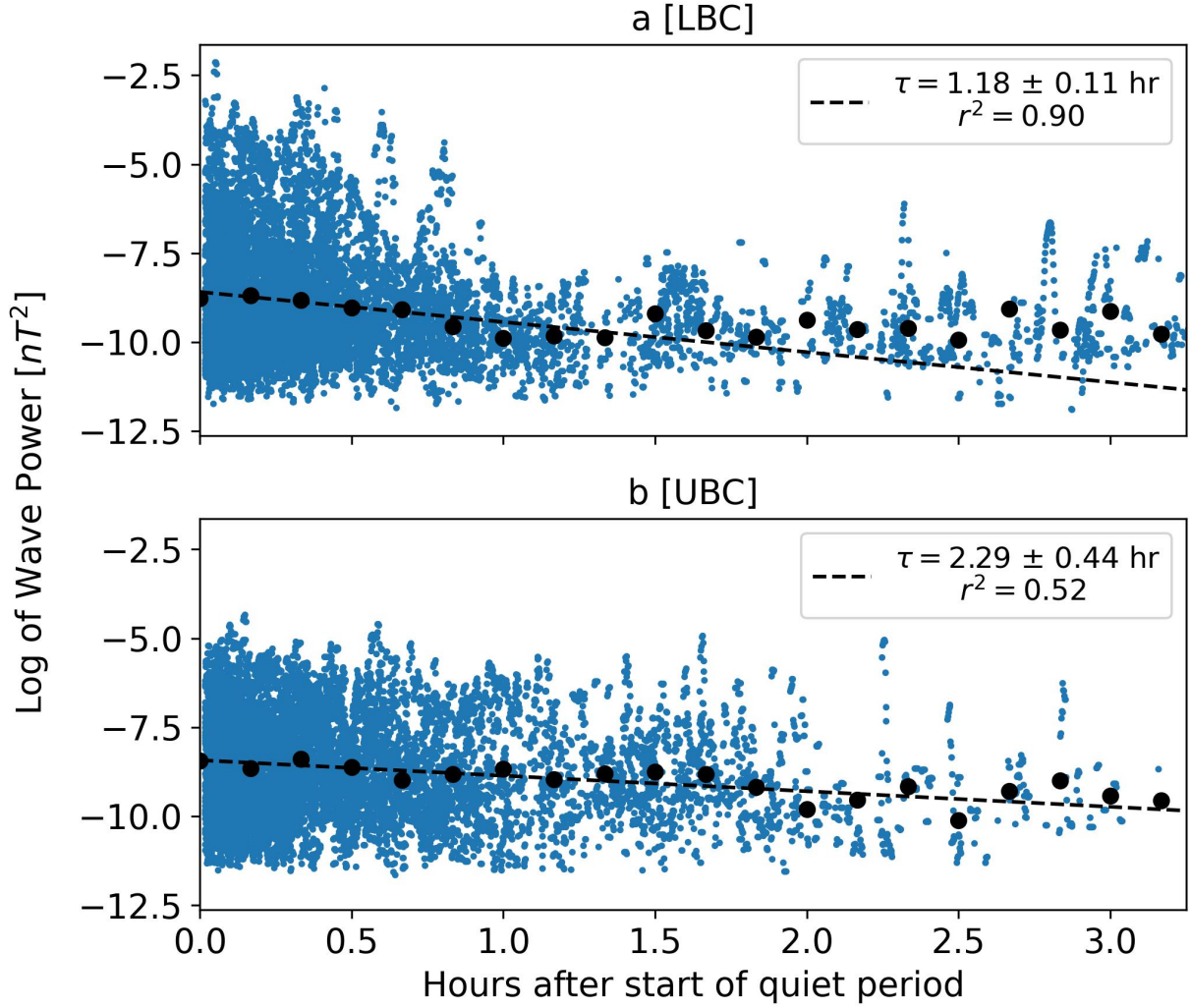


Figure 20. Statistical behavior of magnetic wave power, during the quiet period following substorms, from the LBC [a] and UBC [b] frequency ranges. Data in the figure is from the region 21 to 5 MLT, $3 < L < 6.6$, and -20° to 20° MLAT. The blue scatter points indicate the underlying data, the black scatter points are the geometric mean value of the preceding 10 minutes of data. The dashed black line is the best exponential decay to the first 75 minutes of data. Note that the wave power is natural log transformed.

3.3.5 Simulation

As another test, we modelled the system using the quasi-linear, drift-averaged, diffusion simulation described in Hua, Bortnik, and Ma (2022). To calculate the diffusion coefficients, we set the wave power in the 21 to 3, 3 to 6, and 6 to 9 MLT regions to

$$B_w(t) = B_0 e^{-t/\tau}$$

where t is the simulation time, τ is the decay timescale that we measured for the specific region, and B_0 is the max wave intensity in the region taken from Meredith, Horne, Shen, et al. (2020) at $L = 5$ and $100 \leq AE < 300$ nT. In all other regions we let $B_w(t) = B_0$.

We used the values of Meredith, Horne, Shen, et al. (2020) for B_0 because they provide a large sample size over our MLT bins and have been used in similar simulations (Hua, Bortnik, & Ma, 2022; Hua, Bortnik, Kellerman, et al., 2023). Although it wasn't the primary focus of this work, we can also derive B_0 from our data. Doing so, we find that it differs from Meredith, Horne, Shen, et al. (2020). For instance, we see a peak B_0 on the order of 20 pT in the 3 to 6 MLT region, while for $AE < 100$ nT, Meredith, Horne, Shen, et al. (2020) found it to be on the order of 40-50 pT. We believe this is due to different averaging techniques. Meredith, Horne, Shen, et al. (2020) used an arithmetic mean, while we used a geometric mean because the chorus power distribution is spread over multiple orders of magnitude. Using an arithmetic mean we get B_0 on the order of 40 pT.

Figure 21 summarizes the results of our simulation. Panel A shows how the initial electron energy distribution decays over the simulation. We report the electron distribution in units of spin-averaged flux as the Van Allen Probes ECT instrument would measure it (Spence, Reeves, Baker, et al., 2013; Boyd, Reeves, Spence, et al., 2019). We took the initial flux as measured by ECT from the October 25, 2016 storm event (Hua, Bortnik, & Ma, 2022). In panel A we've marked the region of strong diffusion (14 keV to 125 keV) with solid black lines. We've also marked 30 keV with a dashed red line to match the threshold from Chapter 2. Panel B shows the summed

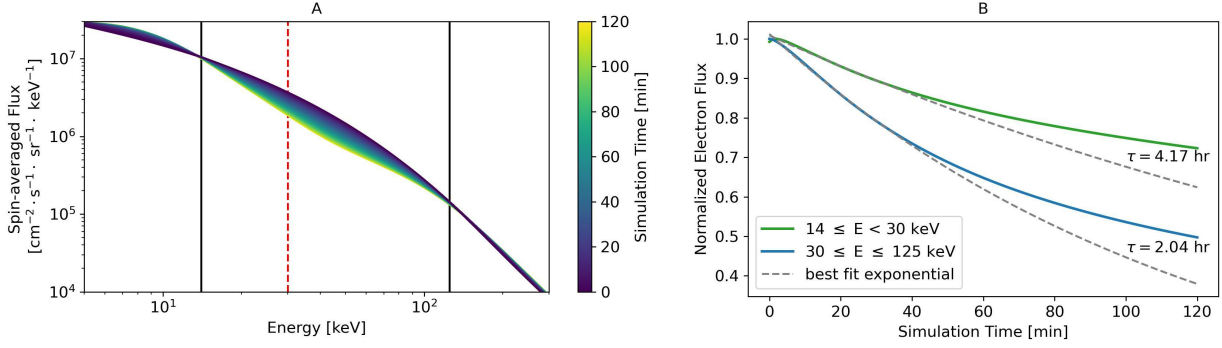


Figure 21. Results from our quasi-linear diffusion simulation of chorus waves. Panel A shows how the initial electron energy distribution decays over the simulation. The solid black lines indicate 14 keV and 125 keV and are the approximate bounds of strong diffusion. The dashed red line indicates 30 keV, which we define as the boundary between high and low energy electrons. Panel B shows the summed decay of low ($14 \text{ keV} \leq E < 30 \text{ keV}$) and high ($30 \text{ keV} \leq E \leq 125 \text{ keV}$) electrons within the region of strong diffusion. The solid lines indicate the normalized flux decays, while the dashed gray lines are the best fit exponentials for the first 30 minutes of the simulation.

electron flux, in the region of strong diffusion, for low-energy electrons ($14 \text{ keV} \leq E < 30 \text{ keV}$) and high-energy electrons ($30 \text{ keV} \leq E \leq 125 \text{ keV}$).

Due to the drift-averaged nature of the simulation, we can't directly compare these decay timescales to timescales measured in a specific region of MLT, although they are on the same order of magnitude. We can, however, investigate the relative differences between the higher and lower energy electrons. In Figure 21B we see that, in the first 30 minutes of the simulation, the $\geq 30 \text{ keV}$ electrons decay with a timescale of 2.04 hr. The $< 30 \text{ keV}$ electrons decay about twice as slowly, with a timescale of 4.17 hr. In Chapter 2 we saw that the decay in energy flux during pulsating aurora was mainly due to a reduction in the $\geq 30 \text{ keV}$ electrons. This agrees well with our simulation and provides further evidence linking energetic pulsating aurora to precipitation caused by substorm driven chorus waves.

3.3.6 Errors

To understand the quality of our exponential fits we used two different methods. We estimated the error in τ by bootstrapping (Johnson, 2001). To bootstrap, we resampled our distribution

10,000 times, with replacement, and found the slope for these new distributions. We then used the standard deviation of these 10,000 resampled slopes as the associated error, propagating this to our timescale given that slope = $-1/\tau$. To estimate the quality of each fit we calculated R^2 values between the best fit exponential and the geometric means values of the distribution.

3.4 Discussion

Doppler shifted resonance with injected energetic electrons is one proposed mechanism for chorus wave growth (Brice, 1964; Kennel & Petschek, 1966). In this process the electron interacts with the perpendicular electric field, causing it to transfer energy to the wave and reducing the pitch angle. To keep wave growth active the average velocity of the electrons perpendicular to the magnetic field must be greater than the average parallel velocity (Brice, 1964). Qualitatively, our results are consistent with this process. During injections, electrons typically enter the outer radiation belt just before magnetic midnight (Gabrielse, Angelopoulos, Runov, & Turner, 2014). They then gradient-curvature drift eastward, overtaking the slower, less energetic plasma population. The interaction of these two populations can provide the anisotropies necessary for pitch angle scattering (Oguti, 1976). As time progresses the electron distribution, and correspondingly wave activity, will tend towards an equilibrium Kennel and Petschek (1966). Thus, chorus wave activity should have less time dependence further eastward (later MLT). This is what we see in Figure 17, with the fastest decay times between 3 to 6 MLT and the slowest times in later MLT bins.

Performing a quantitative analysis of the decay timescales is more challenging and not something we will attempt in this chapter. To do so we would need to take several aspects of the system into consideration. One is the energy dispersion due to gradient-curvature drift. Higher energy electrons will drift eastward at a faster rate, meaning the lower energy electrons will last longer in a particular MLT region. A second is the energy and pitch angle distribution of the injected electrons. The process that drives chorus growth simultaneously reduces the electron energy and pitch angle. After enough interactions an electron that was originally resonant will

either precipitate into the atmosphere or lose enough energy that it is no longer resonant. A third is the temporal and spatial scale of the injection. For a longer and wider injection, by the time we take our measurement, the electron population will be spread over a larger region of MLT. We were able to estimate the median length of the injections as 1.73 ± 0.02 hours, but have no measure of the spatial extent. In Section 3.3.5 we were able to simulate an approximation of these events, but to understand the underlying physics we would need to specifically model the processes just after a substorm. While we did not perform that analysis, we hope that our measured decay timescales will provide a means to test future models.

The decay timescale similarity between LBC in the 21 to 5 MLT region and the energy flux of energetic pulsating aurora is striking, but also not a smoking gun. Our results should be considered as additional statistical evidence linking energetic pulsating aurora to LBC and substorms. Combined with prior studies, LBC certainly appear to play an important role in the formation of pulsating aurora, but the specific processes are likely more complicated than we've outlined here.

3.4.1 Magnetic And Electric Field Differences

To compare with Meredith, Horne, Johnstone, and Anderson (2000) we also analysed the electric wave power for our chorus measurements. Due to data quality, we believe the magnetic field analysis is more reliable and so chose to focus on it for our results. However, during our analysis, we did find several differences between the magnetic and electric decay timescales. The largest difference was in the region 21 to 3 MLT, where $\tau_{\text{electric}} < \tau_{\text{magnetic}}$, and for 3 to 6 MLT, where $\tau_{\text{electric}} > \tau_{\text{magnetic}}$. We've included a plot showing this in the additional materials. We do not fully understand how this would occur, but there are a couple possibilities. One is wave normal angle of the chorus that, as Li, Santolik, Bortnik, et al. (2016) found, varies with MLT. Waves in the 3 to 6 MLT region are less field aligned (larger wave normal angle) than those close to midnight. They also found that waves with angles $> 40^\circ$ tend to have weaker magnetic field power compared with angles $< 30^\circ$, while the electric field is comparable. Another reason for the difference might be the changing distribution of injected electrons. As Kennel and Petschek

(1966) showed, in anisotropic distributions skewed towards 90° pitch angles, the wave electric forces dominate the magnetic forces, while the opposite is true for distributions skewed towards 0° . According to Gabrielse, Angelopoulos, Runov, and Turner (2014), just before midnight is the most probable time for an injection. This injection may drive chorus growth with initially strong wave electric forces in the midnight region. As the electrons drift eastward their pitch angles will decrease, reducing the dominance of the electric forces while increasing that of the magnetic forces. However, both of these connections are highly speculative and we would need to conduct additional work to determine if they could cause our observed decay time differences.

3.5 Summary

In this chapter, we found that chorus waves exponentially decay in the quiet period following a substorm. The timescale of this decay varies based on magnetic local time (MLT), magnetic latitude, and frequency range. The fastest decay timescales occurred for lower-band chorus waves between 21 to 9 MLT with a peak at 3 to 6 MLT. We found that the lower-band chorus magnetic field power spectral density decays in the region 21 to 5 MLT with a timescale of 1.18 ± 0.11 hr. This agrees with the 0.95 ± 0.11 hr timescale that we measured in Chapter 2 for ≥ 30 keV pulsating aurora electrons after substorms. We also modeled our findings in a quasi-linear diffusion simulation and found that ≥ 30 keV electrons decay around twice as fast compared to the < 30 keV population. These statistical decay timescales provide a valuable metric that can be used to track processes through the magnetosphere-ionosphere system and to test the validity of future models.

3.6 Additional Tables And Figures

Table 1. Full chorus, LBC, and UBC magnetic (B) and electric (E) SD decay timescales (τ) and peak wave magnetic field (B_w) for the midnight (21 to 3 MLT) region. We included error, R^2 values, and the number of statistics for the magnetic field measurements (N_B) to contextualize the quality of each fit.

Type	τ_B	B_w	R_B^2	τ_E	R_E^2	N_B
Chorus	2.10 ± 0.43 hr	15.2 pT	0.85	0.73 ± 0.07 hr	0.61	12123
LBC	1.90 ± 0.43 hr	11.9 pT	0.70	1.00 ± 0.20 hr	0.80	7780
UBC	2.15 ± 0.57 hr	15.9 pT	0.57	0.97 ± 0.15 hr	0.18	6862

Table 2. Full chorus, LBC, and UBC magnetic (B) and electric (E) SD decay timescales (τ) and peak wave magnetic field (B_w) for the predawn (3 to 6 MLT) region. We included error, R^2 values, and the number of statistics for the magnetic field measurements (N_B) to contextualize the quality of each fit.

Type	τ_B	B_w	R_B^2	τ_E	R_E^2	N_B
Chorus	0.87 ± 0.05 hr	19.0 pT	0.97	2.90 ± 0.69 hr	0.55	19495
LBC	0.75 ± 0.04 hr	18.7 pT	0.96	5.16 ± 3.09 hr	0.48	14341
UBC	1.45 ± 0.18 hr	14.5 pT	0.47	2.97 ± 0.80 hr	0.49	10041

Table 3. Full chorus, LBC, and UBC magnetic (B) and electric (E) SD decay timescales (τ) and peak wave magnetic field (B_w) for the dawn (6 to 9 MLT) region. We included error, R^2 values, and the number of statistics for the magnetic field measurements (N_B) to contextualize the quality of each fit.

Type	τ_B	B_w	R_B^2	τ_E	R_E^2	N_B
Chorus	2.13 ± 0.19 hr	16.4 pT	0.54	2.61 ± 0.35 hr	0.85	35161
LBC	1.74 ± 0.15 hr	16.5 pT	0.58	2.87 ± 0.51 hr	0.73	28233
UBC	16.57 ± 15.28 hr	11.9 pT	0.23	7.53 ± 3.20 hr	0.03	12478

Table 4. Full chorus, LBC, and UBC magnetic (B) and electric (E) SD decay timescales (τ) and peak wave magnetic field (B_w) for the morning (9 to 12 MLT) region. We included error, R^2 values, and the number of statistics for the magnetic field measurements (N_B) to contextualize the quality of each fit.

Type	τ_B	B_w	R_B^2	τ_E	R_E^2	N_B
Chorus	3.72 ± 0.68 hr	18.9 pT	0.83	4.08 ± 0.87 hr	0.64	33133
LBC	4.27 ± 0.97 hr	19.3 pT	0.75	2.63 ± 0.42 hr	0.66	28816
UBC	2.35 ± 0.38 hr	12.3 pT	0.51	-3.61 ± 1.12 hr	0.12	9240

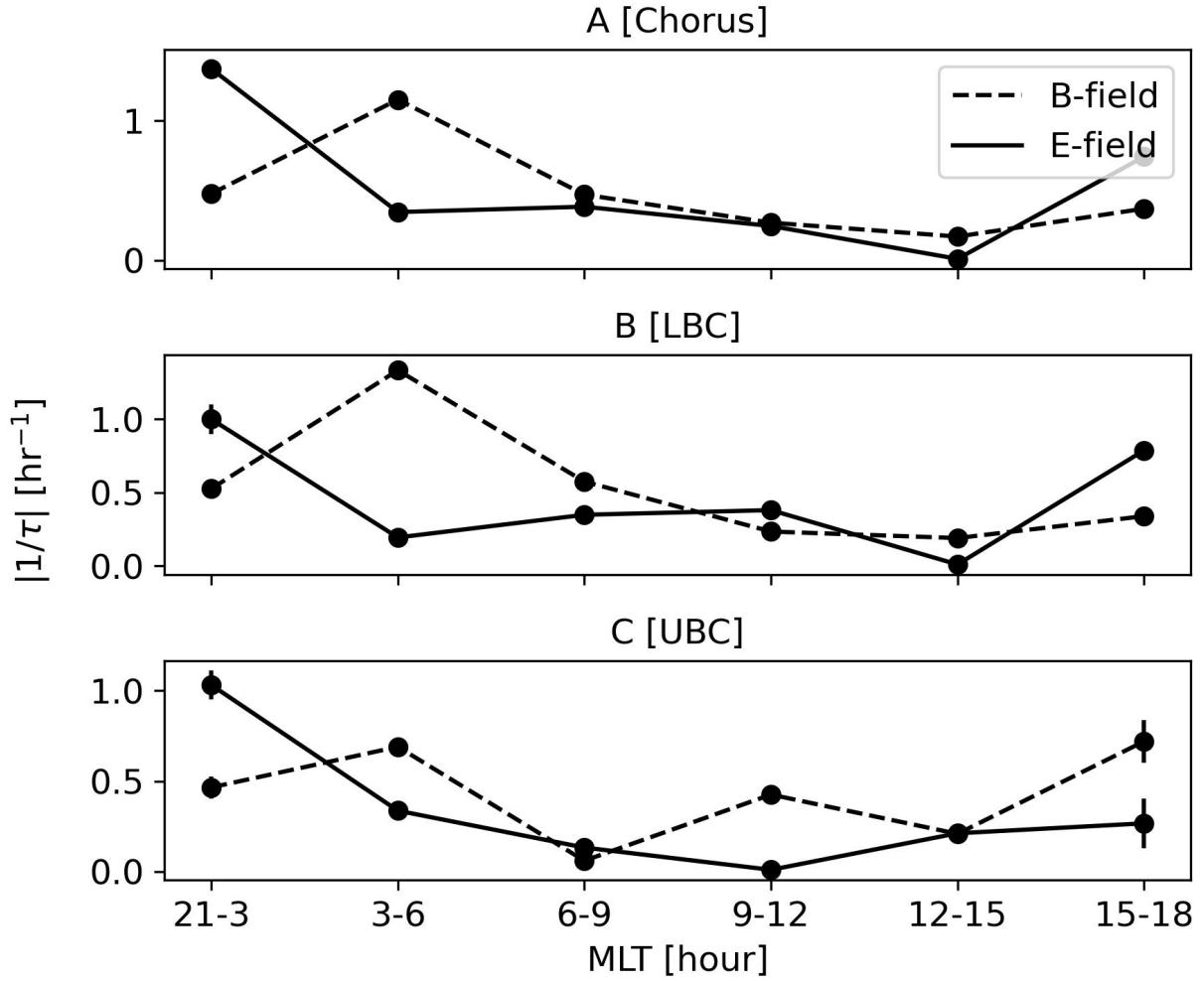


Figure 22. The inverse of magnetic (dashed) and electric (solid) field wave power decay rates for the entire chorus range (Panel A), LBC (Panel B), and UBC (Panel C) versus MLT. For many of the points, the associated errors are smaller than the marker size. We combined the region 21 to 24 and 0 to 3 MLT and omitted 18 to 21 MLT due to statistical limitations.

Table 5. Full chorus, LBC, and UBC magnetic (B) and electric (E) SD decay timescales (τ) and peak wave magnetic field (B_w) for the afternoon (12 to 15 MLT) region. We included error, R^2 values, and the number of statistics for the magnetic field measurements (N_B) to contextualize the quality of each fit.

Type	τ_B	B_w	R_B^2	τ_E	R_E^2	N_B
Chorus	5.90 ± 1.49 hr	18.3 pT	0.34	-7.36 ± 2.52 hr	0.27	39868
LBC	5.27 ± 1.22 hr	18.3 pT	0.40	-5.70 ± 1.56 hr	0.46	38363
UBC	4.79 ± 1.63 hr	10.8 pT	0.58	4.72 ± 1.81 hr	0.30	5274

Table 6. Full chorus, LBC, and UBC magnetic (B) and electric (E) SD decay timescales (τ) and peak wave magnetic field (B_w) for the evening (15 to 18 MLT) region. We included error, R^2 values, and the number of statistics for the magnetic field measurements (N_B) to contextualize the quality of each fit.

Type	τ_B	B_w	R_B^2	τ_E	R_E^2	N_B
Chorus	2.71 ± 0.35 hr	15.0 pT	0.25	1.35 ± 0.14 hr	0.67	14665
LBC	2.95 ± 0.42 hr	14.9 pT	0.22	1.27 ± 0.13 hr	0.69	14265
UBC	1.39 ± 0.45 hr	10.8 pT	0.07	3.75 ± 3.88 hr	0.03	937

CHAPTER 4: THE DIFFUSE AURORAL ERASER

4.1 Introduction

In Chapters 2 and 3 we've closely studied pulsating aurora. Pulsating aurora is a very important subset of diffuse-like aurora. It also happens to be incredibly variable in both energy and appearance. The field is beginning to build up a picture of how typical, strong pulsating aurora forms. This is important and consequential for our understanding of the magnetosphere-ionosphere system. However, to truly understand the system as a whole we will also need to focus some energy on edge cases. There have been observations of other types of diffuse-like and dynamic aurora, but relatively little research into this area. In this chapter, we present one such observation and attempt to quantify some of its characteristics.

Originally referred to as mantle aurora, diffuse aurora appears as a faint glow, just visible to the naked eye, and spread across a large portion of the sky (Lui, Perreault, Akasofu, & Anger, 1973). The location of this aurora occurs equatorward of the discrete auroral oval and usually peaks in activity and brightness after magnetic midnight. This typically corresponds to between 60° and 75° corrected geomagnetic latitude, depending on the solar cycle and geomagnetic activity (Sandford, 1968; Feldstein & Galperin, 1985). Work by Sandford (1968) showed, by integrating the 3914\AA emission over the auroral zone, that during solar maximum, diffuse aurora accounts for 80% of auroral emission, however during solar minimum that was reduced to only 50%. While discrete aurora are much brighter and better known, diffuse-like aurora play an important role in the magnetosphere - ionosphere (MI) system because they are so common and thus are one of the largest sources of energy transfer between the two regions of geospace (Newell, Sotirelis, & Wing, 2009). The glow of diffuse aurora is the result of 100s of eV to 10s of keV electron precipitation from the plasma sheet (Meng, Mauk, & McIlwain, 1979). Many studies have identified wave-particle interactions in the plasma sheet as the primary way that this precipitation occurs. The waves responsible are electron cyclotron harmonic (ECH) and upper-band chorus (UBC) waves (e.g., Meredith, Horne, Thorne, & Anderson, 2009; Thorne, Ni, Tao, et al., 2010; Ni, Thorne,

Zhang, et al., 2016, and others). ECH waves are electrostatic perturbations whose frequencies fall between harmonics of the electron gyrofrequency (f_{ce}) (e.g., Kennel, Scarf, Fredricks, et al., 1970; Fredricks & Scarf, 1973; Shaw & Gurnett, 1975; Gurnett, Anderson, Tsurutani, et al., 1979, and others). UBC waves are electromagnetic and a subset of whistler mode chorus waves with frequencies between $0.5f_{ce} < f < f_{ce}$ (e.g., Tsurutani & Smith, 1974; Burtis & Helliwell, 1976, and others). They differ from lower-band chorus (LBC) waves, which cover the frequency range $0.1f_{ce} < f < 0.5f_{ce}$. ECH and UBC waves also scatter slightly different energy electrons. ECH waves are most efficient between a few hundred eV to a few keV while chorus are most efficient below a few hundred eV (Horne, 2003). While most studies have linked ECH and UBC waves as the primary source of diffuse aurora, there is also a case to be made for whistler mode hiss waves, which have frequencies below $0.1f_{ce}$. These waves resonate best with electrons of energies above a few keV (Horne, 2003).

Despite their usual static appearance, diffuse aurora often occur alongside the more dynamic pulsating aurora (Davis, 1978). Typical pulsating aurora are characterized by widely varying diffuse-like patches that blink on and off with periods between 2 to 20 seconds (e.g., Davis, 1978; Lessard, 2013, and others) and can be widespread and long-lasting (Jones, Lessard, Rychert, et al., 2013). While they frequently happen during diffuse aurora, studies have shown that pulsating aurora originate from a different wave-particle interaction. This interaction happens in the outer radiation belt between LBC waves and a few to 100s of keV electrons (e.g., Nishimura, Bortnik, Li, et al., 2010; Nishimura, Bortnik, Li, et al., 2011; A. N. Jaynes, Lessard, Rodriguez, et al., 2013; Kasahara, Miyoshi, Yokota, et al., 2018). Another, less studied, phenomenon associated with diffuse-like aurora is black aurora. These are defined regions within an auroral patch that have no emissions (Davis, 1978; T. S. Trondsen & Cogger, 1997; Fritz, Lessard, Blandin, & Fernandes, 2015). The exact cause of these aurora is still unknown.

Both typical pulsating aurora and black aurora appeared on the night of our data, although our data did not capture the typical pulsating aurora. However, our focus was on an unusual phenomenon, similar to Dahlgren, Lanchester, Ivchenko, and Whiter (2017), who used a high

frame-rate, narrow field-of-view camera to study the rise and fall times of pulsating auroral patches. They reported several examples of a dip in intensity to below the background “off” level, which then recovered to the background over several seconds. The events we report on are characterized by a diffuse arc, which appears, then rapidly disappears, blacking out the diffuse aurora in the region. However, these events differ from Dahlgren, Lanchester, Ivchenko, and Whiter (2017) in that they tend to be isolated instead of periodic in time, although several events we observed did repeat for several periods. It is not clear that they are part of the same phenomenon. We quantify and report here the statistical distribution of recovery times of these features, which we call “eraser” events. The events appear in images taken during a 2 hour period the night of March 15, 2002, during a campaign in Churchill, MB, Canada. While the campaign lasted for several days, this was the only night that these events appeared. In addition, during that night we only observed these events during this 2 hour window. This auroral feature is worth investigating since it could lead to a better understanding of diffuse-like aurora and the associated waves. What process in the equatorial magnetosphere can turn off diffuse auroral emissions in localized regions?

4.2 Data

The images used in this analysis were taken from an intensified, narrow field-of-view (FOV) CCD-based TV camera known as the Portable Auroral Imager (PAI) (T. S. Trondsen & Cogger, 1997). They were taken at 30 frames-per-second (fps) and span from approximately 6:40 to 8:40 universal time (UT) or 0:06 to 2:06 magnetic local time (MLT) on March 15, 2002. The PAI was mounted to a tripod, which was on the ground at a location near Churchill, Manitoba. This corresponds to 69.28° latitude and 331.22° longitude in AACGM coordinates. It was pointed manually during the nightly observations and equipped with a 25 mm lens in addition to a Wratten 89B IR filter with a cutoff wavelength of 650 nm. T. Trondsen (1998) describes the PAI used to collect the data in more detail. This setup resulted in a 30.9° by 23.2° FOV. Given an image size of 640 by 480 pixels, the single pixel resolution is about 88 m by 88 m at an altitude of 105 km (T. Trondsen, 1998). Using a section of Ursa Major that was visible in the images, we were able



Figure 23. An unprocessed image from the original data. The first several seconds of the video include a UT timestamp. Ursa Major appears at the top of the image.

to estimate that the PAI was facing south of zenith, spanning elevation angles between 66.8° and 90° . Figure 23 is an example of one of the raw images. This is a white-light image and the auroral features are faint, but visible to the naked eye, however we have no additional spectral information. To reduce data size and improve image quality, we averaged every 10 frames to produce a 3 fps video, which we then analyzed. Our analysis of this data is a continuation of preliminary work by A. Jaynes (2013). It is also worth noting that this data was taken during a targeted and short-lived campaign, where data was collected for only a select period each night.

4.3 Case Study

To better describe this phenomenon we first investigate a single representative event (number 28 from the list of 32 events as identified in Figure 26). Figure 24 shows three images taken at different times during this event. We changed the contrast and color map of the images to see the event better. In the first image the aurora begins as a diffuse background. In the second image a diffuse auroral arc appears in the form of a brighter stripe in the lower third of the frame. By the

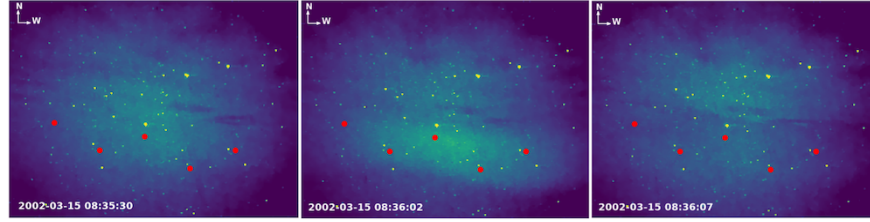


Figure 24. Images across a characteristic eraser event. From left to right the images are before the event, during the event brightening, and during the event eraser. The red dots indicate the 5 pixels we used to represent the event.

third image, the stripe has disappeared and the background aurora is darker than the first image, as if someone has taken an eraser to it. Small black auroral forms can also be seen in each frame, although we do not explore those features in this chapter.

To represent the event, we picked 5 pixels from across the image frame. These are represented by the red dots in Figure 24. By taking the median of a 5x5 pixel block centered on each of those, and then the average of the 5 block values, we were able to estimate the brightness of the event at each time step. Figure 25 shows this brightness plotted versus time after applying a 1.5 second smoothing window. In addition, Figure 25 is color coded to indicate what we refer to as the 4 phases of an auroral eraser event. The initial phase (solid green) is the period before the event with a uniform diffuse aurora background. The brightening phase (dotted red) comes next and is characterized by an east-west stripe of aurora that rapidly brightens. Shortly after, the brighter section disappears in the eraser phase (solid black), taking the diffuse background with it. Finally, in the recovery phase (dotted purple) the pixels return to their original brightness over several tens of seconds. For this event, the recovery time is 32 seconds. The details of how this is calculated are in the next section.

4.4 Analysis

We found that the best way to identify an auroral eraser event was in a keogram. This is a type of figure that is often used to visualize the evolution of aurora. A keogram is constructed by taking a north-south line of pixels from each image and aligning all of them chronologically. For

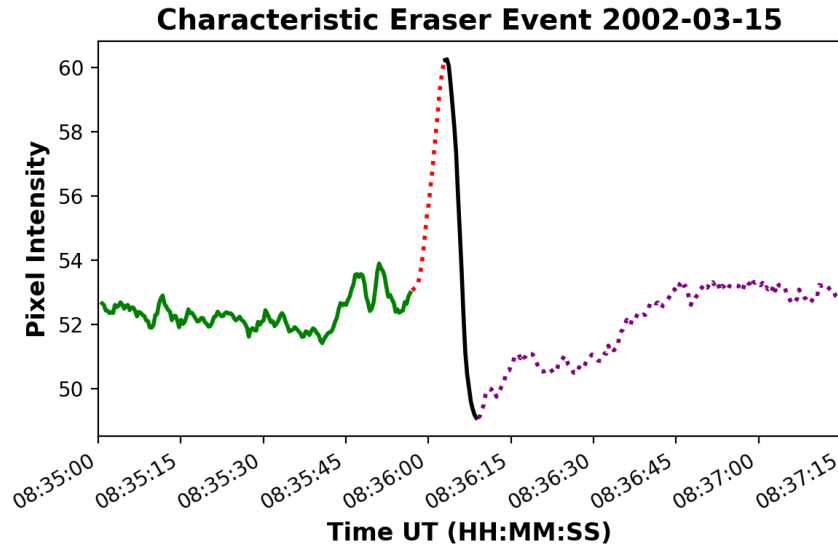


Figure 25. The averaged intensity of a characteristic eraser event. The event is color coded by phase: initial (solid green), brightening (dotted red), eraser (solid black), recovery (dotted purple).

each of our keogram columns we calculated a median column from the 21 center pixel columns of the corresponding image. We did this to highlight the diffuse auroral features over the much brighter stars, which appear as bright horizontal lines throughout the keogram. Initially, we split the 2 hours of data into approximately 20 minute sections, and made a keogram for each. We found 32 auroral eraser events in the last 2 sections and no events preceding this. The keogram shown in Figure 26 spans a time range that contains all 32 events. These are labeled in the figure and are identifiable by a bright vertical strip, followed by a darker section. An observant reader might also notice darker patches scattered across the keogram in addition to the auroral erasers. These are black aurora, which we mention, but did not study further. Finally, the bright horizontal streaks are stars that happened to fall within the center columns of the base images.

Using the keogram to identify all of the events, we then created an intensity versus time plot, like Figure 25, for each auroral eraser. Looking at these plots, it was clear that some events didn't have a full recovery phase, often being disrupted by a second event (see Figure 30 as an example). From the 32 events, we were able to visually identify 22 that returned to the original diffuse auroral brightness without being interrupted by a second event. Since we were interested

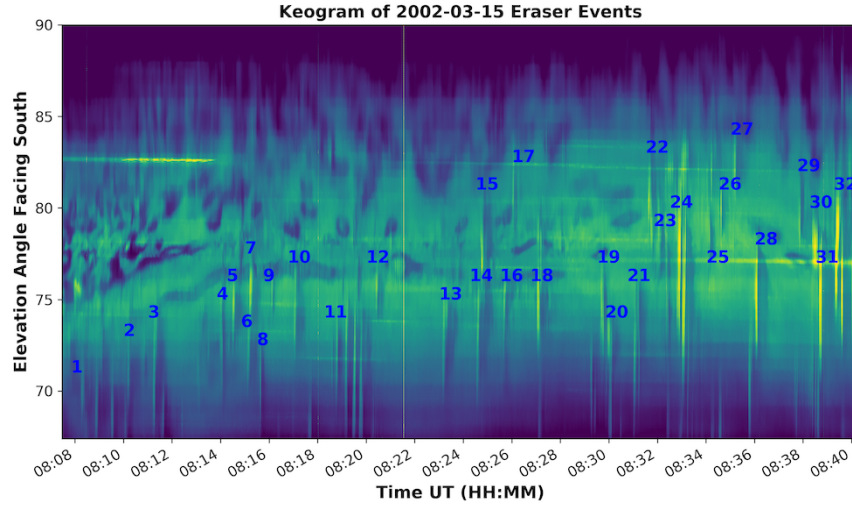


Figure 26. A keogram containing all of the auroral eraser events we identified. We increased the contrast and used the Viridis color map to see the events better.

in characterizing the recovery time, we limited our data set to these events. We then performed a superposed epoch analysis, shown in Figure 27. We set an epoch time halfway between the peak of the brightening phase and the trough of the eraser phase. We also normalized the pixel intensity by setting the average of the initial phase to zero. The time range associated with this was 100 to 30 frames or 43 to 10 seconds before the epoch. We could then determine the time from trough of the eraser phase to when the brightness returned to zero, we called this the recovery time. The average recovery time from this analysis was 20 seconds. However, the standard deviation was 13.17 seconds, highlighting that individual events can vary dramatically. This can be further seen in Figure 28, which is a histogram of the recovery times from the 22 events. The large peak for times less than 10 seconds is a result of events whose initial phases slowly increase in brightness instead of remaining constant. This causes the baseline average to be lower than other events.

Using the keogram we measured the approximate north-south extent of each eraser event, visually identifying the event edges. Widths range between 5 and 13 kilometers, with an average of 4.6 kilometers. This scale often shrinks as the eraser event fills in from the outsides during the recovery phase.

We were also interested in the magnetic conditions on March 15, 2002. To learn about these

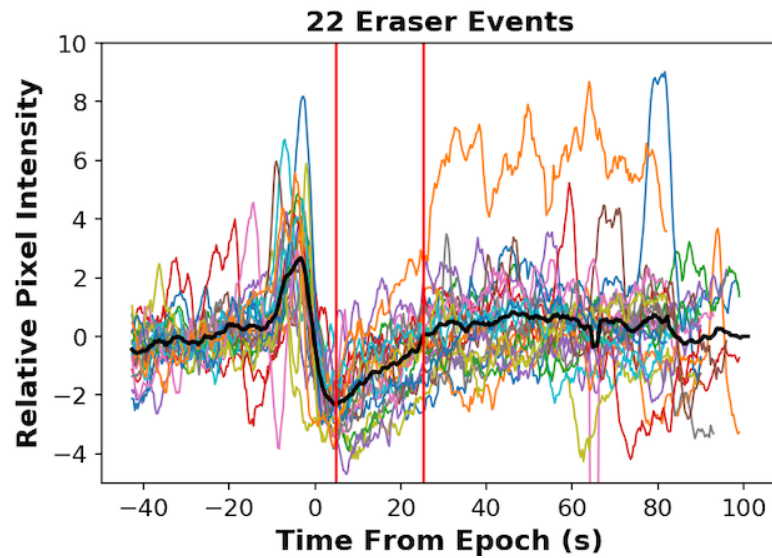


Figure 27. Epoch analysis for the 22 eraser events with a full recovery. The red lines indicate the start and stop of the average recovery period, which is 20 seconds. Some of the time series show periodic behavior.

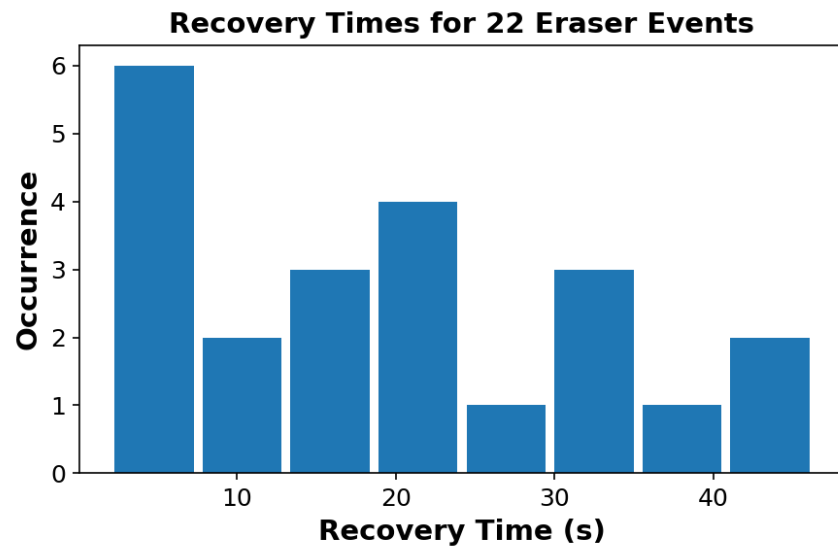


Figure 28. Histogram of the recovery times for the 22 eraser events with a full recovery. The recovery time is calculated as the time between the end of the eraser phase to when the brightness returns to the average of 43 seconds to 10 seconds before the brightening phase.

we looked at several different sources. The solar wind speed as extracted from NASA/GSFC's OMNI data set through OMNIWeb, was between 340 and 360 km/s. OMNI is a database of combined solar wind parameters from multiple spacecraft including WIND and ACE. B_z ranged between 0 and 6 nT, the K_p index was < 2 , and the Dst index was > -20 nT (King, 2005). In all, the solar wind and magnetic conditions were unremarkable and indicated quiet activity. The story was the same for ground-based magnetometers. SuperMAG is a database of over 300 magnetometers, each of which measures magnetic fields in 3 directions (Gjerloev, 2009, 2012). We looked at data from several stations during the night of March 15, 2002. Data from Churchill (FCC) and surrounding magnetometers (IQA, SKT) showed no major perturbations in any of the field directions. Magnetometers on the north-east coast of Greenland and on Svalbard (DNB, NAL) did show some activity in the form of small wave-like fluctuations. These are plotted in Figure 29. Unfortunately, the highest cadence option was 1 minute, so we were unable to see any higher frequency modulations. Finally, the Auroral Electrojet (AE) index, which is derived from the horizontal component of select magnetometers around the globe, indicated low magnetic activity with a value of < 90 nT.

4.5 Discussion

Other types of events showing atypical fluctuations in brightness of diffuse-like aurora have been published before (Yamamoto, 1988; Dahlgren, Lanchester, Ivchenko, & Whiter, 2017). Dahlgren, Lanchester, Ivchenko, and Whiter (2017) mentions observing a dip in brightness to below the average, during the off phase of pulsating aurora. While the events discussed here are similar, we believe that the differences are significant enough to provide additional scientific insight.

Watching video of the eraser events, the question arises, what type of aurora are these associated with? The background appears diffuse-like, but the eraser events are more structured. One possibility is that they are an atypical form of pulsating aurora. While typical pulsating aurora appears as patches of aurora that turn on and off with periods up to 20 seconds, which repeat for

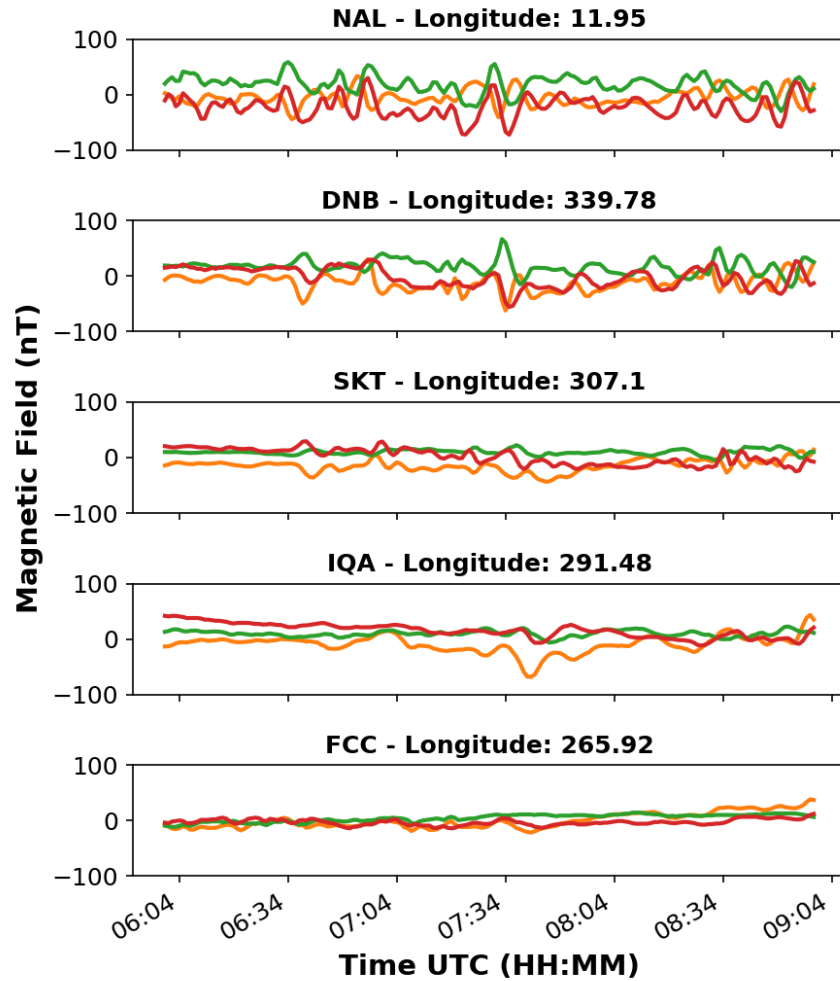


Figure 29. Five ground-based magnetometers during the night of March 15, 2002. The plots are arranged by eastward geographic longitude from bottom to top. The bottom three are located between Churchill and the west coast of Greenland. The top two are located on the east coast of Greenland and on Svalbard.

many periods, studies have observed other, less common behaviors. For instance, Johansen and Omholt (1966) classifies type A pulsating aurora as pulses with periods between 1 and 3 seconds that decrease in intensity with each pulse until they are no longer visible. This is usually no more than 5-8 pulses. Royrvik and Davis (1977) also specify that a pulsating aurora patch can undergo only a single pulse. In addition, dual-layer pulsating aurora could also be similar (Royrvik, 1976; T. S. Trondsen & Cogger, 1997). T. S. Trondsen and Cogger (1997) described it as a section of foreground diffuse aurora that turns off, revealing a background with structure in it. It is possible that these are auroral eraser events, but their camera FOV was significantly smaller (7.4° by 5.5°), so it is difficult to tell with certainty. Another possibility is that the eraser events are a type of structured diffuse-like aurora. Nightside structured diffuse-like aurora manifests as regular, parallel auroral stripes, brighter than the background according to Sergienko, Sandahl, Gustavsson, et al. (2008), who found that structured diffuse-like aurora is caused by precipitating electrons above 3-4 keV and linked these to whistler mode hiss waves. A future study to find more of these events and compare them with known types of aurora such as those in Royrvik and Davis (1977) and Fukuda, Kataoka, Miyoshi, et al. (2016) would be interesting. There are also many additional features in this data set that could be researched further such as the black aurora and non-erasing diffuse-like forms.

Without further data, we do not wish to speculate on what type of aurora the eraser events are linked to. However, we would like to note that, to our knowledge, reports of auroral behavior such as this are rare. That is intriguing, as the global and local geomagnetic data we investigated appears to show ordinary conditions that likely occur frequently. In addition, the 32 events we observed happened within a 2 hour period suggesting that when the conditions are right numerous eraser events can occur. Are eraser events such as these common during times of low global magnetic indices and have other observations just overlooked them due to the narrow field-of-view and high sensitivity required to see them, or are they rare? A more detailed search would be necessary to answer this question.

Without concurrent in situ spacecraft observations, we can only speculate on possible drivers

of these features. One possible cause could be modulated chorus waves interacting with a diffuse-like aurora population, possibly driven by ECH waves. As Ni, Thorne, Meredith, et al. (2011) showed, the scattering efficiencies are different between ECH and chorus waves for different pitch angles. Chorus waves scatter more efficiently over a wider pitch angle distribution than ECH waves. If, during an instance of ECH-driven diffuse aurora, the particles drifted through a region of modulated chorus waves, the effect might be to momentarily increase the electron flux, causing the brightening we observe. If the chorus waves were strong enough they could deplete electrons in the narrower ECH pitch angle scattering distribution, causing the eraser. If this were true, we would expect a second peak if the particles drifted through another region of chorus waves before the diffuse aurora had completely recovered. We see this behavior in several cases as Figure 30 shows.

Another explanation could be the relaxation oscillator model proposed by Davidson (1986) to explain the periodic behavior of pulsating aurora. This model is driven by an interaction between the loss cone and scattering waves. When electrons are injected into a closed field line, waves begin to grow and scatter some of these into the loss cone. As the loss cone fills, wave growth halts. Without waves to scatter more electrons, the loss cone empties to a level lower than it started with. This might explain the erasing behavior of an eraser event. In this cycle, more particles are lost than would be required to reestablish equilibrium. For the process to continue for multiple cycles, the source of electrons needs to be strong enough to fill the loss cone back to equilibrium.

These explanations are only speculative and we would need more detailed modeling and data to determine their feasibility.

4.6 Summary

- A diffuse auroral eraser event is characterized by an initial background of diffuse aurora, followed by the brightening of a more defined auroral stripe, which disappears and takes the background aurora with it. The background then refills back to the initial state at a slower rate. This recovery time can vary dramatically, but averages around 20 seconds.

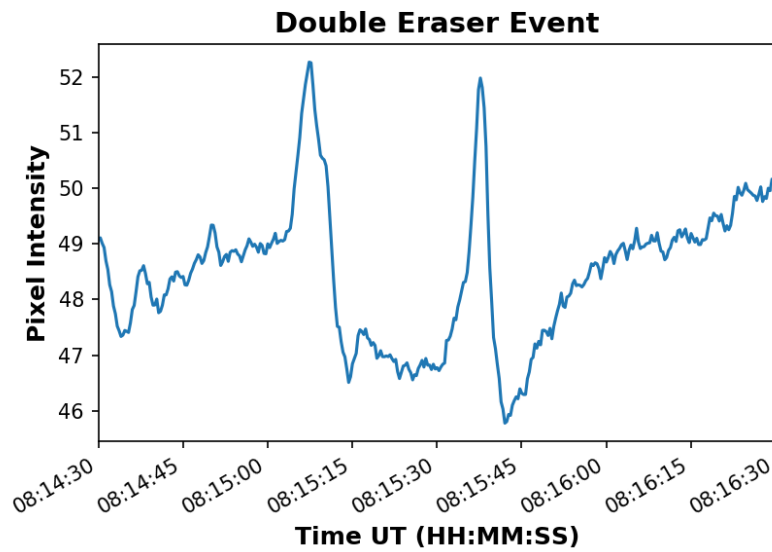


Figure 30. Event 6 begins as a normal eraser event, but before the diffuse background is able to fully refill, a second event (7) appears to occur. After this the background refills as normal.

- The eraser events we observed occurred within diffuse aurora and during times of low magnetic activity. In addition, they all occurred within 40 minutes of each other.
- From our knowledge there have been limited reports of events such as these, which raises the question: are these a common quiet time phenomenon that has been overlooked or are they rare?

CHAPTER 5: ANALYSIS AND VISUALIZATION METHODS

5.1 Energy Inversion

To solve the inverted problem of extracting a differential energy flux from electron densities, we used the process outlined in Semeter and Kamalabadi (2005). We assumed the pitch angle distribution of the incoming electrons was isotropic and used the universal energy dissipation function (Λ) given in the paper. We took our range-energy function from Barrett and Hays (1976) as

$$R = 4.7 \times 10^{-6} + 5.36 \times 10^{-5} K^{1.67} - 0.38 \times 10^{-7} K^{-0.7} \quad [\text{kg} \cdot \text{m}^{-2}]$$

where K is the electron energy in keV. Using these, we can construct a matrix A , where

$$A_{ij} = \frac{\Lambda\left(\frac{s(z_i)}{R(K_j)}\right) \rho(z_i) K_j \Delta K_j}{35.5 R(K_j)}$$

where $s(z_i) = \sec(\theta) \int_{z_0}^{\infty} \rho(z) dz$ is the mass distance traveled by an electron as a function of altitude. We assumed the dip angle of the magnetic field, $\theta \approx 0$. We calculated the neutral atmospheric density $\rho(z)$ using the NRLMSISE00 model and approximated $z \rightarrow \infty$ as $z = 1000$ km (Hedin, 1991).

The matrix A relates the ion production rate (q) and the differential number flux (ϕ) via

$$q_i = A_{ij} \frac{\phi_j}{\Delta K_j}$$

As Fang, Randall, Lummerzheim, et al. (2010) showed, using a range-energy function gives poor estimates of the ion production rate from electrons below 1 keV. However, the altitude range of the PFISR data means that there is very little, if any, contribution from these energies. Therefore, we assume that the range-energy function is a good enough estimate in this case.

Given that the inversion is done in terms of the ion production rate, we must convert our

electron density into an ion production rate. Once we have done this we can compare the model to reality and perform the iterative process involved in the inversion. Important atmospheric chemistry is encapsulated in the conversion of electron density measured by PFISR to an ion production rate. This is especially relevant below 85 km, where the chemistry of ion production becomes increasingly complex (Mitra, 1981). There are several ways of handling the chemistry. For our primary results we used the Glukhov-Pasko-Ina (GPI) model (Glukhov, Pasko, & Inan, 1992; Lehtinen & Inan, 2007). This uses the specific conditions as measured by PFISR, and modeled by the International Reference Ionosphere (IRI-2016) and NRLMSISE-00. From this, it outputs an ion production rate as a function of altitude. This is what the algorithm compares to the modeled ion production rate.

Previous work has shown that GPI performs well for the D-region (Marshall, Xu, Kero, et al., 2019). We set the values above 90 km to those of Gledhill (1986) for nighttime aurora. The Gledhill model is suitably close that of Vickrey, Vondrak, and Matthews (1982) above 90 km and the Vickrey model performs well in this region (Sivadas, Semeter, Nishimura, & Kero, 2017). While we could have used the Vickrey model, we believe the Gledhill model is slightly more accurate to this data. We refer to this adjusted model as GPI+. Given that the chemistry in this region of the atmosphere is not well known, we also performed our analysis with three additional models to provide context.

1. The best fit from Vickrey, Vondrak, and Matthews (1982) of multiple observations from several authors of α in the E-region.

$$\alpha(h) = 2.5 \times 10^{-12} e^{-h_{\text{km}}/51.2} \quad [\text{m}^3 \cdot \text{s}^{-1}]$$

To use this model we needed to extend it into the D-region, where it is not well defined.

2. The observations of Osepian, Kirkwood, Dalin, and Tereschenko (2009) during a solar proton event on January 17, 2005 at 9:50 UT. While these observations cover the D-region, they must be extended into the E-region. They also only cover a single event and that event is not

pulsating aurora.

3. The best fit of Gledhill (1986) for nighttime aurora covering the E-region and D-region.

$$\alpha(h) = 4.3 \times 10^{-6} e^{-2.42 \times 10^{-2} h_{\text{km}}} + 8.16 \times 10^{12} e^{-0.524 h_{\text{km}}} \quad [\text{cm}^3 \cdot \text{s}^{-1}]$$

Figure 31 shows how these three additional chemistry model compare with our analysis. They are represented by scatter points around each bar. These points can be considered as rough bounds on our results.

To determine the differential number flux (ϕ) we iterated using the maximum entropy method outlined in Semeter and Kamalabadi (2005). We monitored convergence through the χ^2 value between the modeled ion production rate and the rate calculated from the PFISR measurements. We stopped iterating when the step difference in the χ^2 values was less than 0.01. This usually took between 100 and 1000 steps. From the spectra that converged, we took those with a $1 \leq \chi^2_{\text{reduced}} < 3$ to be suitably good models. To calculate χ^2 it is important to have an accurate description of the variances (errors) in the PFISR data. The data products contain absolute errors associated with the measured number density. To propagate this to the ion production rate we calculated an intermediary recombination coefficient using the simple continuity equation

$$\frac{dn}{dt} = q - \alpha n^2$$

Assuming the temporal change of the electron density, as measured by PFISR, is small compared to the timescales we are studying, we can say that $q = \alpha n^2$, where α is the effective recombination coefficient. From our experience, this steady state assumption is good for pulsating aurora, at least when integrated over 1 minute like the PFISR data is. Previous work has also used it to convert between D-region electron densities and ion production rates (Kirkwood & Osepian, 1995;

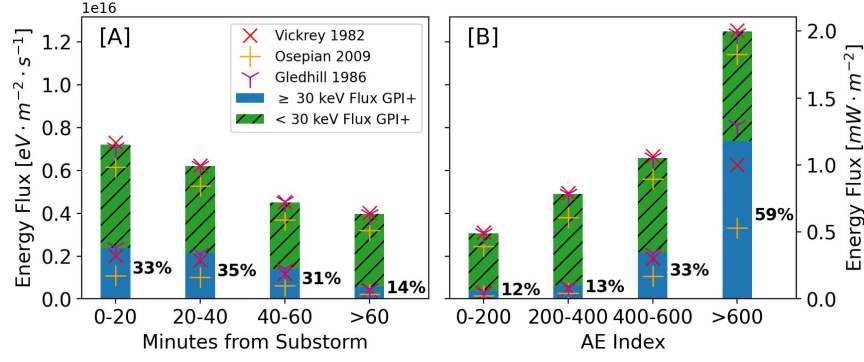


Figure 31. The high (≥ 30 keV) and low (< 30 keV) differential energy flux contributions to pulsating aurora events occurring in four temporal bins relative to substorm onset [A] and AE index [B]. We set the bar heights to the GPI+ model. The scatter points indicate the individual values from the three other chemistry models.

Osepian, Kirkwood, Dalin, & Tereschenko, 2009). Using this, our errors were then

$$\Delta q_{\text{chem}}(z) = 2\alpha(z)n(z)\Delta n(z)$$

To determine χ^2_{reduced} we need an estimate of the degrees of freedom in the model. We set this as the number of altitude bins where the errors were less than the data (fitted values) minus the number of energy bins (varied values). Figure 32 shows an example fitted electron density using this method. For this visualization, we converted back to electron density from the ion production rates using the same steady state assumption as above.

When performing the inversion, we found that the differential number flux of the highest energy bin was often over an order of magnitude larger than the next highest bin. We believe this is not physical and instead an artifact due to the initial electron density guess only needing to converge to the PFISR sensitivity ($\sim 10^9 \text{ m}^{-3}$) and not zero for lower altitudes. To mitigate this error, we only calculated our averages up to the second highest energy bin.

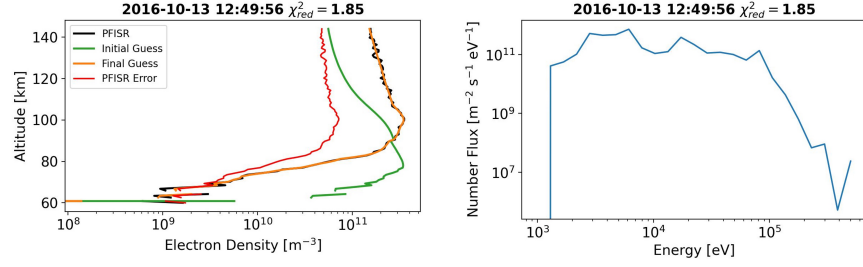


Figure 32. An example fitted electron density using the maximum entropy method along with the GPI+ chemistry model. The plot on the left shows the PFISR measured electron density (black) along with the associated error (red). The initial guess is shown in green and the final fit is shown in orange. The plot on the right is the differential number flux over the range of energies given to the model.

5.1.1 Poker Flat Incoherent Scatter Radar Data

Our inversion analysis in Chapter 2 uses PFISR data collected in three closely related modes named MSWinds23, MSWinds26, and MSWinds27. All three of these modes interleave three different pulse types optimized for the D-region, E-region, and F-region, respectively, with most of the available duty cycle dedicated to the D-region portion. The D-region portion uses 13-baud Barker codes with $10 \mu s$ baud, oversampled at $5 \mu s$, with a 2 ms interpulse period (IPP). The E-region portion uses 16-baud randomized alternating code with 30 s baud, and the F-region portion uses $480 \mu s$ uncoded long pulses. Both MSWinds23 and MSWinds26 send 256 consecutive Barker coded pulses in each of the four beam directions and then cycles through the complete set of 32 alternating codes and 32 long pulses on each of the four beam directions. Sending the Barker codes on consecutive pulses allows for the computation of pulse-to-pulse autocorrelation functions and spectra in the D-region, but it has the detrimental effect of introducing range-aliased returns from ranges at integer multiples of 300 km. MSWinds23 transmits the Barker codes and alternating codes on 449.3 MHz and the long pulses on 449.6 MHz. In MSWinds23 the dedicated noise samples on 449.3 MHz are taken by the alternating code channel and need to be rescaled according to the different filter bandwidth to be applied to the Barker code data. MSWinds26 improves this by transmitting the Barker codes on 449.3 MHz, alternating codes on 449.6 MHz, and long pulses

on 449.8 MHz, and incorporating dedicated noise samples on all three channels. MSWinds27 is identical to MSWinds26, except it changes the pulse repetition pattern for the Barker codes. Rather than transmitting 256 pulses on each of the four beams, each cycle MSWinds27 transmits 2048 consecutive pulses on the vertical beam and then 128 consecutive pulses on each of the other three beams. This gives MSWinds27 significantly better statistics on the vertical beam at the expense of reduced statistics on the other positions.

This inversion analysis uses electron density estimated from the received Barker code power and error estimates for that electron density determined from the number of pulses averaged and the signal-to-noise ratio. In addition to random errors, this electron density estimate is potentially subject to systematic bias if the subtracted noise is too small. PFISR has certain hardware issues that cause the noise to be slightly higher at short ranges than at long ranges. Furthermore, the D-region returns can be corrupted by range-aliased F-region returns. Both of these problems bias the lower D-region electron density estimates high. In order to compensate for this bias, we have assumed the true electron density between 55 and 60 km is always indistinguishable from zero. We estimate the bias by averaging the power between 55 and 60 km and subtracting it off from the power profiles before converting to electron density. This bias can be on the order of an electron density of 10^9 m^{-3} , which is a minor correction to the typical electron densities in pulsating aurora (above 10^{10} m^{-3}). Nonetheless, this bias correction is needed to prevent the inversions from incorrectly estimating tails of relativistic electrons in order to match the lowest altitude data.

After conducting our analysis using the inversion technique, we've since discovered a more accurate way of characterizing the high estimates of the electron density in the lower D-region. The responsible noise falls off between approximately 85 km to 110 km, thus we do not need a correction above 110 km. Our new correction is scaled by 1 below 85 km, 0 above 110 km, and by a linear reduction from 1 to 0 between 85 km and 110 km. Figure 33 shows how the noise scales in the vertical beam.

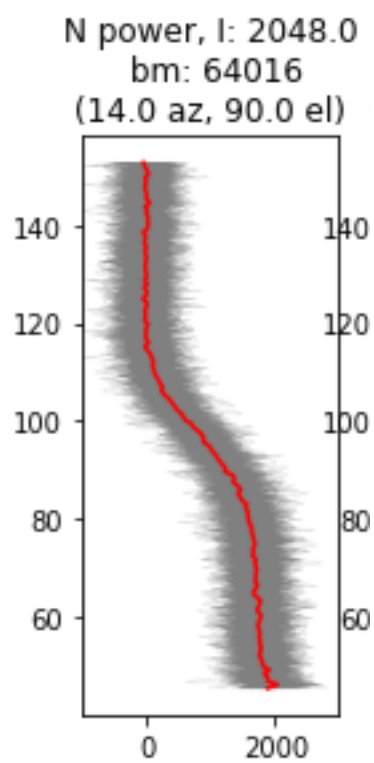


Figure 33. Hiss noise in the vertical PFISR beam measured as a function of beam range.

5.2 Machine Learning Identification

There is extraordinary potential in all-sky camera data of the aurora, but the data can be tricky to work with. The THEMIS ASI dataset contains thousands of nights from around 20 imagers totalling nearly 100 TB of data. To conduct a pulsating aurora study one must manually look through many images or keograms and determine which contain pulsating aurora. This is time consuming and limited when compared to the whole dataset. Image classification is one of the most well tested uses of machine learning. It would be natural then to extend this to ASI data and automate auroral classifications. Clausen and Nickisch (2018) did just that, training an algorithm on six different labels: arc, discrete, diffuse, cloudy, moon, and clear/no aurora. While they were able to predict approximately 82% of the image labels correctly in their testing data, they did not distinguish between diffuse and pulsating aurora. Kvammen, Wickstrøm, McKay, and Partamies (2020) did make that distinction with their machine learning auroral classification. They achieved precision and recall values of 0.92 and 0.89 respectively, but trained their model on a color all-sky imager near Kiruna, Sweden. We have trained a new model with the intent of extending machine learning techniques to pulsating aurora classification of the THEMIS ASIs. As of writing this thesis, we are still working on this project and so are still lacking specifics as to how well the model works.

5.2.1 Data Processing

Before working with the THEMIS images we process them from their raw state. The raw images are stored as 256 x 256 arrays with 16-bit depth. Each camera is different in its orientation and location. This information is contained in a separate calibration file with pixel mapping to latitude/longitude and elevation and azimuthal angle. Occasionally, a camera will get moved, resulting in a new calibration file. We use these calibration files to mask the lowest 15° of the field-of-view. This helps eliminate contamination by car headlights, building lights, building exhaust, etc. The aurora near the edge of the field-of-view is difficult to identify, so we do not lose much useful information by cropping in this way.

The machine learning methods that we use require 8-bit image input, so we must downscale the original images. This is a tricky process that we have to do carefully so as to not lose valuable information. Our current method, which we've found preserves auroral information well without over or under saturating, uses the Contrast Limited Adaptive Histogram Equalization (CLAHE) technique baked into the OpenCV Python package. Compare Figure 35 to 34 to see an example of this technique in action. Many imager teams, including THEMIS, store the raw data in the format of many individual files. We've employed a different technique to store the images that we believe is more convenient for transporting and working with the semi-processed data. Initially we read in the raw images, for an entire day, into an array. At the same time we find and read in the corresponding calibration file for the imager and date. We then downscale the image array from 16-bit to 8-bit, as described above. Finally, we write the images, calibration information, and timestamps for each image to an HDF5 file. Each HDF5 file is between a few hundred MB to a GB in size and contains all the information a researcher would need to analyze and visualize the images from that particular day.

5.2.2 Training Data

As a training dataset for our model we classified by eye approximately 23,000 images from 16 THEMIS cameras and 12 days and approximately 35,000 images from the Poker Flat ASI over 58 days. We split our classifications into four different categories:

- Pulsating aurora (including all classifications from Grono and Donovan (2018))
- Other aurora (including diffuse, discrete, and substorm)
- No aurora (includes periods where the sky is visible, but there is no visible aurora)
- Bad viewing conditions (conditions that obscure the sky such as clouds, bad optics, sunrise and sunset, etc.)

5.2.3 Model

To design our machine learning model we used a modified Convolutional Neural Network (CNN). A normal CNN model classifies images individually. Our modification allows the model to be trained and classify images by taking a rolling average, similar to Rosebrock (2019). Pulsating aurora is a strongly temporal phenomenon and so we believe this technique will provide the most robust predictions. When classifying, the model will provide confidence values, totally 100%, for each of our categories. See Figures 34 and 35 as examples of classified frames. In these images we've used different processing techniques. Figure 34 is processed in a such a way that the image is over saturated, meaning that classification is challenging and the bad viewing condition label is accurate. Figure 35 uses our better CLAHE technique and allows us to see the pulsating aurora despite the poor conditions. The model is able to detect it as well and correctly classifies the frame.

Going forward we plan to run our model on the entire THEMIS ASI database. This will produce metadata for each image with the classification labels and their confidence levels. This metadata will be published for public viewing on the AuroraX platform (Shumko, Chaddock, Gallardo-Lacourt, et al., 2022).

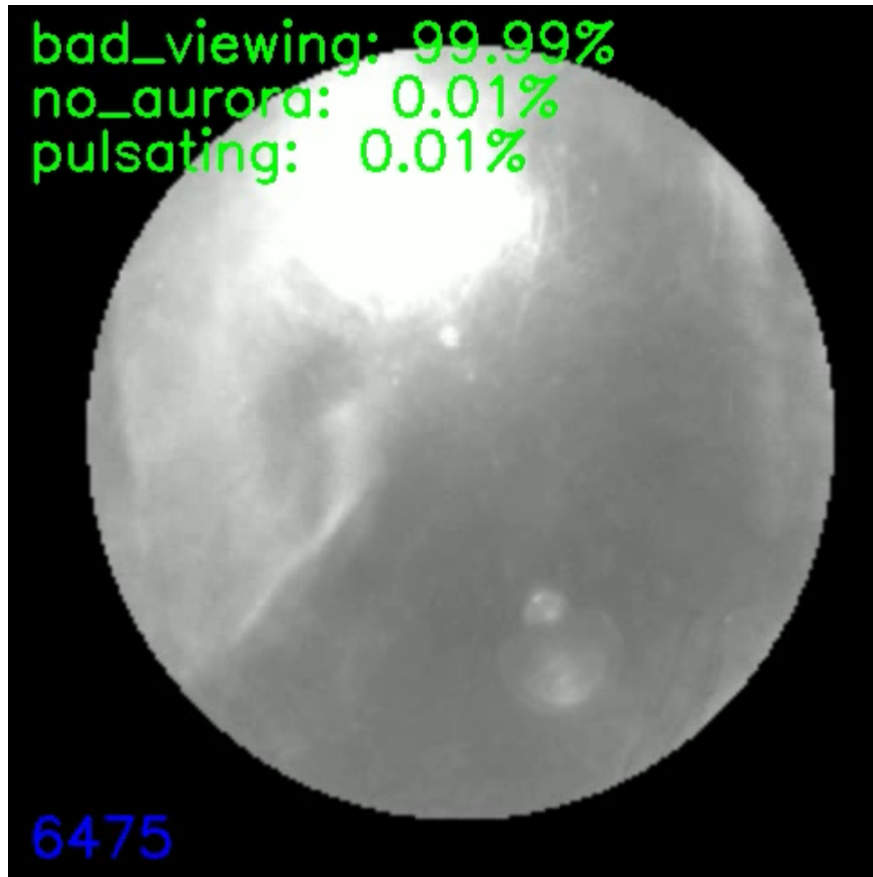


Figure 34. An image from one of the test of our machine learning model. The image here was classified with a scaling technique that doesn't perform as well in poor conditions as our CLAHE technique. In this image the moon is up and the optics are damaged in some way. The combined result is a very over saturated image and the model is unable to see the aurora, thus classifying it as a bad viewing condition. The image was taken with the Gillam, MB ASI on 2015-10-02

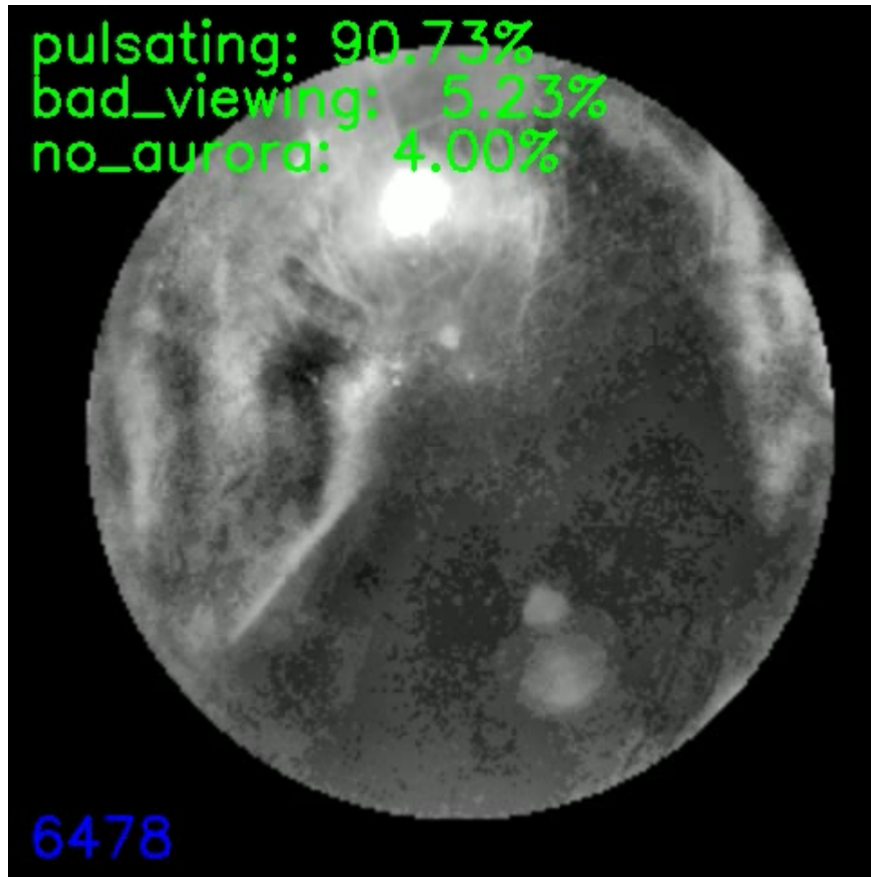


Figure 35. An image from one of the test of our machine learning model. The image here was classified with our CLAHE technique. In this image the moon is up and the optics are damaged in some way. However, our processing technique is able to enhance the auroral features and allows us to see pulsating aurora. The machine learning model is also able to detect them based on the classification confidence. The image was taken with the Gillam, MB ASI on 2015-10-02

CHAPTER 6: CONCLUSIONS

Throughout this thesis we have investigated the properties of diffuse-like, but dynamic aurora. Primarily we looked at an important subset of diffuse-like aurora called pulsating aurora. However, we also examined a similar, but yet intriguingly different, type that we coined the diffuse auroral eraser.

Diffuse-like and dynamic aurora aren't as stunning or photogenic as a classic discrete arc or substorm aurora, but are just as important to study. For instance, as Verronen, Kero, Partamies, et al. (2021) showed, pulsating aurora could be responsible for up to an 8% reduction in ozone during certain instances. However, many investigations of auroral energy deposition into the atmosphere, such as Newell, Sotirelis, and Wing (2009), leave out pulsating aurora energies. In addition, large missions like the upcoming Geospace Dynamics Constellation (GDC), often leave out > 30 keV measurements in their auroral electron instrument design Gershman (2022). We hope the work presented here will provide evidence and incentive to include pulsating aurora and their associated energies in future auroral studies.

6.1 Pulsating Aurora Energy

In Chapter 2 we examined the statistics of pulsating aurora energy. Rocket missions have found that the energy content of certain pulsating aurora instances are more energetic than other auroral types (Sandahl, Eliasson, & Lundin, 1980). Optical measurements using triangulation and wavelength ratios showed that pulsating aurora occur at a lower altitude (Whalen, Miller, & McDiarmid, 1971; Brown, Davis, Hallinan, & Stenbaek-Nielsen, 1976). This lower altitude also shows up in incoherent scatter radar measurements (Jones, Lessard, Fernandes, et al., 2009; Tesema, Partamies, Nesse Tyssøy, & McKay, 2020). However, these past studies have either been proxies, such as altitude, for energy, or case studies. Thus there was a need for a statistical study of pulsating aurora energies. In Chapter 2 we conducted a statistical study that confirmed the energetic nature of pulsating aurora. We also quantified the energy content and found that it varies

predictably related to both AE index and substorm onset. Close in time to substorm onsets, and for high AE, a majority of the pulsating aurora energy flux can be carried by > 30 keV electrons. Our results compare well to the recent study of Tesema, Partamies, Tyssøy, et al. (2020), which looked at the statistical properties of pulsating aurora using satellite measurements. Combined, these results show that the energy of pulsating aurora can be an order of magnitude larger than discrete aurora. Therefore understanding this aurora at such a quantitative level is important. Our results have already been used to help successfully launch the LAMP rocket mission. Going forward, they will guide models and studies aiming to quantify the impact of energetic pulsating aurora on processes like ozone depletion.

6.2 Pulsating Aurora Source Mechanism

In Chapter 3 we followed a lead discovered in Chapter 2 that helped us better understand the source mechanism for pulsating aurora. Statistically connecting pulsating aurora on the ground with wave activity in the magnetosphere is challenging. To make a direct measurement, a satellite must pass through a magnetic field line that maps to a pixel on an all-sky camera that is observing pulsating aurora. Several studies have successfully done this and shown that lower-band chorus waves can drive pulsating aurora (Nishimura, Bortnik, Li, et al., 2010; Kasahara, Miyoshi, Yokota, et al., 2018). However, because of the inherent difficulties, the number of cases in these studies is small. One possible way of making a broader connection is through timescales. In Chapter 2 we found that > 30 keV electrons decay after substorms with a timescale of 0.85 hr. In Chapter 3, following up on Meredith, Horne, Johnstone, and Anderson (2000), we studied the statistical decay timescale of lower-band chorus after substorms. We found that these decay times, in the MLT regions that pulsating aurora is most common, were very similar at 0.75 hr. This provides a strong statistical link connecting pulsating aurora to lower-band chorus waves and helps complete the general picture of how pulsating aurora forms.

6.3 Diffuse Auroral Eraser

Finally, in Chapter 4 we looked at a similar, but separate, type of diffuse-like aurora. We called this the diffuse auroral eraser and it appears to be a special case of different diffuse-like auroral types influencing each other. We were able to find 32 of these events in 2 hours of video taken from Churchill, MB, Canada in 2002. Using those, we were able to understand what a typical event might look like. During a diffuse auroral eraser a diffuse arc will appear over top of background aurora, brighten, then rapidly disappear. Once gone, the background aurora, in the region where the arc had been, is darker than before, as if someone has taken an eraser to it. Over the course of approximately 20 seconds, the background aurora returns to the original brightness. Interactions like this could provide a unique perspective on magnetospheric processes. While we didn't have enough data to determine the cause of this phenomena, we hope that our report will inspire future studies into the cause and impacts of diffuse-like, but dynamic aurora.

REFERENCES

- Akasofu, S.-I. (1964). The development of the auroral substorm. *Planetary and Space Science*, 12(4), 273–282. [https://doi.org/10.1016/0032-0633\(64\)90151-5](https://doi.org/10.1016/0032-0633(64)90151-5)
- Akasofu, S.-I. (1966). The auroral oval, the auroral substorm, and their relations with the internal structure of the magnetosphere. *Planetary and Space Science*, 14(7), 587–595. [https://doi.org/10.1016/0032-0633\(66\)90043-2](https://doi.org/10.1016/0032-0633(66)90043-2)
- Anderson, K. A., & Milton, D. W. (1964). Balloon observations of x rays in the auroral zone: 3. high time resolution studies. *Journal of Geophysical Research*, 69(21), 4457–4479. <https://doi.org/10.1029/JZ069i021p04457>
- Aryan, H., Bortnik, J., Sibeck, D. G., & Hospodarsky, G. (2022). Global map of chorus wave sizes in the inner magnetosphere. *Journal of Geophysical Research: Space Physics*, 127(3). <https://doi.org/10.1029/2021JA029768>
- Baker, D. N., Kanekal, S. G., Hoxie, V. C., Henderson, M. G., Li, X., Spence, H. E., Elkington, S. R., Friedel, R. H. W., Goldstein, J., Hudson, M. K., Reeves, G. D., Thorne, R. M., Kletzing, C. A., & Claudepierre, S. G. (2013). A long-lived relativistic electron storage ring embedded in earth's outer van allen belt. *Science*, 340(6129), 186–190. <https://doi.org/10.1126/science.1233518>
- Barrett, J. L., & Hays, P. B. (1976). Spatial distribution of energy deposited in nitrogen by electrons. *The Journal of Chemical Physics*, 64(2), 743–750. <https://doi.org/10.1063/1.432221>
- Bland, E., Tesema, F., & Partamies, N. (2021). D-region impact area of energetic electron precipitation during pulsating aurora. *Annales Geophysicae*, 39(1), 135–149. <https://doi.org/10.5194/angeo-39-135-2021>
- Bland, E. C., Partamies, N., Heino, E., Yukimatu, A. S., & Miyaoka, H. (2019). Energetic electron precipitation occurrence rates determined using the syowa east SuperDARN radar. *Journal of Geophysical Research: Space Physics*, 124(7), 6253–6265. <https://doi.org/10.1029/2018JA026437>

- Borkin, M., Gajos, K., Peters, A., Mitsouras, D., Melchionna, S., Rybicki, F., Feldman, C., & Pfister, H. (2011). Evaluation of artery visualizations for heart disease diagnosis. *IEEE Transactions on Visualization and Computer Graphics*, 17(12), 2479–2488. <https://doi.org/10.1109/TVCG.2011.192>
- Borland, D., & Taylor, R. M. (2007). Rainbow color map (still) considered harmful. *IEEE Computer Graphics and Applications*, 27(2), 14–17. <https://doi.org/10.1109/MCG.2007.323435>
- Borovsky, J. E., & Partamies, N. (2022). What produces and what controls the spatial-temporal structuring of the magnetospheric chorus waves that create the pulsating aurora: An unsolved problem in need of new measurements. *Frontiers in Astronomy and Space Sciences*, 9, 1059039. <https://doi.org/10.3389/fspas.2022.1059039>
- Bortnik, J., Inan, U. S., & Bell, T. F. (2006). Landau damping and resultant unidirectional propagation of chorus waves. *Geophysical Research Letters*, 33(3), L03102. <https://doi.org/10.1029/2005GL024553>
- Boyd, A. J., Reeves, G. D., Spence, H. E., Funsten, H. O., Larsen, B. A., Skoug, R. M., Blake, J. B., Fennell, J. F., Claudepierre, S. G., Baker, D. N., Kanekal, S. G., & Jaynes, A. N. (2019). RBSP-ECT combined spin-averaged electron flux data product. *Journal of Geophysical Research: Space Physics*, 124(11), 9124–9136. <https://doi.org/10.1029/2019JA026733>
- Brice, N. (1964). Fundamentals of very low frequency emission generation mechanisms. *Journal of Geophysical Research*, 69(21), 4515–4522. <https://doi.org/10.1029/JZ069i021p04515>
- Brown, N. B., Davis, T. N., Hallinan, T. J., & Stenbaek-Nielsen, H. C. (1976). Altitude of pulsating aurora determined by a new instrumental technique. *Geophysical Research Letters*, 3(7), 403–404. <https://doi.org/10.1029/GL003i007p00403>
- Burtis, W., & Helliwell, R. (1976). Magnetospheric chorus: Occurrence patterns and normalized frequency. *Planetary and Space Science*, 24(11), 1007–1024. [https://doi.org/10.1016/0032-0633\(76\)90119-7](https://doi.org/10.1016/0032-0633(76)90119-7)

- Chapman, S. (1962). The aurora. *Leaflet of the Astronomical Society of the Pacific*, 8(394), 343. <https://articles.adsabs.harvard.edu/full/1962ASPL....8..343C>
- Chepuri, S. N. F., Jaynes, A. N., Turner, D. L., Gabrielse, C., Baker, D. N., Mauk, B. H., Cohen, I. J., Leonard, T., Blake, J. B., & Fennell, J. F. (2023). A comparison of energetic particle energization observations MMS at and injections at van allen probes. *Frontiers in Astronomy and Space Sciences*, 9, 1033546. <https://doi.org/10.3389/fspas.2022.1033546>
- Chu, X., McPherron, R. L., Hsu, T.-S., & Angelopoulos, V. (2015). Solar cycle dependence of sub-storm occurrence and duration: Implications for onset. *Journal of Geophysical Research: Space Physics*, 120(4), 2808–2818. <https://doi.org/10.1002/2015JA021104>
- Clausen, L. B. N., & Nickisch, H. (2018). Automatic classification of auroral images from the oslo auroral THEMIS (OATH) data set using machine learning. *Journal of Geophysical Research: Space Physics*, 123(7), 5640–5647. <https://doi.org/10.1029/2018JA025274>
- Crameri, F. (2018). Geodynamic diagnostics, scientific visualisation and StagLab 3.0. *Geoscientific Model Development*, 11(6), 2541–2562. <https://doi.org/10.5194/gmd-11-2541-2018>
- Crameri, F. (2021, September 12). *Scientific colour maps* (Version 7.0.1) [Language: en]. Zenodo. <https://doi.org/10.5281/ZENODO.1243862>
- Crameri, F., Shephard, G. E., & Heron, P. J. (2020). The misuse of colour in science communication. *Nature Communications*, 11(1), 5444. <https://doi.org/10.1038/s41467-020-19160-7>
- Cresswell, G. R., & Davis, T. N. (1966). Observations on pulsating auroras. *Journal of Geophysical Research*, 71(13), 3155–3163. <https://doi.org/10.1029/JZ071i013p03155>
- Dahlgren, H., Lanchester, B. S., Ivchenko, N., & Whiter, D. K. (2017). Variations in energy, flux, and brightness of pulsating aurora measured at high time resolution. *Annales Geophysicae*, 35(3), 493–503. <https://doi.org/10.5194/angeo-35-493-2017>
- Davidson, G. T. (1986). Pitch-angle diffusion in morningside aurorae: 2. the formation of repetitive auroral pulsations. *Journal of Geophysical Research*, 91, 4429. <https://doi.org/10.1029/JA091iA04p04429>

- Davis, T. N. (1980, January 23). *Names and definition of the aurora* | *geophysical institute*. Retrieved February 17, 2023, from <https://www.gi.alaska.edu/alaska-science-forum/names-and-definition-aurora>
- Davis, T. (1978). Observed characteristics of auroral forms. *Space Science Reviews*, 22(1). <https://doi.org/10.1007/BF00215814>
- DeForest, S. E., & McIlwain, C. E. (1971). Plasma clouds in the magnetosphere. *Journal of Geophysical Research*, 76(16), 3587–3611. <https://doi.org/10.1029/ja076i016p03587>
- Dry, S. (2018). Weather forecasts should get over the rainbow. *Wall Street Journal*.
- Dungey, J. (1963). Loss of van allen electrons due to whistlers. *Planetary and Space Science*, 11(6), 591–595. [https://doi.org/10.1016/0032-0633\(63\)90166-1](https://doi.org/10.1016/0032-0633(63)90166-1)
- Fang, X., Randall, C. E., Lummerzheim, D., Wang, W., Lu, G., Solomon, S. C., & Frahm, R. A. (2010). Parameterization of monoenergetic electron impact ionization. *Geophysical Research Letters*, 37(22), n/a–n/a. <https://doi.org/10.1029/2010GL045406>
- Feldstein, Y. I., & Galperin, Y. I. (1985). The auroral luminosity structure in the high-latitude upper atmosphere: Its dynamics and relationship to the large-scale structure of the earth's magnetosphere. *Reviews of Geophysics*, 23(3), 217. <https://doi.org/10.1029/RG023i003p00217>
- Forsyth, C., Rae, I. J., Coxon, J. C., Freeman, M. P., Jackman, C. M., Gjerloev, J., & Fazakerley, A. N. (2015). A new technique for determining substorm onsets and phases from indices of the electrojet (SOPHIE). *Journal of Geophysical Research: Space Physics*, 120(12), 10,592–10,606. <https://doi.org/10.1002/2015JA021343>
- Fredricks, R. W., & Scarf, F. L. (1973). Recent studies of magnetospheric electric field emissions above the electron gyrofrequency. *Journal of Geophysical Research*, 78(1), 310–314. <https://doi.org/10.1029/JA078i001p00310>
- Fritz, B. A., Lessard, M. R., Blandin, M. J., & Fernandes, P. A. (2015). Structure of black aurora associated with pulsating aurora. *Journal of Geophysical Research: Space Physics*, 120(11), 10096–10106. <https://doi.org/10.1002/2015JA021397>

- Fukuda, Y., Kataoka, R., Miyoshi, Y., Katoh, Y., Nishiyama, T., Shiokawa, K., Ebihara, Y., Hampton, D., & Iwagami, N. (2016). Quasi-periodic rapid motion of pulsating auroras. *Polar Science*, 10(3), 183–191. <https://doi.org/10.1016/j.polar.2016.03.005>
- Gabrielse, C., Angelopoulos, V., Runov, A., & Turner, D. L. (2014). Statistical characteristics of particle injections throughout the equatorial magnetotail. *Journal of Geophysical Research: Space Physics*, 119(4), 2512–2535. <https://doi.org/10.1002/2013JA019638>
- Gallardo-Lacourt, B., Frey, H. U., & Martinis, C. (2021). Proton aurora and optical emissions in the subauroral region. *Space Science Reviews*, 217(1), 10. <https://doi.org/10.1007/s11214-020-00776-6>
- Gauss, C.-F. (1832). The intensity of the earth's magnetic force reduced to absolute measurement. <http://21stcenturysciencetech.com/translations/gaussMagnetic.pdf>
- Gershman, D. J. (2022, December 13). *The comprehensive auroral precipitation experiment for NASA's geospace dynamics constellation* (Poster) [AGU Fall Meeting] [Poster]. Retrieved December 13, 2022, from <https://agu.confex.com/agu/fm22/meetingapp.cgi/Paper/1068032>
- Gillies, D. M., Knudsen, D., Spanswick, E., Donovan, E., Burchill, J., & Patrick, M. (2015). Swarm observations of field-aligned currents associated with pulsating auroral patches. *Journal of Geophysical Research: Space Physics*, 120(11), 9484–9499. <https://doi.org/10.1002/2015JA021416>
- Gjerloev, J. W. (2009). A global ground-based magnetometer initiative. *Eos, Transactions American Geophysical Union*, 90(27), 230. <https://doi.org/10.1029/2009EO270002>
- Gjerloev, J. W. (2012). The SuperMAG data processing technique. *Journal of Geophysical Research: Space Physics*, 117, n/a–n/a. <https://doi.org/10.1029/2012JA017683>
- Gledhill, J. A. (1986). The effective recombination coefficient of electrons in the ionosphere between 50 and 150 km. *Radio Science*, 21(3), 399–408. <https://doi.org/10.1029/RS021i003p00399>

- Glukhov, V. S., Pasko, V. P., & Inan, U. S. (1992). Relaxation of transient lower ionospheric disturbances caused by lightning-whistler-induced electron precipitation bursts. *Journal of Geophysical Research*, 97, 16971. <https://doi.org/10.1029/92JA01596>
- Griffiths, D. J. (2013). *Introduction to electrodynamics* (Fourth edition). Pearson.
- Grono, E., & Donovan, E. (2018). Differentiating diffuse auroras based on phenomenology. *Annales Geophysicae*, 36(3), 891–898. <https://doi.org/10.5194/angeo-36-891-2018>
- Grono, E., & Donovan, E. (2020). Surveying pulsating auroras. *Annales Geophysicae*, 38(1), 1–8. <https://doi.org/10.5194/angeo-38-1-2020>
- Gurnett, D. A., Anderson, R. R., Tsurutani, B. T., Smith, E. J., Paschmann, G., Haerendel, G., Bame, S. J., & Russell, C. T. (1979). Plasma wave turbulence at the magnetopause: Observations from ISEE 1 and 2. *Journal of Geophysical Research*, 84, 7043. <https://doi.org/10.1029/JA084iA12p07043>
- Hartley, D. P., Christopher, I. W., Kletzing, C. A., Kurth, W. S., Santolik, O., Kolmasova, I., Wygant, J. R., & Bonnell, J. W. (2022). Quantifying the sheath impedance of the electric double probe instrument on the van allen probes. *Journal of Geophysical Research: Space Physics*, 127(5). <https://doi.org/10.1029/2022JA030369>
- Hartley, D. P., Kletzing, C. A., Chen, L., Horne, R. B., & Santolík, O. (2019). Van allen probes observations of chorus wave vector orientations: Implications for the chorus-to-hiss mechanism. *Geophysical Research Letters*, 46(5), 2337–2346. <https://doi.org/10.1029/2019GL082111>
- Hedin, A. E. (1991). Extension of the MSIS thermosphere model into the middle and lower atmosphere. *Journal of Geophysical Research: Space Physics*, 96, 1159–1172. <https://doi.org/10.1029/90JA02125>
- Horne, R. B. (2003). Diffuse auroral electron scattering by electron cyclotron harmonic and whistler mode waves during an isolated substorm. *Journal of Geophysical Research*, 108, 1290. <https://doi.org/10.1029/2002JA009736>
- Horne, R. B., & Thorne, R. M. (2003). Relativistic electron acceleration and precipitation during resonant interactions with whistler-mode chorus: RELATIVISTIC ELECTRON AC-

- CELERATION. *Geophysical Research Letters*, 30(10), n/a–n/a. <https://doi.org/10.1029/2003GL016973>
- Hosokawa, K., Miyoshi, Y., Ozaki, M., Oyama, S.-I., Ogawa, Y., Kurita, S., Kasahara, Y., Kasaba, Y., Yagitani, S., Matsuda, S., Tsuchiya, F., Kumamoto, A., Kataoka, R., Shiokawa, K., Raita, T., Turunen, E., Takashima, T., Shinohara, I., & Fujii, R. (2020). Multiple time-scale beats in aurora: Precise orchestration via magnetospheric chorus waves. *Scientific Reports*, 10(1), 3380. <https://doi.org/10.1038/s41598-020-59642-8>
- Hosokawa, K., & Ogawa, Y. (2015). Ionospheric variation during pulsating aurora. *Journal of Geophysical Research: Space Physics*, 120(7), 5943–5957. <https://doi.org/10.1002/2015JA021401>
- Hotea, M. D., & Fritz, H. (2017, November 24). *The threads of the aurora and isochasms* [ETHeritage]. Retrieved February 17, 2023, from <https://etheritage.ethz.ch/2017/11/24/the-threads-of-the-aurora-and-isochasms/?lang=en>
- Hua, M., Bortnik, J., Kellerman, A. C., Camporeale, E., & Ma, Q. (2023). Ensemble modeling of radiation belt electron acceleration by chorus waves: Dependence on key input parameters. *Space Weather*. <https://doi.org/10.1029/2022SW003234>
- Hua, M., Bortnik, J., & Ma, Q. (2022). Upper limit of outer radiation belt electron acceleration driven by whistler-mode chorus waves. *Geophysical Research Letters*, 49(15). <https://doi.org/10.1029/2022GL099618>
- Hua, M., Bortnik, J., Spence, H. E., & Reeves, G. D. (2023). Testing the key processes that accelerate outer radiation belt relativistic electrons during geomagnetic storms. *Frontiers in Astronomy and Space Sciences*, 10, 1168636. <https://doi.org/10.3389/fspas.2023.1168636>
- Isted, G. A., & Millington, G. (1957). The ‘dawn chorus’ in radio observations. *Nature*, 180(4588), 716–716. <https://doi.org/10.1038/180716a0>
- Jaynes, A. N., Lessard, M. R., Rodriguez, J. V., Donovan, E., Loto’aniu, T. M., & Rychert, K. (2013). Pulsating auroral electron flux modulations in the equatorial magnetosphere. *Jour-*

- Journal of Geophysical Research: Space Physics*, 118(8), 4884–4894. <https://doi.org/10.1002/jgra.50434>
- Jaynes, A. N., Lessard, M. R., Takahashi, K., Ali, A. F., Malaspina, D. M., Michell, R. G., Span-
swick, E. L., Baker, D. N., Blake, J. B., Cully, C., Donovan, E. F., Kletzing, C. A., Reeves,
G. D., Samara, M., Spence, H. E., & Wygant, J. R. (2015). Correlated pc4–5 ULF waves,
whistler-mode chorus, and pulsating aurora observed by the van allen probes and ground-
based systems. *Journal of Geophysical Research: Space Physics*, 120(10), 8749–8761.
<https://doi.org/10.1002/2015JA021380>
- Jaynes, A. (2013). *I-pulsating aurora: Source region & morphology* (Doctoral dissertation) [ISBN:
9781303418129]. University of New Hampshire. United States – New Hampshire. Re-
trieved November 15, 2022, from [https://www.proquest.com/docview/1436992455/
abstract/6B31A4EEDD134C2DPQ/1](https://www.proquest.com/docview/1436992455/abstract/6B31A4EEDD134C2DPQ/1)
- Johansen, O., & Omholt, A. (1966). A study of pulsating aurora. *Planetary and Space Science*,
14(2), 207–215. [https://doi.org/10.1016/0032-0633\(66\)90119-X](https://doi.org/10.1016/0032-0633(66)90119-X)
- Johnson, R. W. (2001). An introduction to the bootstrap. *Teaching Statistics*, 23(2), 49–54. <https://doi.org/10.1111/1467-9639.00050>
- Johnstone, A. D. (1978). Pulsating aurora. *Nature*, 274(5667), 119–126. [https://doi.org/10.1038/
274119a0](https://doi.org/10.1038/274119a0)
- Jones, S. L., Lessard, M. R., Rychert, K., Spanswick, E., & Donovan, E. (2011). Large-scale as-
pects and temporal evolution of pulsating aurora. *Journal of Geophysical Research: Space
Physics*, 116. <https://doi.org/10.1029/2010JA015840>
- Jones, S. L., Lessard, M. R., Rychert, K., Spanswick, E., Donovan, E., & Jaynes, A. N. (2013).
Persistent, widespread pulsating aurora: A case study. *Journal of Geophysical Research:
Space Physics*, 118(6), 2998–3006. <https://doi.org/10.1002/jgra.50301>
- Jones, S., Lessard, M., Fernandes, P., Lummerzheim, D., Semeter, J., Heinselman, C., Lynch, K.,
Michell, R., Kintner, P., Stenbaek-Nielsen, H., & Asamura, K. (2009). PFISR and ROPA

- observations of pulsating aurora. *Journal of Atmospheric and Solar-Terrestrial Physics*, 71(6), 708–716. <https://doi.org/10.1016/j.jastp.2008.10.004>
- Kaeppler, S. R., Sanchez, E., Varney, R. H., Irvin, R. J., Marshall, R. A., Bortnik, J., Reimer, A. S., & Reyes, P. M. (2020). Incoherent scatter radar observations of 10–100 keV precipitation: Review and outlook. *The Dynamic Loss of Earth's Radiation Belts*, 145–197. <https://doi.org/10.1016/B978-0-12-813371-2.00006-8>
- Kasahara, S., Miyoshi, Y., Yokota, S., Mitani, T., Kasahara, Y., Matsuda, S., Kumamoto, A., Matsuoka, A., Kazama, Y., Frey, H. U., Angelopoulos, V., Kurita, S., Keika, K., Seki, K., & Shinohara, I. (2018). Pulsating aurora from electron scattering by chorus waves. *Nature*, 554(7692), 337–340. <https://doi.org/10.1038/nature25505>
- Kennel, C. F., & Petschek, H. E. (1966). Limit on stably trapped particle fluxes. *Journal of Geophysical Research*, 71(1), 1–28. <https://doi.org/10.1029/JZ071i001p00001>
- Kennel, C. F., Scarf, F. L., Fredricks, R. W., McGehee, J. H., & Coroniti, F. V. (1970). VLF electric field observations in the magnetosphere. *Journal of Geophysical Research*, 75(31), 6136–6152. <https://doi.org/10.1029/JA075i031p06136>
- King, J. H. (2005). Solar wind spatial scales in and comparisons of hourly wind and ACE plasma and magnetic field data. *Journal of Geophysical Research*, 110, A02104. <https://doi.org/10.1029/2004JA010649>
- Kirkwood, S., & Osepian, A. (1995). Quantitative studies of energetic particle precipitation using incoherent scatter radar. *Journal of geomagnetism and geoelectricity*, 47(8), 783–799. <https://doi.org/10.5636/jgg.47.783>
- Kivelson, M. G., & Russell, C. T. (Eds.). (1995). *Introduction to space physics*. Cambridge University Press.
- Kletzing, C. A., Kurth, W. S., Acuna, M., MacDowall, R. J., Torbert, R. B., Averkamp, T., Bodet, D., Bounds, S. R., Chutter, M., Connerney, J., Crawford, D., Dolan, J. S., Dvorsky, R., Hospodarsky, G. B., Howard, J., Jordanova, V., Johnson, R. A., Kirchner, D. L., Mokrzycki, B., ... Tyler, J. (2013). The electric and magnetic field instrument suite and integrated

- science (EMFISIS) on RBSP. *Space Science Reviews*, 179(1), 127–181. <https://doi.org/10.1007/s11214-013-9993-6>
- Korth, H., Zhang, Y., Anderson, B. J., Sotirelis, T., & Waters, C. L. (2014). Statistical relationship between large-scale upward field-aligned currents and electron precipitation: Current-precipitation relationship. *Journal of Geophysical Research: Space Physics*, 119(8), 6715–6731. <https://doi.org/10.1002/2014JA019961>
- Kvammen, A., Wickstrøm, K., McKay, D., & Partamies, N. (2020). Auroral image classification with deep neural networks. *Journal of Geophysical Research: Space Physics*, 125(10). <https://doi.org/10.1029/2020JA027808>
- Kvifte, G., & Pettersen, H. (1969). Morphology of the pulsating aurora. *Planetary and Space Science*, 17(9), 1599–1607. [https://doi.org/10.1016/0032-0633\(69\)90148-2](https://doi.org/10.1016/0032-0633(69)90148-2)
- Lam, M. M., Horne, R. B., Meredith, N. P., Glauert, S. A., Moffat-Griffin, T., & Green, J. C. (2010). Origin of energetic electron precipitation >30 keV into the atmosphere. *Journal of Geophysical Research: Space Physics*, 115, n/a–n/a. <https://doi.org/10.1029/2009JA014619>
- Lawrence, D. J., Thomsen, M. F., Borovsky, J. E., & McComas, D. J. (1999). Measurements of early and late time plasmasphere refilling as observed from geosynchronous orbit. *Journal of Geophysical Research*, 104, 14691–14704. <https://doi.org/10.1029/1998ja900087>
- Lehtinen, N. G., & Inan, U. S. (2007). Possible persistent ionization caused by giant blue jets. *Geophysical Research Letters*, 34(8). <https://doi.org/10.1029/2006GL029051>
- Lessard, M. R. (2013). A review of pulsating aurora. *Geophysical Monograph Series*, 55–68. <https://doi.org/10.1029/2011GM001187>
- Li, W., Santolik, O., Bortnik, J., Thorne, R. M., Kletzing, C. A., Kurth, W. S., & Hospodarsky, G. B. (2016). New chorus wave properties near the equator from van allen probes wave observations. *Geophysical Research Letters*, 43(10), 4725–4735. <https://doi.org/10.1002/2016GL068780>

- Lorentzen, K. R., Looper, M. D., & Blake, J. B. (2001). Relativistic electron microbursts during the GEM storms. *Geophysical Research Letters*, 28(13), 2573–2576. <https://doi.org/10.1029/2001GL012926>
- Lui, A., Perreault, P., Akasofu, S.-I., & Anger, C. (1973). The diffuse aurora. *Planetary and Space Science*, 21(5), 857–861. [https://doi.org/10.1016/0032-0633\(73\)90102-5](https://doi.org/10.1016/0032-0633(73)90102-5)
- Luo, B., Li, X., Temerin, M., & Liu, S. (2013). Prediction of the AU , AL , and AE indices using solar wind parameters. *Journal of Geophysical Research: Space Physics*, 118(12), 7683–7694. <https://doi.org/10.1002/2013JA019188>
- Mamajek, E. E., Prsa, A., Torres, G., Harmanec, P., Asplund, M., Bennett, P. D., Capitaine, N., Christensen-Dalsgaard, J., Depagne, E., Folkner, W. M., Haberreiter, M., Hekker, S., Hilton, J. L., Kostov, V., Kurtz, D. W., Laskar, J., Mason, B. D., Milone, E. F., Montgomery, M. M., ... Stewart, S. G. (2015). IAU 2015 resolution b3 on recommended nominal conversion constants for selected solar and planetary properties [Publisher: arXiv Version Number: 1]. <https://doi.org/10.48550/ARXIV.1510.07674>
- Marshall, R. A., Xu, W., Kero, A., Kabirzadeh, R., & Sanchez, E. (2019). Atmospheric effects of a relativistic electron beam injected from above: Chemistry, electrodynamics, and radio scattering. *Frontiers in Astronomy and Space Sciences*, 6, 6. <https://doi.org/10.3389/fspas.2019.00006>
- Mauk, B., N. J. Fox, Fox, N. J., Kanekal, S., Kessel, R., Sibeck, D. G., & Ukhorskiy, A. Y. (2013). Science objectives and rationale for the radiation belt storm probes mission. *Space Science Reviews*, 179(1), 3–27. <https://doi.org/10.1007/s11214-012-9908-y>
- McEwen, D., & Bryant, D. (1978). Optical-particle characteristics of pulsating aurora. *Journal of Atmospheric and Terrestrial Physics*, 40(7), 871–876. [https://doi.org/10.1016/0021-9169\(78\)90037-5](https://doi.org/10.1016/0021-9169(78)90037-5)
- Meng, C.-I., Mauk, B., & McIlwain, C. (1979). Electron precipitation of evening diffuse aurora and its conjugate electron fluxes near the magnetospheric equator. *Journal of Geophysical Research*, 84, 2545. <https://doi.org/10.1029/JA084iA06p02545>

- Meredith, N. P., Horne, R. B., Johnstone, A. D., & Anderson, R. R. (2000). The temporal evolution of electron distributions and associated wave activity following substorm injections in the inner magnetosphere. *Journal of Geophysical Research: Space Physics*, *105*, 12907–12917. <https://doi.org/10.1029/2000JA900010>
- Meredith, N. P., Horne, R. B., Li, W., Thorne, R. M., & Sicard-Piet, A. (2014). Global model of low-frequency chorus ($f_{\text{LHR}} < f < 0.1 f_{\text{ce}}$) from multiple satellite observations. *Geophysical Research Letters*, *41*(2), 280–286. <https://doi.org/10.1002/2013GL059050>
- Meredith, N. P., Horne, R. B., Shen, X.-C., Li, W., & Bortnik, J. (2020). Global model of whistler mode chorus in the near-equatorial region ($|\lambda_m| < 18^\circ$). *Geophysical Research Letters*, *47*(11). <https://doi.org/10.1029/2020GL087311>
- Meredith, N. P., Horne, R. B., Thorne, R. M., & Anderson, R. R. (2009). Survey of upper band chorus and ECH waves: Implications for the diffuse aurora. *Journal of Geophysical Research: Space Physics*, *114*, n/a–n/a. <https://doi.org/10.1029/2009JA014230>
- Mitra, A. (1981). Chemistry of middle atmospheric ionization—a review. *Journal of Atmospheric and Terrestrial Physics*, *43*(8), 737–752. [https://doi.org/10.1016/0021-9169\(81\)90050-7](https://doi.org/10.1016/0021-9169(81)90050-7)
- Miyoshi, Y., Hosokawa, K., Kurita, S., Oyama, S.-I., Ogawa, Y., Saito, S., Shinohara, I., Kero, A., Turunen, E., Verronen, P. T., Kasahara, S., Yokota, S., Mitani, T., Takashima, T., Higashio, N., Kasahara, Y., Matsuda, S., Tsuchiya, F., Kumamoto, A., ... Nakamura, S. (2021). Penetration of MeV electrons into the mesosphere accompanying pulsating aurorae. *Scientific Reports*, *11*(1), 13724. <https://doi.org/10.1038/s41598-021-92611-3>
- Miyoshi, Y., Saito, S., Kurita, S., Asamura, K., Hosokawa, K., Sakanoi, T., Mitani, T., Ogawa, Y., Oyama, S., Tsuchiya, F., Jones, S. L., Jaynes, A. N., & Blake, J. B. (2020). Relativistic electron microbursts as high-energy tail of pulsating aurora electrons. *Geophysical Research Letters*, *47*(21). <https://doi.org/10.1029/2020GL090360>
- Nanjo, S., Hozumi, Y., Hosokawa, K., Kataoka, R., Miyoshi, Y., Oyama, S.-i., Ozaki, M., Shiokawa, K., & Kurita, S. (2021). Periodicities and colors of pulsating auroras: DSLR cam-

- era observations from the international space station. *Journal of Geophysical Research: Space Physics*, 126(10). <https://doi.org/10.1029/2021JA029564>
- Newell, P. T., & Gjerloev, J. W. (2011a). Evaluation of SuperMAG auroral electrojet indices as indicators of substorms and auroral power. *Journal of Geophysical Research: Space Physics*, 116, 2011JA016779. <https://doi.org/10.1029/2011JA016779>
- Newell, P. T., & Gjerloev, J. W. (2011b). Substorm and magnetosphere characteristic scales inferred from the SuperMAG auroral electrojet indices. *Journal of Geophysical Research: Space Physics*, 116, 2011JA016936. <https://doi.org/10.1029/2011JA016936>
- Newell, P. T., Sotirelis, T., & Wing, S. (2009). Diffuse, monoenergetic, and broadband aurora: The global precipitation budget. *Journal of Geophysical Research: Space Physics*, 114, n/a–n/a. <https://doi.org/10.1029/2009JA014326>
- Ni, B., Thorne, R. M., Meredith, N. P., Horne, R. B., & Shprits, Y. Y. (2011). Resonant scattering of plasma sheet electrons leading to diffuse auroral precipitation: 2. evaluation for whistler mode chorus waves: DIFFUSE AURORAL SCATTERING BY CHORUS. *Journal of Geophysical Research: Space Physics*, 116, n/a–n/a. <https://doi.org/10.1029/2010JA016233>
- Ni, B., Thorne, R. M., Shprits, Y. Y., & Bortnik, J. (2008). Resonant scattering of plasma sheet electrons by whistler-mode chorus: Contribution to diffuse auroral precipitation. *Geophysical Research Letters*, 35(11), L11106. <https://doi.org/10.1029/2008GL034032>
- Ni, B., Thorne, R. M., Zhang, X., Bortnik, J., Pu, Z., Xie, L., Hu, Z.-j., Han, D., Shi, R., Zhou, C., & Gu, X. (2016). Origins of the earth's diffuse auroral precipitation. *Space Science Reviews*, 200(1), 205–259. <https://doi.org/10.1007/s11214-016-0234-7>
- Nishimura, Y., Bortnik, J., Li, W., Thorne, R. M., Lyons, L. R., Angelopoulos, V., Mende, S. B., Bonnell, J. W., Le Contel, O., Cully, C., Ergun, R., & Auster, U. (2010). Identifying the driver of pulsating aurora. *Science*, 330(6000), 81–84. <https://doi.org/10.1126/science.1193186>
- Nishimura, Y., Bortnik, J., Li, W., Thorne, R. M., Chen, L., Lyons, L. R., Angelopoulos, V., Mende, S. B., Bonnell, J., Le Contel, O., Cully, C., Ergun, R., & Auster, U. (2011). Multievent

- study of the correlation between pulsating aurora and whistler mode chorus emissions. *Journal of Geophysical Research: Space Physics*, 116, n/a–n/a. <https://doi.org/10.1029/2011JA016876>
- Oguti, T., Kokubun, S., Hayashi, K., Tsuruda, K., Machida, S., Kitamura, T., Saka, O., & Watanabe, T. (1981). Statistics of pulsating auroras on the basis of all-sky TV data from five stations. i. occurrence frequency. *Canadian Journal of Physics*, 59(8), 1150–1157. <https://doi.org/10.1139/p81-152>
- Oguti, T. (1976). Recurrent auroral patterns. *Journal of Geophysical Research*, 81(10), 1782–1786. <https://doi.org/10.1029/JA081i010p01782>
- Ohtani, S., & Gjerloev, J. W. (2020). Is the substorm current wedge an ensemble of wedgelets?: Revisit to midlatitude positive bays. *Journal of Geophysical Research: Space Physics*, 125(9). <https://doi.org/10.1029/2020JA027902>
- Olifer, L., Feltman, C., Ghaffari, R., Henderson, S., Huyghebaert, D., Burchill, J., Jaynes, A. N., Knudsen, D., McWilliams, K., Moen, J. I., Spicher, A., & Wu, J. (2021). Swarm observations of dawn/dusk asymmetries between pedersen conductance in upward and downward field-aligned current regions. *Earth and Space Science*, 8(7). <https://doi.org/10.1029/2020EA001167>
- Osepian, A., Kirkwood, S., Dalin, P., & Tereschenko, V. (2009). D-region electron density and effective recombination coefficients during twilight – experimental data and modelling during solar proton events. *Annales Geophysicae*, 27(10), 3713–3724. <https://doi.org/10.5194/angeo-27-3713-2009>
- Oyama, S., Kero, A., Rodger, C. J., Clilverd, M. A., Miyoshi, Y., Partamies, N., Turunen, E., Raita, T., Verronen, P. T., & Saito, S. (2017). Energetic electron precipitation and auroral morphology at the substorm recovery phase. *Journal of Geophysical Research: Space Physics*, 122(6), 6508–6527. <https://doi.org/10.1002/2016JA023484>
- Partamies, N., Whiter, D., Kadokura, A., Kauristie, K., Nesse Tyssøy, H., Massetti, S., Stauning, P., & Raita, T. (2017). Occurrence and average behavior of pulsating aurora. *Journal of*

- Geophysical Research: Space Physics*, 122(5), 5606–5618. <https://doi.org/10.1002/2017JA024039>
- Partamies, N., Tesema, F., & Bland, E. (2022). Appearance and precipitation characteristics of high-latitude pulsating aurora. *Frontiers in Astronomy and Space Sciences*, 9, 923396. <https://doi.org/10.3389/fspas.2022.923396>
- Roederer, J. G. (1970). *Dynamics of geomagnetically trapped radiation* (Vol. 2). Springer Berlin Heidelberg. <https://doi.org/10.1007/978-3-642-49300-3>
- Rogowitz, B., & Treinish, L. (1998). Data visualization: The end of the rainbow. *IEEE Spectrum*, 35(12), 52–59. <https://doi.org/10.1109/6.736450>
- Rosebrock, A. (2019, July 15). *Video classification with keras and deep learning* [PyImageSearch]. Retrieved March 18, 2023, from <https://pyimagesearch.com/2019/07/15/video-classification-with-keras-and-deep-learning/>
- Royrvik, O. (1976). *Pulsating aurora: Local and global morphology* (Doctoral dissertation). University of Alaska Fairbanks. <https://hdl.handle.net/11122/9248>
- Royrvik, O., & Davis, T. N. (1977). Pulsating aurora: Local and global morphology. *Journal of Geophysical Research*, 82(29), 4720–4740. <https://doi.org/10.1029/JA082i029p04720>
- Russell, C. T., Luhmann, J. G., & Strangeway, R. J. (2016). *Space physics: An introduction*. Cambridge University Press.
- Samara, M., Michell, R. G., & Redmon, R. J. (2015). Low-altitude satellite measurements of pulsating auroral electrons. *Journal of Geophysical Research: Space Physics*, 120(9), 8111–8124. <https://doi.org/10.1002/2015JA021292>
- Sandahl, I., Eliasson, L., & Lundin, R. (1980). Rocket observations of precipitating electrons over a pulsating aurora. *Geophysical Research Letters*, 7(5), 309–312. <https://doi.org/10.1029/GL007i005p00309>
- Sandford, P. (1968). Variations of auroral emissions with time, magnetic activity and the solar cycle. *Journal of Atmospheric and Terrestrial Physics*, 30(12), 1921–1942. [https://doi.org/10.1016/0021-9169\(68\)90001-9](https://doi.org/10.1016/0021-9169(68)90001-9)

- Schroeder, J. W. R., Howes, G. G., Kletzing, C. A., Skiff, F., Carter, T. A., Vincena, S., & Dorfman, S. (2021). Laboratory measurements of the physics of auroral electron acceleration by alfvén waves. *Nature Communications*, 12(1), 3103. <https://doi.org/10.1038/s41467-021-23377-5>
- Semeter, J., & Kamalabadi, F. (2005). Determination of primary electron spectra from incoherent scatter radar measurements of the auroral region. *Radio Science*, 40(2), n/a–n/a. <https://doi.org/10.1029/2004RS003042>
- Sergienko, T., Sandahl, I., Gustavsson, B., Andersson, L., Brändström, U., & Steen, Å. (2008). A study of fine structure of diffuse aurora with ALIS-FAST measurements. *Annales Geophysicae*, 26(11), 3185–3195. <https://doi.org/10.5194/angeo-26-3185-2008>
- Shaw, R. R., & Gurnett, D. A. (1975). Electrostatic noise bands associated with the electron gyrofrequency and plasma frequency in the outer magnetosphere. *Journal of Geophysical Research*, 80(31), 4259–4271. <https://doi.org/10.1029/JA080i031p04259>
- Sheeley, B. W., Moldwin, M. B., Rassoul, H. K., & Anderson, R. R. (2001). An empirical plasma-sphere and trough density model: CRRES observations. *Journal of Geophysical Research: Space Physics*, 106, 25631–25641. <https://doi.org/10.1029/2000JA000286>
- Shumko, M., Chaddock, D., Gallardo-Lacourt, B., Donovan, E., Spanswick, E. L., Halford, A. J., Thompson, I., & Murphy, K. R. (2022). AuroraX, PyAuroraX, and aurora-asi-lib: A user-friendly auroral all-sky imager analysis framework. *Frontiers in Astronomy and Space Sciences*, 9, 1009450. <https://doi.org/10.3389/fspas.2022.1009450>
- Sivadas, N., Semeter, J., Nishimura, Y., & Kero, A. (2017). Simultaneous measurements of substorm-related electron energization in the ionosphere and the plasma sheet. *Journal of Geophysical Research: Space Physics*, 122(10). <https://doi.org/10.1002/2017JA023995>
- Soni, P. K., Kakad, B., & Kakad, A. (2021). Simulation study of motion of charged particles trapped in earth's magnetosphere. *Advances in Space Research*, 67(2), 749–761. <https://doi.org/10.1016/j.asr.2020.10.020>

- Spence, H. E., Reeves, G. D., Baker, D. N., Blake, J. B., Bolton, M., Bourdarie, S., Chan, A. A., Claudepierre, S. G., Clemmons, J. H., Cravens, J. P., Elkington, S. R., Fennell, J. F., Friedel, R. H. W., Funsten, H. O., Goldstein, J., Green, J. C., Guthrie, A., Henderson, M. G., Horne, R. B., ... Thorne, R. M. (2013). Science goals and overview of the radiation belt storm probes (RBSP) energetic particle, composition, and thermal plasma (ECT) suite on NASA's van allen probes mission. *Space Science Reviews*, 179(1), 311–336. <https://doi.org/10.1007/s11214-013-0007-5>
- Tesema, F., Partamies, N., Nesse Tyssøy, H., & McKay, D. (2020). Observations of precipitation energies during different types of pulsating aurora. *Annales Geophysicae*, 38(6), 1191–1202. <https://doi.org/10.5194/angeo-38-1191-2020>
- Tesema, F., Partamies, N., Tyssøy, H. N., Kero, A., & Smith-Johnsen, C. (2020). Observations of electron precipitation during pulsating aurora and its chemical impact. *Journal of Geophysical Research: Space Physics*, 125(6). <https://doi.org/10.1029/2019JA027713>
- Thorne, R. M., Smith, E. J., Fiske, K. J., & Church, S. R. (1974). Intensity variation of ELF hiss and chorus during isolated substorms. *Geophysical Research Letters*, 1(5), 193–196. <https://doi.org/10.1029/GL001i005p00193>
- Thorne, R. M., Ni, B., Tao, X., Horne, R. B., & Meredith, N. P. (2010). Scattering by chorus waves as the dominant cause of diffuse auroral precipitation. *Nature*, 467(7318), 943–946. <https://doi.org/10.1038/nature09467>
- Trakhtengerts, V. Y., Demekhov, A. G., Titova, E. E., Kozelov, B. V., Santolik, O., Gurnett, D., & Parrot, M. (2004). Interpretation of cluster data on chorus emissions using the backward wave oscillator model. *Physics of Plasmas*, 11(4), 1345–1351. <https://doi.org/10.1063/1.1667495>
- Trondsen, T. (1998). *High spatial and temporal resolution auroral imaging high spatial and temporal resolution auroral imaging* (Doctoral dissertation).

- Trondsen, T. S., & Cogger, L. L. (1997). High-resolution television observations of black aurora. *Journal of Geophysical Research: Space Physics*, 102, 363–378. <https://doi.org/10.1029/96JA03106>
- Troyer, R., Jaynes, A., Jones, S., Kaeppler, S., Varney, R., & Reimer, A. (2022, July 21). PFRR ASC image dataset for troyer et al. 2022 (substorm activity as a driver of energetic pulsating aurora) [Type: dataset]. <https://doi.org/10.5281/ZENODO.6878145>
- Troyer, R. N., Jaynes, A. N., Kaeppler, S. R., Varney, R. H., Reimer, A. S., & Jones, S. L. (2022). Substorm activity as a driver of energetic pulsating aurora. *Frontiers in Astronomy and Space Sciences*, 9. <https://doi.org/10.3389/fspas.2022.1032552>
- Tsurutani, B. T., & Smith, E. J. (1974). Postmidnight chorus: A substorm phenomenon. *Journal of Geophysical Research*, 79(1), 118–127. <https://doi.org/10.1029/JA079i001p00118>
- Turunen, E., Kero, A., Verronen, P. T., Miyoshi, Y., Oyama, S.-I., & Saito, S. (2016). Mesospheric ozone destruction by high-energy electron precipitation associated with pulsating aurora. *Journal of Geophysical Research: Atmospheres*, 121(19). <https://doi.org/10.1002/2016JD025015>
- Van Allen, J. A. (1959). Radiation belts around the earth. *Scientific American*, 200(3), 39–46. <https://doi.org/10.1038/scientificamerican0359-39>
- van der Walt, S., & Smith, N. (2020). *Matplotlib colormaps*. Retrieved March 6, 2023, from <https://bids.github.io/colormap/>
- Verronen, P. T., Kero, A., Partamies, N., Szélag, M. E., Oyama, S.-I., Miyoshi, Y., & Turunen, E. (2021). Simulated seasonal impact on middle atmospheric ozone from high-energy electron precipitation related to pulsating aurorae. *Annales Geophysicae*, 39(5), 883–897. <https://doi.org/10.5194/angeo-39-883-2021>
- Vickrey, J. F., Vondrak, R. R., & Matthews, S. J. (1982). Energy deposition by precipitating particles and joule dissipation in the auroral ionosphere. *Journal of Geophysical Research: Space Physics*, 87, 5184–5196. <https://doi.org/10.1029/JA087iA07p05184>

- Ware, C. (2004). *Information visualization: Perception for design* (2. ed., [Nachdr.]). Elsevier/Morgan Kaufmann. https://www.researchgate.net/publication/224285723_Information_Visualization_Perception_for_Design_Second_Edition
- Whalen, B. A., Miller, J. R., & McDiarmid, I. B. (1971). Energetic particle measurements in a pulsating aurora. *Journal of Geophysical Research*, 76(4), 978–986. <https://doi.org/10.1029/JA076i004p00978>
- Whiter, D. K., Partamies, N., Gustavsson, B., & Kauristie, K. (2022, September 2). *The altitude of green OI 557.7 nm and blue n_2^+ 427.8 nm aurora* (preprint). Earth's ionosphere & aeronomy/Auroral ionosphere. <https://doi.org/10.5194/angeo-2022-23>
- Wing, S., Gkioulidou, M., Johnson, J. R., Newell, P. T., & Wang, C.-P. (2013). Auroral particle precipitation characterized by the substorm cycle. *Journal of Geophysical Research: Space Physics*, 118(3), 1022–1039. <https://doi.org/10.1002/jgra.50160>
- Wygant, J. R., Bonnell, J. W., Goetz, K., Keith Goetz, Ergun, R., Mozer, F. S., Bale, S. D., Ludlam, M., Ludlam, M., Paul Turin, Turin, P., Harvey, P., Hochmann, R., Harps, K., Dalton, G., Dalton, G., J. McCauley, McCauley, J., Rachelson, W., ... Tao, J. B. (2013). The electric field and waves instruments on the radiation belt storm probes mission. *Springer US*. <https://doi.org/10.1007/s11214-013-0013-7>
- Yamamoto, T. (1988). On the temporal fluctuations of pulsating auroral luminosity. *Journal of Geophysical Research*, 93, 897. <https://doi.org/10.1029/JA093iA02p00897>

APPENDIX A: THE USE OF COLOR IN SCIENTIFIC PLOTS

In space physics we often use color to represent a third variable. For instance, temperature as a function of some latitude and longitude, or wave power as a function of time and frequency. The human eye interprets color in a very specific way based on our evolution. For instance, we interpret green as brighter than other colors. Because of this, when we use color to represent numerical data we need to think carefully about how that color is going to get interpreted. In certain cases, our figure might only be for artistic purposes, but I believe in most cases we use the colormap to help understand the underlying data.

What I am about to state could be controversial in certain areas of the field, but it is backed up by evidence. In nearly all cases, the rainbow (Jet) colormap is a terrible (nearly the worst) option for visualizing scientific data. This comes down to three main reasons:

1. The rainbow colormap does not have a naturally perceived order.
2. The rainbow colormap introduces artificial boundaries and gradients in our data.
3. The rainbow colormap obscures trends in our data that fall on certain colors.

We will go through each of these reasons and explore them in more length. There is also the issue of people with color deficiencies (color blindness). However, I leave this out of the main reasons because for these people the issues aren't much different, just more dramatic. For an even more complete discussion about this topic, I would recommend the Nature Communications article Crameri, Shephard, and Heron (2020).

A.1 Naturally Perceived Order

Figure A.1 shows how the rainbow color map does not have a naturally perceived order. It is immediately intuitive how to order the grayscale circles. Darker gray on one side, lighter on the other. For the colored circles, this is not true. There is no reason that red is greater than blue, despite that usually being the convention. As Borland and Taylor (2007) and Ware (2004) explain, for

ordinary people arranging a sequence of colors in order is confusing and the results likely varied. To arrange the rainbow colormap as it is usually done in our field we have to remember that red values are high and the mnemonic ROYGBIV. One might argue that there is a natural ordering to the colormap, wavelength. While this is true, as we have just seen, our eyes do not perceive an increase in wavelength as an increase in value.

Visualizations are designed to quickly and clearly convey our data. If our data has an order (some values are higher than others) the rainbow colormap is a poor choice because it makes it difficult to determine which values are order above or below another.

A.2 Artificial Boundaries And Gradients

In the rainbow colormap we perceive the transition between colors differently depending on the color. For instance the transition between light blue to turquoise looks very sharp, while between green and yellow it is much less obvious. This causes artificial boundaries and makes gradients seem steeper or less so than in reality. Figure A.2 is a representation of four different dataset from Borland and Taylor Ii (2007). Notice how the rainbow colormaps creates artificial boundaries and sharp gradients in the first and third columns. These boundaries are not visible in the other plots and do not exist in the underlying data.

Artifacts like this can have very real consequences. Dry (2018) discusses a case where the Trump administration advised the public about the dangers of Hurricane Florence using a rainbow colormap. In this map there was what appeared to be a sharp boundary that would represent a large drop in probability of storm force winds. In reality the drop was only 10%. This could have resulted in poor policy and decision making.

A.3 Obscuring Features

In addition to creating artifacts in the data, the rainbow colormap can also obscure important information. Figure A.3 is another image from Borland and Taylor Ii (2007), which shows how this is true, particularly for values that map to near the color green. The human eye perceives high

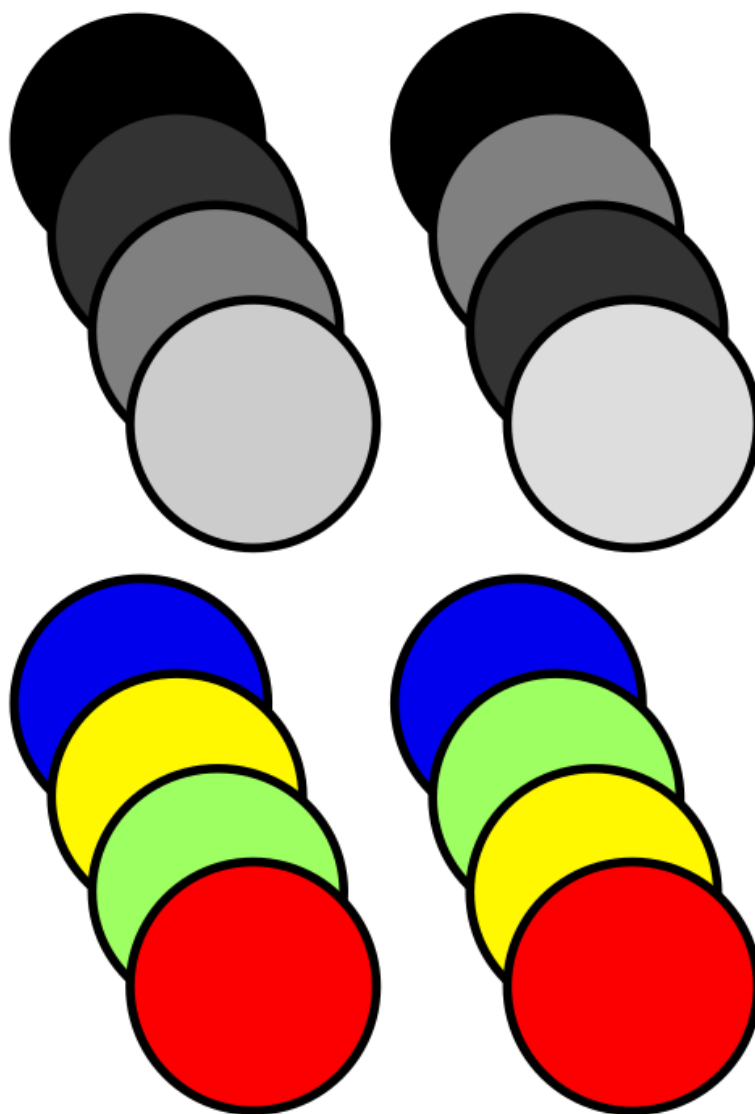


Figure A.1. A demonstration why the rainbow colormaps does not have a naturally perceived order. Which grayscale sequence is in order? Now which color sequence is in order?

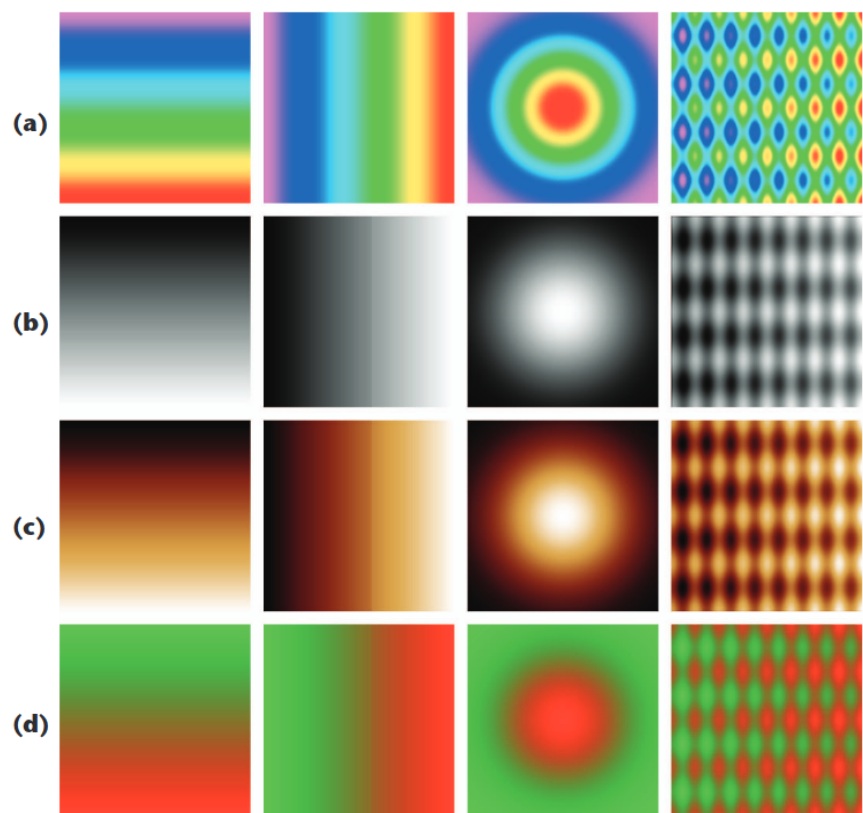


Figure A.2. Four different data sets from Borland and Taylor Ii (2007) plotted with four different colormaps. Notice the artificial gradients in the first and third columns for the rainbow colormap.

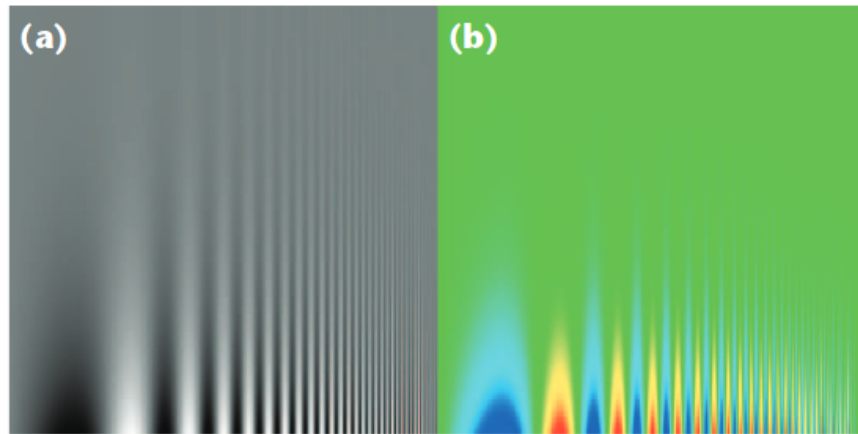


Figure A.3. A figure from Borland and Taylor Ii (2007) demonstrating how the rainbow colormap can obscure data, particularly near the color green.

spatial frequencies through changes in brightness, not hue (Rogowitz & Treinish, 1998). Because the rainbow colormap doesn't change in brightness over portions, like the greens, it is very difficult to pick out small details.

Because of these issues the rainbow colormap is particularly bad for values that vary around a central value. For instance global elevation as Figure A.4 shows. In the plot, sea level falls directly within the greens and so small variations in elevation around sea level, like the Appalachian Mountains, are difficult to view. A better way to plot data like this is with a diverging colormap, which the bottom panel shows.

We've seen that the rainbow colormap is one of the worst ways to represent most scientific data. There have even been studies demonstrating what effect this can have. Borkin, Gajos, Peters, et al. (2011) found that medical students examining diagnostic images made more errors identifying disease when the images were plotted in the rainbow colormap. That was despite them preferring the look of the rainbow colormap because it was familiar. So, what should we use instead? Cramer, Shephard, and Heron (2020) provides a very detailed flow chart and a list of colormaps that you can refer to, but I generally consider three options.

1. If your data varies between high and low values with no clear central value use a perceptually uniform colormap. One good option is Viridis, which is included in Python's Matplotlib

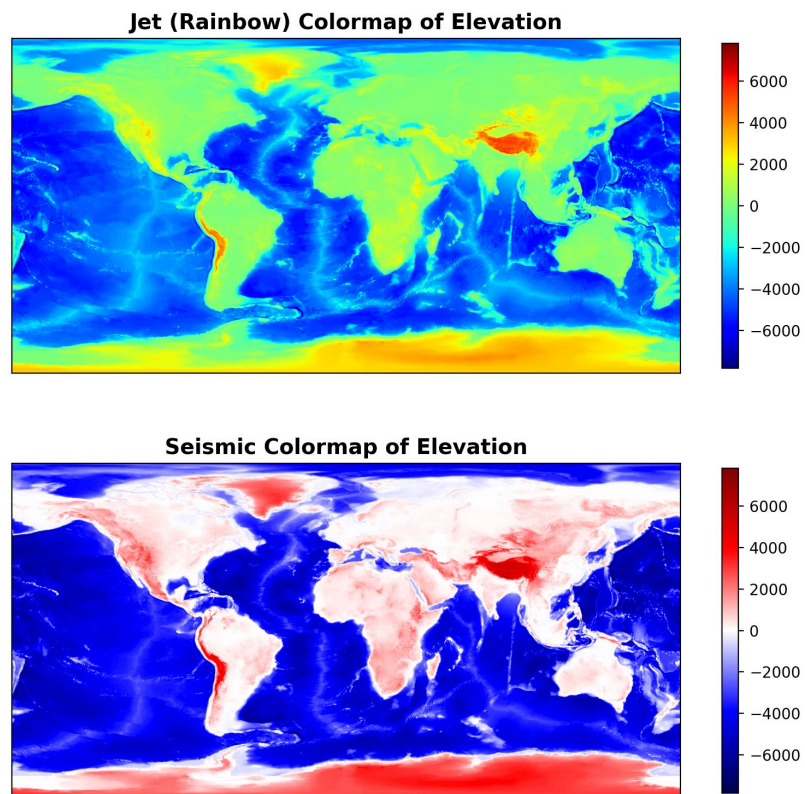


Figure A.4. A plot of global elevation based on sea level for both the rainbow colormap and Seismic, diverging colormap. Small variations around sea level are difficult to view in the rainbow colormap.

plotting package and available at van der Walt and Smith (2020). Another is the colormaps of Crameri (2018), available at Crameri (2021).

2. If your data varies between high and low values, but also has a central value, such as deviations in temperature around a baseline or elevation above/below sea level, use a diverging colormap. See the references above for examples of these.
3. If your data does not vary between high and low values, such as geographic boundaries, then it is probably best to use colormaps designed for qualitative visualizations.
4. Finally, if the purpose of the visualization is artistic use whatever colormap you feel looks the best.

APPENDIX B: DERIVATIONS

B.1 Dipole Field

In the inner-magnetosphere, for many purposes, we can approximate the planet's magnetic field as a dipole. Because this is such an important field configuration to pulsating aurora and their source region in the outer Van Allen radiation belt, it is worth deriving here. We will be following the derivation as it is done in Griffiths (2013).

The electric field can be written as the negative gradient of something known as the scalar potential (V)

$$\vec{E} = -\nabla V \quad (\text{B.1})$$

This stems from the fact that an electric field has no curl. Because the magnetic field has no divergence, it can also be written in terms of a potential of sorts, called the vector potential \vec{A} , such that

$$\vec{B} = \nabla \times \vec{A} \quad (\text{B.2})$$

With this definition, we can write the static Ampère's law as

$$\nabla^2 \vec{A} = -\mu_0 \vec{J} \quad (\text{B.3})$$

This is essentially Poisson's equation.

$$\nabla^2 V = -\frac{\rho}{\epsilon_0} \quad (\text{B.4})$$

With $\mu_0 \vec{J}$ as the source. To solve Poisson's equation we go back to the definition of the scalar potential

$$V(\vec{r}) = -\int_{r_o}^{\vec{r}} \vec{E} \cdot d\vec{l} \quad (\text{B.5})$$

If we solve this for a point charge where $\vec{E} = \frac{q}{4\pi\epsilon_0 r^2} \hat{r}$ and, in spherical coordinates, $d\vec{l} = dr \hat{r} +$

$rd\theta \hat{\theta} + r\sin\phi \hat{\phi}$ it follows that

$$V(\vec{r}) = -\frac{1}{4\pi\epsilon_0} \int_{r_o}^r \frac{q}{r'^2} dr' = \frac{q}{4\pi\epsilon_0} \frac{1}{r'} \Big|_{\infty}^r = \frac{q}{4\pi\epsilon_0} \frac{1}{r} \quad (\text{B.6})$$

where r_o is our origin point, that we set to ∞ . For a continuous charge distribution this will become

$$V(\vec{r}) = \frac{1}{4\pi\epsilon_0} \int \frac{\rho(\vec{r}')}{z} d\tau' \quad (\text{B.7})$$

where z is the distance between the charge element and the measurement point \vec{r} , and $d\tau'$ is the infinitesimal volume element containing the charge (Griffiths, 2013). Now with this defined, we can go back to the vector potential and see that

$$\vec{A}(\vec{r}) = \frac{\mu_0}{4\pi} \int \frac{\vec{J}(\vec{r}')}{z} d\tau' \quad (\text{B.8})$$

To get the dipole field we would like to take the multipole expansion of \vec{A} , which means expanding in the form of a power series of $1/r$. As Griffiths (2013) derives in section 3.4

$$\frac{1}{z} = \frac{1}{r} \sum_{n=0}^{\infty} \left(\frac{r'}{r} \right)^n P_n(\cos\alpha) \quad (\text{B.9})$$

where P_n are the Legendre polynomials, and α is the angle between the vector from the origin to the infinitesimal current bit and the vector between the origin and the measurement point. For a current loop

$$\vec{A}(\vec{r}) = \frac{\mu_0 I}{4\pi} \oint \frac{1}{z} d\vec{l}' = \frac{\mu_0 I}{4\pi} \sum_{n=0}^{\infty} \frac{1}{r^{n+1}} \oint (r')^n P_n(\cos\alpha) d\vec{l}' \quad (\text{B.10})$$

$P_0 = 1$, which means that the monopole term is zero since $\oint d\vec{l}' = 0$ for a closed loop. The dipole term is

$$\vec{A}_{\text{dip}}(\vec{r}) = \frac{\mu_0 I}{4\pi r^2} \oint r' \cos\alpha d\vec{l}' = \frac{\mu_0 I}{4\pi r^2} \oint (\hat{r} \cdot \vec{r}') d\vec{l}' \quad (\text{B.11})$$

Given that

$$\oint (\hat{r} \cdot \vec{r}') d\vec{l}' = -\hat{r} \times \int d\vec{a}' \quad (\text{B.12})$$

and setting the magnetic dipole moment as

$$m = I \int d\vec{a} = I\vec{a} \quad (\text{B.13})$$

where \vec{a} is the vector area of the current loop. The dipole vector potential is then

$$\vec{A}_{\text{dip}}(\vec{r}) = \frac{\mu_0}{4\pi} \frac{\vec{m} \times \hat{r}}{r^2} \quad (\text{B.14})$$

Putting \vec{m} at the origin and letting it point in the \hat{z} direction causes $\vec{m} \times \hat{r} = m \sin \theta$ in spherical coordinates, and leads to

$$\vec{A}_{\text{dip}}(\vec{r}) = \frac{\mu_0}{4\pi} \frac{m \sin \theta}{r^2} \hat{\phi} \quad (\text{B.15})$$

Thus the magnetic field will be

$$\vec{B}(\vec{r}) = \nabla \times \vec{A}_{\text{dip}}(\vec{r}) \quad (\text{B.16})$$

$$= \frac{\mu_0 m}{4\pi r \sin \theta} \frac{\partial}{\partial \theta} \frac{\sin^2 \theta}{r^2} \hat{r} - \frac{\mu_0 m}{4\pi r} \frac{\partial}{\partial r} \frac{\sin \theta}{r} \hat{\theta} \quad (\text{B.17})$$

$$= \frac{\mu_0 m \cos \theta}{2\pi} \frac{1}{r^3} \hat{r} + \frac{\mu_0 m \sin \theta}{4\pi} \frac{1}{r^3} \hat{\theta} \quad (\text{B.18})$$

$$= \frac{\mu_0 m}{4\pi} \left(\frac{2 \cos \theta}{r^3} \hat{r} + \frac{\sin \theta}{r^3} \hat{\theta} \right) \quad (\text{B.19})$$

For the earth, the magnetic dipole moment is approximately the following (Kivelson & Russell, 1995).

$$M = \frac{\mu_0 m}{4\pi} \approx 8 \times 10^{15} \text{ T} \cdot \text{m}^3 \quad (\text{B.20})$$

The magnetic field line of a dipole must be tangent to the magnetic field direction at every point,

such that

$$d\phi = 0 \text{ and } \frac{rd\theta}{B_\theta} = \frac{dr}{B_r} \implies \frac{r^4}{\sin\theta}d\theta = \frac{r^3}{2\cos\theta}dr \implies 2\cot\theta d\theta = \frac{1}{r}dr \quad (\text{B.21})$$

Integrating both sides of this

$$2\ln(\sin\theta) + C = \ln r \implies r = r_0 \sin^2\theta \quad (\text{B.22})$$

where r_0 is the distance to the equatorial crossing of the field line. We can also write this in terms of magnetic latitude as that is more frequently used. Here we also change the constant to L . This is the constant that we use often in the field to designate a specific field line.

$$\frac{r}{R_E} = L\cos^2\lambda \quad (\text{B.23})$$

where R_E is the radius of the earth.

B.2 Plasma Parameter

Assuming a gas of charged particles is quasi-neutral, such that $n_e \approx n_i$, we can calculate the potential of one of these particles. We will pick an ion (proton). In the absence of all other particles the potential will be

$$\phi = \frac{q_i}{4\pi\epsilon_0 r} \quad (\text{B.24})$$

Within the plasma the potential will be distorted, but still must satisfy Poisson's equation.

$$\nabla^2\phi = -\frac{e}{\epsilon_0}(n_i - n_e) \quad (\text{B.25})$$

Very close to the proton, $n_e \neq n_i$, instead we can determine n_e using Boltzmann's law for a Maxwellian distribution.

$$n_e = n_0 e^{e\phi/k_B T_e} \quad (\text{B.26})$$

where k_B is the Boltzmann constant, n_0 is the number density assumed by quasi-neutrality, and T_e is the temperature of the electrons. Assuming the potential is weak such that $e\phi \ll k_B T_e$, we can substitute this into Poisson's equation and do a Taylor expansion, taking only the first order terms.

$$\nabla^2 \phi = -\frac{n_0 e}{\epsilon_0} \left(1 - e^{e\phi/k_B T_e}\right) \approx \frac{n_0 e^2}{\epsilon_0 k_B T_e} \phi \quad (\text{B.27})$$

Assuming a spherically symmetric potential the differential equation becomes

$$\frac{\partial^2}{\partial r^2}(r\phi) - \frac{n_0 e^2}{\epsilon_0 k_B T_e}(r\phi) = 0 \quad (\text{B.28})$$

Solutions to this equation are of the form

$$\phi(r) = \frac{C}{r} e^{-r/\lambda_D} \quad (\text{B.29})$$

with

$$\lambda_D^2 = \frac{\epsilon_0 k_B T_e}{n_0 e^2} \quad (\text{B.30})$$

λ_D is called the Debye length and describe the distance over which our proton can influence electrons and perturb the plasma. The number of particles within the sphere of length λ_D around the proton will be:

$$N_D = n_0 \lambda_D^3 \quad (\text{B.31})$$

and is called the plasma parameter. For an ideal plasma $N_D \gg 1$.

B.3 Gradient Curvature Drift

The drift of energetic electrons around Earth's dipole magnetic field is one of the most important motions for pulsating aurora. To derive the mathematics underpinning this motion we will also derive other important particle motions such as the cyclotron frequency, and bounce motion. Our first step will be to see how a charged particle would behave in a uniform magnetic

field. We'll assume that the particle has some velocity \vec{v} and charge q . We'll also define the pitch angle α between the particle velocity and the magnetic field such that $\vec{v} \cdot \vec{B} = vB \cos \alpha$. The Lorentz force defines the force a charged particle feels

$$\vec{F} = m \frac{d\vec{v}}{dt} = q\vec{E} + q\vec{v} \times \vec{B} + \vec{F}_g \quad (\text{B.32})$$

where \vec{E} is the electric field, \vec{B} is the magnetic field, and \vec{F}_g represents any non-electromagnetic forces such as gravity. For our purposes, we'll assume that $\vec{E} = 0$ and $\vec{F}_g = 0$. We'll also let $\hat{B} = \hat{z}$ and $\alpha = 90^\circ$, it then follows that in Cartesian coordinates

$$m\dot{v}_x = qv_y B \quad m\dot{v}_y = -qv_x B \quad (\text{B.33})$$

Taking the derivative with time one more time for each of these components we get

$$m\ddot{v}_x = q\dot{v}_y B \quad m\ddot{v}_y = -q\dot{v}_x B \quad (\text{B.34})$$

Combining these two equations we can see that

$$\ddot{v}_{x,y} = -\left(\frac{qB}{m}\right)^2 v_{x,y} \quad (\text{B.35})$$

This is a harmonic oscillator representing circular motion! The frequency of the motion, called cyclotron frequency, is $\Omega_c = qB/m$ in radians per second. For a negative charge the motion will be right-handed and a positive charge will be left-handed. To determine the gyroradius, ρ_c , of this motion we first look at the centripetal force

$$F_g = \frac{mv_\perp^2}{\rho_c} = qv_\perp B \implies \rho_c = \frac{mv_\perp}{qB} \quad (\text{B.36})$$

If $\alpha < 90^\circ$ then the particle will still gyrate around the magnetic field, but will now also have an additional component to the velocity along the magnetic field line, causing it to spiral along the

field line infinitely, assuming nothing else changes. However, in the magnetosphere, this is not a valid assumption. As we derived in Section B.1 the dipole magnetic field of the earth is not constant along \hat{r} or $\hat{\theta}$.

As a charged particle spirals through this field it will experience different forces depending on where it is. To explore this, let's first consider a charged particle with $\alpha = 90^\circ$ gyrating around a magnetic field line at the magnetic equator where $\theta = 90^\circ$, thus $\vec{B} = B_\theta = M/r^3$. At this location there is only a gradient in the magnetic field in the \hat{r} direction, or perpendicular to the magnetic field. In the gyrating circle at the point closest to the earth (smallest r) the particle will feel a larger Lorentz force than at the point furthest from the earth (largest r). This means that there will be a net Lorentz force in the direction of $-\nabla_\perp B$, or away from the earth. To compute this average force we must integrate around one full gyration.

$$F_{\nabla_\perp B} = \frac{1}{2\pi} \int_0^{2\pi} qv_\perp (B + \nabla_\perp B \rho_c \cos \phi) \cos \phi d\phi = \frac{qv_\perp \nabla_\perp B \rho_c}{2\pi} \int_0^{2\pi} \cos^2 \phi d\phi = \frac{qv_\perp \nabla_\perp B \rho_c}{2} \quad (\text{B.37})$$

where B is the average magnetic field strength over the full gyration and ρ_c is the gyroradius. Also note that this force points in the direction opposite to the gradient. Now we must consider how a force like this will affect the particle motion. One neat trick is to find a reference frame where the induced electric field balances out this force. We can do that with the following equality

$$q\vec{E}^* + \vec{F}^* = q\vec{v}_\nabla \times \vec{B} + \vec{F}_\nabla = 0 \quad (\text{B.38})$$

where the $*$ indicates the new reference frame. Taking the cross product of \hat{B}/qB on both sides

$$\frac{\vec{v}_\nabla \times \vec{B} \times \hat{B}}{B} = -\frac{\vec{F}_\nabla \times \hat{B}}{qB} \quad (\text{B.39})$$

The first term is just $\vec{v}_\nabla \times \hat{B} \times \hat{B} = -\vec{v}_\nabla$, thus

$$\vec{v}_\nabla = \frac{\vec{F}_\nabla \times \hat{B}}{qB} \quad (\text{B.40})$$

This shows us that the affect of this external force is to cause a drift perpendicular to the magnetic field. If we substitute in $\vec{F} = q\vec{E}$, we get the drift that will be caused by an electric field, called the $\vec{E} \times \vec{B}$ drift. In this case both electrons and protons will drift eastward.

In the case of our particle gyrating around a magnetic field with a gradient and no electric field

$$\vec{v}_\nabla = -\frac{v_\perp \rho_c}{2B} \nabla_\perp B \times \hat{B} = \frac{mv_\perp^2}{2qB^2} \hat{B} \times \nabla_\perp B \quad (\text{B.41})$$

Notice the dependence on charge. This causes electrons to drift in an eastward direction, while protons drift westward. There is an assumption baked into this derivation, which is that the magnetic field intensity varies very little over a gyroradius, or that $\nabla_\perp B \rho_c \ll B \implies \rho_c \nabla_\perp B / B \ll 1$.

Suppose now that our particle has an $\alpha < 90^\circ$. Now it will spiral around the field line, but in a dipole the field line is not straight, it has a curvature to it. Because of that the particle will feel a centripetal force

$$\vec{F}_c = \frac{mv_\parallel^2}{R_c} \hat{n} \quad (\text{B.42})$$

where \hat{n} is the unit normal vector along the radius of curvature, R_c . It then follows that the drift from this force will be

$$\vec{v}_c = \frac{mv_\parallel^2}{qR_c B} \hat{n} \times \hat{B} \quad (\text{B.43})$$

For fields that are curl free it is true that

$$\nabla_\perp B = -B \frac{\hat{n}}{R_c} \implies \frac{\hat{n}}{R_c} = -\frac{\nabla_\perp B}{B} \quad (\text{B.44})$$

Using this

$$\vec{v}_c = \frac{mv_\parallel^2}{qB^2} \hat{B} \times \nabla_\perp B \quad (\text{B.45})$$

Notice how similar this is to the gradient drift. Because of that it is helpful to combine the two into a general gradient curvature drift. We can also use α to describe v_\perp and v_\parallel .

$$\vec{v}_{cg} = \frac{mv^2}{2qB^2} (1 + \cos^2 \alpha) \hat{B} \times \nabla_\perp B \quad (\text{B.46})$$

To make this easier to use with the information that we often have, let's assume the perfect dipole field and make the measurement at the equator.

$$\vec{v}_{cg} = \frac{KE_{\text{total}}}{qB^2} (1 + \cos^2 \alpha) \nabla_r \vec{B} \hat{\phi} \quad (\text{B.47})$$

$$= -\frac{KE_{\text{total}} r^6}{qM^2} (1 + \cos^2 \alpha) \frac{3M}{r^4} \hat{\phi} \quad (\text{B.48})$$

$$= -\frac{3KE_{\text{total}} r^2}{qM} (1 + \cos^2 \alpha) \hat{\phi} \quad (\text{B.49})$$

$$= -\frac{3KE_{\text{total}} L^2 R_E^2}{qM} (1 + \cos^2 \alpha) \hat{\phi} \quad (\text{B.50})$$

where we've replaced $mv^2/2$ with the particle's kinetic energy, r with L , and used the fact that $\vec{B} = M/r^3 \hat{\theta}$ at the equator. The known values $R_E = 6.38 \times 10^6 \text{ m}$, $q = -1.6 \times 10^{-19} \text{ C}$, and $M = 8 \times 10^{15} \text{ T} \cdot \text{m}^3$ combine, such that $R_E^2/qM = 3.18 \times 10^{16} [\text{s} \cdot \text{kg}^{-1} \cdot \text{m}^{-1}]$ (Kivelson & Russell, 1995; Mamajek, Prsa, Torres, et al., 2015).

$$\vec{v}_{cg} = 9.54 \times 10^{16} KE_{\text{total}} L^2 (1 + \cos^2 \alpha) \hat{\phi} [\text{m} \cdot \text{s}^{-1}] \quad (\text{B.51})$$

Finally, converting Joules to electron volts, as that is a more common unit of energy, we get the drift velocity of an electron at the equator. The electron will drift in the $\hat{\phi}$ direction, which is eastward.

$$v_{cg} = 1.53 \times 10^{-2} KE_{\text{total}} L^2 (1 + \cos^2 \alpha) [\text{m} \cdot \text{s}^{-1}] \quad (\text{B.52})$$

B.4 Bounce Motion

The final major configuration of Earth's dipole magnetic field, that we haven't considered yet, is the changing magnetic field along a field line. If a particle gyrates along a field line, as it gets to lower θ values, or high magnetic latitude, it will get closer to the planet and the field strength will increase. Essentially, the magnetic field lines get closer and closer together as they approach the poles. This sort of configuration is known as a magnetic trap. To see why it is called that, we

have to understand a property of charged particles in a magnetic field called the magnetic moment.

$$\mu = \frac{\frac{1}{2}mv_{\perp}^2}{B} = \frac{\frac{1}{2}mv^2 \sin^2 \alpha}{B} \quad (\text{B.53})$$

A interesting property of the magnetic moment is that even if the energy of the particle changes, this quantity will remain constant, assuming that the field changes slowly. Slowly means that the changes over a single gyration will be small. The total kinetic energy of the particle can be written as

$$KE_{\text{total}} = KE_{\perp} + KE_{\parallel} = \frac{1}{2}mv_{\perp}^2 + \frac{1}{2}mv_{\parallel}^2 \quad (\text{B.54})$$

Using this it then follows that

$$\mu = \frac{\left(KE_{\text{total}} - \frac{1}{2}mv_{\parallel}^2\right)}{B} \quad (\text{B.55})$$

If μ is constant and the kinetic energy is constant then, for a larger magnetic field strength, the particles velocity parallel to the magnetic field will be smaller. Eventually, as B increases the parallel velocity will go to zero. This is known as the mirror point. Here the particle will stop moving towards the planet and instead begin moving in the opposite direction, towards the opposite pole. Near the opposing pole it will experience a similar mirror point and thus will bounce back and forth between the two points, hence the magnetic trap. Our next step is to figure out where this mirror point is located. Knowing that μ is constant over the entire path of the particle

$$\frac{KE_{\text{total}} \sin^2 \alpha_0}{B_0} = \frac{KE_{\text{total}} \sin^2 \alpha_{\text{mirror}}}{B_{\text{mirror}}} \implies B_{\text{mirror}} = \frac{B_0}{\sin^2 \alpha_0} \text{ since } \alpha_{\text{mirror}} = 90^\circ \quad (\text{B.56})$$

where α_0 and B_0 are the pitch angle and magnetic field at some initial point. For simplicity we'll choose this to be at the magnetic equator. As we've seen previously, we know that the magnetic field of a dipole at the equator is only in the $\hat{\theta}$ direction, thus

$$B_0 = \frac{M}{r_0^3} = \frac{M}{(LR_E)^3} \quad (\text{B.57})$$

Where we've found r_0 in terms of L at the equator. Substituting this back into our equation for the mirror point

$$B_{\text{mirror}} = \frac{M}{(LR_E)^3 \sin^2 \alpha_0} \quad (\text{B.58})$$

The magnetic field of the mirror point is given by

$$B_{\text{mirror}} = \sqrt{B_r^2 + B_\theta^2} = \frac{M}{r_{\text{mirror}}^3} \sqrt{4 \cos^2 \theta_{\text{mirror}} + \sin^2 \theta_{\text{mirror}}} \quad (\text{B.59})$$

Simplifying a little and converting to magnetic latitude

$$B_{\text{mirror}} = \frac{M}{r_{\text{mirror}}^3} \sqrt{4 - 3 \cos^2 \lambda_{\text{mirror}}} \quad (\text{B.60})$$

We also know that the particle will stay along a field line, such that $\cos^2 \lambda = r_{\text{mirror}} / (R_E L)$ and so

$$B_{\text{mirror}} = \frac{M}{r_{\text{mirror}}^3} \sqrt{4 - \frac{3r_{\text{mirror}}}{R_E L}} \quad (\text{B.61})$$

Substituting this back into Eq. B.58 and squaring both sides

$$\frac{M^2}{r_{\text{mirror}}^6} \left(4 - \frac{3r_{\text{mirror}}}{R_E L} \right) = \frac{M^2}{(LR_E)^6 \sin^4 \alpha_0} \quad (\text{B.62})$$

With some simplifying this becomes

$$\frac{r_{\text{mirror}}^6}{L^6 R_E^6 \sin^4 \alpha_0} = 4 - \frac{3r_{\text{mirror}}}{R_E L} \quad (\text{B.63})$$

We are particularly interested in the altitude above the earth's surface that the mirror point happens.

To solve for this $r_{\text{mirror}} = R_E + \delta r$, where δr is the altitude.

$$\frac{1}{\sin^4 \alpha_0} \left(\frac{1}{L} + \frac{\delta r}{LR_E} \right)^6 = 4 - 3 \left(\frac{1}{L} + \frac{\delta r}{LR_E} \right) \quad (\text{B.64})$$

Letting $x = \left(\frac{1}{L} + \frac{\delta r}{LR_E}\right)$, the equation we need to solve is then

$$\frac{1}{\sin^4 \alpha_0} x^6 + 3x - 4 = 0 \quad (\text{B.65})$$

Alternatively we can plot Eq. B.64 over a variety of different altitudes, which I've done in Figure 8.

B.5 Plasma Waves

This derivation will follow along that of Russell, Luhmann, and Strangeway (2016). Since a plasma is composed of a collection of charged particles it reacts to electric and magnetic fields. Waves in those fields will thus perturb the plasma. This is known as an electromagnetic wave. Space plasmas also behave like a gas, so they can have density and pressure waves similar to sound waves. In reality, a plasma wave is a combination of both of these phenomena and so behaves differently from both. For this derivation we will start with the fluid continuity equations given by Section 3.5.2 in Russell, Luhmann, and Strangeway (2016). First up is the momentum equation for 3 orthogonal directions where the subscript represents the coordinate.

$$\frac{\partial}{\partial t} (mn\bar{v}_i) + \frac{\partial}{\partial x_j} [P_{ji} + nm(\bar{v}_j\bar{u}_i + \bar{u}_j\bar{v}_i - \bar{u}_j\bar{u}_i)] - \quad (\text{B.66})$$

$$n \left[q \left(E_i + \left(\vec{v} \times \vec{B} \right)_i \right) + F_{gi} \right] = \frac{\partial}{\partial t} (mn\bar{v}_i) \Big|_c \quad (\text{B.67})$$

The terms in this equation are as follows:

- m - mass of the particle (electron or ion)
- n - number density of the particles
- v - velocity of an individual particle
- u - bulk flow velocity of the particles (electron or ion)
- P - pressure of the gas

- q - charge of the particle
- E - wave electric field
- F_g - external forces, i.e. gravity
- $|_c$ - signifies that the term is due to collisions

This is a pretty nasty equation, but thankfully we're going to make assumptions that will clean it up a bit. We assume that the wave solutions will be harmonic, meaning

$$\vec{y} = \vec{y}_0 e^{i(\vec{k} \cdot \vec{r} - \omega t)} \quad (\text{B.68})$$

where \vec{y} is a perturbed quantity such as the electric field or current density, \vec{k} is the wave vector, \vec{r} is the position vector, and ω is the wave frequency. If the solution is harmonic we can ignore second order and higher terms, so the momentum equation becomes

$$-i\omega n_s m_s \vec{u}_s + i\vec{k} \delta P_s = n_s q_s \left(\vec{E} + \vec{u}_s \times \vec{B}_0 \right) \quad (\text{B.69})$$

Here we've used the knowledge that the $\partial/\partial t$ operator on a harmonic solution is $-i\omega$ and $\partial/\partial x$ is $i\vec{k}$. We've also assumed that the plasma is collisionless and so can ignore that term. We've also assumed that δP_s , the plasma pressure perturbation, is a scalar. We'll use δ for the perturbations to indicate that they are small quantities away from the mean. Next we need to look at the continuity equation

$$\frac{\partial \rho}{\partial t} + \nabla \cdot (\rho \vec{u}) = 0 \quad (\text{B.70})$$

Again we'll use the operator trick for a harmonic solution and only take first order terms. This then becomes

$$-i\omega \delta n_s + i n_s \vec{k} \cdot \vec{u}_s = 0 \quad (\text{B.71})$$

where δn_s is the number density perturbation. Finally we need an equation for the pressure perturbation. We do this with Equation 3.167 from Russell, Luhmann, and Strangeway (2016).

$$P = \frac{\gamma P_0}{\rho_0} \rho \quad (\text{B.72})$$

Here, ρ is the mass density, P the pressure, and γ is the ratio of specific heats. Using the knowledge that the zero order pressure $P_s = n_s K T_s$, where T_s is the temperature of the species (electron or ion), the equation becomes

$$\delta P_s = \frac{\gamma_s P_s}{m_s n_s} m_s \delta n_s = \gamma_s K T_s \delta n_s \quad (\text{B.73})$$

Combining Equations B.69, B.71, and B.73 we get an expression that relates the perturbation flow velocity for a species to the wave electric field

$$\omega^2 \vec{u}_s - \frac{\gamma_s K T_s}{m_s} \vec{k} (\vec{k} \cdot \vec{u}_s) = i \omega \frac{q_s}{m_s} (\vec{E} + \vec{u}_s \times \vec{B}_0) \quad (\text{B.74})$$

Finally we can close the equations with the current density

$$\vec{j} = \sum_s n_s q_s \vec{u}_s \quad (\text{B.75})$$

For the purposes of my thesis I am mostly interested in the behavior of electromagnetic waves in a cold magnetized plasma. Whistler-mode waves are the primary wave type associated with pulsating aurora and they fall into this category. With the assumption that the plasma is cold, or that

$$\frac{\omega^2}{k^2} \gg \frac{\gamma_s K T_s}{m_s} \quad (\text{B.76})$$

We can ignore the effects of plasma pressure. Thus Equation B.74 reduces to

$$\vec{u}_s = i \frac{q_s}{\omega m_s} (\vec{E} + \vec{u}_s \times \vec{B}_0) \quad (\text{B.77})$$

It will be helpful to express this in terms of the current density from a species. For this we will de-

fine the species plasma frequency $\omega_{ps}^2 = n_s q_s^2 / \epsilon_0 m_s$, and the species gyro frequency $\Omega_s = q_s B_0 / m_s$. From Equation B.75 $\vec{u}_s = \vec{j}_s / n_s q_s$, thus

$$\vec{j}_s = i \frac{\omega_{ps}^2}{\omega} \epsilon_0 \vec{E} + i \frac{\Omega_s}{\omega} \vec{j}_s \times \hat{b} \quad (\text{B.78})$$

where \hat{b} is a unit vector in the direction of the ambient magnetic field \vec{B}_0 . Splitting this equation into Cartesian components.

$$j_{sx} = i \frac{\omega_{ps}^2}{\omega} \epsilon_0 E_x + i \frac{\Omega_s}{\omega} j_{sy} \quad (\text{B.79})$$

$$j_{sy} = i \frac{\omega_{ps}^2}{\omega} \epsilon_0 E_y - i \frac{\Omega_s}{\omega} j_{sx} \quad (\text{B.80})$$

$$j_{sz} = i \frac{\omega_{ps}^2}{\omega} \epsilon_0 E_z \quad (\text{B.81})$$

Combining the x and y components together

$$j_{sx} = i \frac{\omega_{ps}^2}{(\omega^2 - \Omega_s^2)} \epsilon_0 (\omega E_x + i \Omega_s E_y) \quad (\text{B.82})$$

$$j_{sy} = i \frac{\omega_{ps}^2}{(\omega^2 - \Omega_s^2)} \epsilon_0 (\omega E_y - i \Omega_s E_x) \quad (\text{B.83})$$

We now have a set of equations that describes the current density per species entirely in terms of the wave electric field. The terms that multiply the electric field components are the elements of the conductivity tensor σ . We can get another equation relating the current density and electric field by combining Faraday's law and the time derivative of Ampere's law for a harmonic solution, this leads to

$$k^2 \vec{E} - \vec{k} (\vec{k} \cdot \vec{E}) - \frac{\omega^2}{c^2} \vec{E} = i \omega \mu_0 \vec{j} \quad (\text{B.84})$$

Using the refractive index $\mu = kc / \omega$, and the relation $c^2 = 1 / \mu_0 \epsilon_0$, this becomes

$$(\mu^2 - 1) \vec{E} - \mu^2 \hat{k} (\hat{k} \cdot \vec{E}) = \frac{i}{\omega \epsilon_0} \vec{j} \quad (\text{B.85})$$

where \hat{k} is the unit vector along \vec{k} . Before going further we'll assume high frequencies, meaning that $\omega \gg \omega_{pi}$. This allows us to neglect the contribution to \vec{j} from the ions. We will now consider the case of a wave propagating parallel to the ambient magnetic field, such that $\hat{k} \parallel \vec{B}_0$, then the components of Equation B.85 will be

$$(\mu^2 - 1) E_x = \frac{i}{\omega \epsilon_0} j_x \quad (\text{B.86})$$

$$(\mu^2 - 1) E_y = \frac{i}{\omega \epsilon_0} j_y \quad (\text{B.87})$$

$$E_z = -\frac{i}{\omega \epsilon_0} j_z \quad (\text{B.88})$$

Using our derived current density components this becomes

$$(\mu^2 - 1) E_x = -\frac{\omega_{pe}^2}{(\omega^2 - \Omega_e^2)} \left(E_x - i \frac{|\Omega_e|}{\omega} E_y \right) \quad (\text{B.89})$$

$$(\mu^2 - 1) E_y = -\frac{\omega_{pe}^2}{(\omega^2 - \Omega_e^2)} \left(E_y + i \frac{|\Omega_e|}{\omega} E_x \right) \quad (\text{B.90})$$

$$E_z = \frac{\omega_{pe}^2}{\omega^2} E_z \quad (\text{B.91})$$

Written in matrix form this becomes

$$\begin{pmatrix} (\mu^2 - 1)(\omega^2 - \Omega_e^2) + \omega_{pe}^2 & -i\omega_{pe}^2 \frac{|\Omega_e|}{\omega} & 0 \\ i\omega_{pe}^2 \frac{|\Omega_e|}{\omega} & (\mu^2 - 1)(\omega^2 - \Omega_e^2) + \omega_{pe}^2 & 0 \\ 0 & 0 & \omega^2 - \omega_{pe}^2 \end{pmatrix} \times \begin{pmatrix} E_x \\ E_y \\ E_z \end{pmatrix} = 0 \quad (\text{B.92})$$

We can find the solutions of this by finding the determinant of the matrix and setting it to zero. However, before doing that one solution jumps out. That solution occurs for $E_x = E_y = 0$ and $E_z \neq 0$ and is

$$\omega^2 = \omega_{pe}^2 \quad (\text{B.93})$$

The other solutions will be for

$$\begin{vmatrix} (\mu^2 - 1)(\omega^2 - \Omega_e^2) + \omega_{pe}^2 & -i\omega_{pe}^2 \frac{|\Omega_e|}{\omega} \\ i\omega_{pe}^2 \frac{|\Omega_e|}{\omega} & (\mu^2 - 1)(\omega^2 - \Omega_e^2) + \omega_{pe}^2 \end{vmatrix} = 0 \quad (\text{B.94})$$

However, this determinant is just in the form $a^2 - b^2 = 0$, or $a = \pm b$, thus

$$(\mu^2 - 1)(\omega^2 - \Omega_e^2) + \omega_{pe}^2 = \pm \frac{\omega_{pe}^2 |\Omega_e|}{\omega} \quad (\text{B.95})$$

We can rearrange terms to get a dispersion relation, which related wave number k to wave frequency ω .

$$\mu^2 - 1 = -\omega_{pe}^2 \left(1 \mp \frac{|\Omega_e|}{\omega} \right) \frac{1}{\omega^2 - \Omega_e^2} \quad (\text{B.96})$$

$$= -\omega_{pe}^2 \left(\frac{1}{\omega^2 - \Omega_e^2} \mp \frac{|\Omega_e|}{\omega(\omega^2 - \Omega_e^2)} \right) \quad (\text{B.97})$$

$$= -\omega_{pe}^2 \left(\frac{\omega \mp |\Omega_e|}{\omega(\omega^2 - \Omega_e^2)} \right) \quad (\text{B.98})$$

$$= -\omega_{pe}^2 \left(\frac{\omega \mp |\Omega_e|}{\omega(\omega \pm |\Omega_e|)(\omega \mp |\Omega_e|)} \right) \quad (\text{B.99})$$

$$\implies \mu^2 = 1 - \frac{\omega_{pe}^2}{\omega(\omega \pm |\Omega_e|)} \quad (\text{B.100})$$

There is a resonance (refractive index goes to infinity) if we use the negative sign and let $\omega = |\Omega_e|$. Looking back at the origin of this plus-minus sign in the matrix equation we can see that the resonance implies that $E_x + iE_y = 0$. Because the y-component is imaginary, it lags the x-component by 90° or $1/4$ period. This represents a right-hand circularly polarized wave (R mode). The positive sign corresponds to a left-hand polarized wave (L mode). Whistler waves are an R mode wave and occur for frequencies below the electron cyclotron frequency.

B.6 Pitch Angle Diffusion

This derivation will follow along that of Brice (1964). Whistler mode waves are characterized by an electric field that rotates around the ambient magnetic field in the right-handed sense. To see how the energy of an electron can be altered by these waves we'll first go back to the force on a charged particle due to an electric (\vec{E}) and magnetic (\vec{B}) field.

$$\vec{F} = q \left(\vec{E} + \vec{v} \times \vec{B} \right) \quad (\text{B.101})$$

where q and \vec{v} are the charge and velocity of the particle. We can describe the change in energy of the particle ΔKE over a distance $\Delta \vec{s}$, by

$$\Delta KE = \vec{F} \cdot \Delta \vec{s} \quad (\text{B.102})$$

$$= q \left(\vec{E} + \vec{v} \times \vec{B} \right) \cdot \vec{v} \Delta t \quad (\text{B.103})$$

$$= q \vec{E} \cdot \vec{v} \Delta t \quad (\text{B.104})$$

For appreciable energy transfer, there needs to be a constant component of the dot product between the electric field and electron velocity. We'll split the velocity into a component parallel to the magnetic field, and one perpendicular. We will then get longitudinal resonance when

$$\vec{E}_{\parallel} \cdot \vec{v}_{\parallel} = \text{constant} \quad (\text{B.105})$$

We will get transverse resonance when

$$\vec{E}_{\perp} \cdot \vec{v}_{\perp} = \text{constant} \quad (\text{B.106})$$

For the longitudinal resonance the requirement is

$$v_{\parallel} \cos \theta = v_p \quad (\text{B.107})$$

where v_p is the wave phase velocity and θ is the angle between the wave normal and Earth's magnetic field.

For the transverse resonance the electron cyclotron frequency needs to match the wave frequency. However, whistler waves only occur below the electron cyclotron frequency. The only way to get the wave and electron frequency to match is if they are travelling in opposite directions leading to a Doppler shift. Therefore, the following requirement for transverse resonance is

$$\gamma v_{\parallel} \cos \theta = v_p \frac{\omega - \Omega_e}{\omega} \quad (\text{B.108})$$

where Ω_e is the electron cyclotron frequency and

$$\gamma = \left(1 - \frac{v_{\parallel}^2}{c^2} \right)^{-1/2} \quad (\text{B.109})$$

For nonrelativistic electrons we will assume this is 1. In Equation B.108 it is useful to solve for the wave phase velocity v_p . One way to do this is from the dispersion relation for whistler waves from Equation B.100.

$$\mu^2 = 1 - \frac{\omega_{pe}^2}{\omega(\omega - |\Omega_e|)} \quad (\text{B.110})$$

The refractive index $\mu = ck/\omega_{pe} = c/v_p$, thus

$$\frac{c^2}{v_p^2} = 1 - \frac{\omega_{pe}^2}{\omega(\omega - |\Omega_e|)} \quad (\text{B.111})$$

Finally, we'd like to express the electron plasma frequency ω_{pe} in terms of values that we can measure. One way of defining this is

$$\omega_{pe}^2 = \frac{n_e q_e^2}{\epsilon_0 m_e} \quad (\text{B.112})$$

where n_e is the electron density (which can be measured/estimated). To calculate the resonant energy of a given frequency we now just need to know the wave propagation angle, electron pitch

angle, electron cyclotron frequency, and electron density.

To examine the energy transfer between an electron and a wave propagating with $\theta = 0$ in more detail, we will start with Maxwell's equation

$$\nabla \times \vec{E} = -\frac{\partial \vec{B}}{\partial t} \quad (\text{B.113})$$

With the assumption that the electric and magnetic fields vary harmonically, hence the operator $\nabla \times = i\vec{k}$ and $\partial/\partial t = -i\omega$, it follows that

$$\vec{k} \times \vec{E} = \omega_{pe} \vec{B} \quad (\text{B.114})$$

Since \vec{E} is perpendicular to \vec{k}

$$\left| \frac{E}{B} \right| = \left| \frac{\omega_{pe}}{k} \right| = |v_p| \quad (\text{B.115})$$

The force on an electron moving with the wave phase velocity will thus be

$$\vec{F} = q \left(\vec{E} + \vec{v}_p \times \vec{B} \right) = q(E - E) = 0 \quad (\text{B.116})$$

Therefore the energy of an electron in the frame of reference moving with the phase velocity is constant, which means that

$$\frac{1}{2}mv_{\perp}^2 + \frac{1}{2}m(v_{\parallel} - v_p)^2 = \text{constant} \quad (\text{B.117})$$

Assuming the wave makes small changes to the velocity of the electron, to first order

$$mv_{\perp}\Delta v_{\perp} + mv_{\parallel}\Delta v_{\parallel} - mv_p\Delta v_p = 0 \quad (\text{B.118})$$

In the rest frame, the change in energy of the electron will be

$$\Delta KE = mv_{\perp}\Delta v_{\perp} + mv_{\parallel}\Delta v_{\parallel} = mv_p\Delta v_{\parallel} \quad (\text{B.119})$$

The change in transverse and longitudinal energy of the electron is

$$\Delta KE_{\perp} = mv_{\perp} \Delta v_{\perp} \quad \Delta KE_{\parallel} = mv_{\parallel} \Delta v_{\parallel} \quad (\text{B.120})$$

From this we can see that

$$\frac{\Delta KE_{\parallel}}{\Delta KE} = \frac{v_{\parallel}}{v_p} \quad (\text{B.121})$$

and that

$$\frac{\Delta KE_{\perp}}{\Delta KE} = 1 - \frac{v_{\parallel}}{v_p} \quad (\text{B.122})$$

From Equation B.108 it follows that

$$\frac{v_{\parallel}}{v_p} = -\frac{\Omega_e - \omega}{\omega} \quad (\text{B.123})$$

and then that

$$\frac{\Delta KE_{\perp}}{\Delta KE} = 1 + \frac{\Omega_e - \omega}{\omega} = \frac{\Omega_e}{\omega} \quad (\text{B.124})$$

We know that $\Omega_e > \omega$ for whistler waves, so the change in transverse energy is greater than the total change in energy. That means, the longitudinal energy must change by an opposite, but smaller amount. If the resonance is such that the change in total energy is negative (the electron loses energy), the transverse energy will decrease, while the longitudinal energy increases by a smaller amount. Because the pitch angle of the electron is defined as

$$\alpha = \tan^{-1} \frac{v_{\perp}}{v_{\parallel}} \quad (\text{B.125})$$

We can figure out how much the pitch angle will change by first determining the following relation

$$\tan \alpha = \frac{v_{\perp}}{v_{\parallel}} \quad (\text{B.126})$$

$$\implies \Delta \tan \alpha = \frac{v_{\parallel} \Delta v_{\perp} - v_{\perp} \Delta v_{\parallel}}{v_{\parallel}^2} \quad (\text{B.127})$$

$$\implies \frac{\Delta \tan \alpha}{\tan \alpha} = \frac{v_{\parallel} \Delta v_{\perp} - v_{\perp} \Delta v_{\parallel}}{v_{\perp} v_{\parallel}} = \frac{\Delta v_{\perp}}{v_{\perp}} - \frac{\Delta v_{\parallel}}{v_{\parallel}} \quad (\text{B.128})$$

We also know that $\Delta v_{\perp}/v_{\perp} = \Delta KE_{\perp}/mv_{\perp}^2$ and that $mv_{\perp}^2 = 2KE_{\perp}$. Using this fact and the equivalent expression for the parallel component

$$\frac{\Delta \tan \alpha}{\tan \alpha} = \frac{1}{2} \left(\frac{\Delta KE_{\perp}}{KE_{\perp}} - \frac{\Delta KE_{\parallel}}{KE_{\parallel}} \right) \quad (\text{B.129})$$

Using the relations $d(\tan \alpha)/d\alpha = 1 + \tan^2 \alpha$, $KE_{\perp}/KE = \sin^2 \alpha$, and $KE_{\parallel}/KE = \cos^2 \alpha$ we can get that

$$\Delta \alpha = \frac{\tan \alpha}{2(1 + \tan^2 \alpha)} \left[\frac{\Delta KE_{\perp}}{\Delta KE \sin^2 \alpha} - \frac{\Delta KE_{\parallel}}{\Delta KE \cos^2 \alpha} \right] \frac{\Delta KE}{KE} \quad (\text{B.130})$$

Finally using Equations B.122, B.123, and B.124, we can get the change in pitch angle as a function of the change in total energy.

$$\Delta \alpha = \frac{\tan \alpha}{2(1 + \tan^2 \alpha)} \left[\frac{\Omega_e}{\omega \sin^2 \alpha} + \frac{\Omega_e - \omega}{\omega \cos^2 \alpha} \right] \frac{\Delta KE}{KE} \quad (\text{B.131})$$